DESIGN AND APPLICATION OF A CNC ROTARY AXIS FOR GRINDING RESEARCH

by

Scott Dewar

Submitted in partial fulfillment of the requirements
for the degree of Master of Applied Science

at

Dalhousie University
Halifax, Nova Scotia
August 2017

Table of Contents

List of Tables

List of Figures

Abstract

This thesis presents four studies into cylindrical plunge grinding that used a custom built, instrumented rotary axis. The design and capabilities of the rotary axis are presented. These capabilities include accurate speed control and in-process force measurement. The rotary axis enabled research into workpiece stiffness, which show a 2.5 fold decrease in the effective stiffness from a 1" (25.4 mm) change in grinding location. The wheel wear of grooved wheels is also shown to be higher than the wear of non-grooved wheels. A method of optimizing material removal through force curve inspection was presented and found to be effective at reducing wear. The largest study compared the performance of grooved and non-grooved wheels in plunge grinding. It was found that grooved wheels lowered grinding forces, spindle power, specific energy, and the time constants. However, there was an increase in surface roughness and no measurable change in workpiece roundness. The final study looked at the effect of angular speed ratios on plunge grinding with grooved wheels. There was an observed texture at integer speed ratios and a variation of the grinding forces, power, and surface roughness at non-integer speed ratios. A formula was presented that can predict the texture of a circumferentially grooved wheel and may be used to explain the other process variations.

List of Abbreviations and Symbols Used

A_g Total surface area of the grooves.

A_o Total wheel face surface area.

F_n Normal force.

F_r Radial force.

F_t Tangential force.

L Grain spacing.

L_g Lead of grooves.

MRR Material Removal Rate.

N Number of complete waves.

P_s Spindle Power.

R_a Average surface roughness.

ϵ Chatter wave phase.

ϵ_g Wheel contact phase.

η Groove Factor.

T_d Dwell time.

ω_s Wheel angular velocity.

ω_w Workpiece angular velocity.

τ Plunge grinding time constant.

a Actual depth of cut.

a_g Depth of groove.

b_g Width of groove.

b_w Width of ground surface.

d Commanded depth of cut.

d_e Equilvalent diameter.

d_s Grinding wheel diameter.

d_w Workpiece diameter.

f Frequency of chatter.

h_m Minimum uncut chip thickness.

k_a Contact stiffness.

k_c Cutting stiffness.

k_e Effective stiffness.

k_s Grinding machine stiffness.

k_w Rotary axis stiffness.

l_c Grinding contact length.

n General spindle speed.

r_ω Angular velocity ratio.

t_z Distance between max and min traces.

u Specific grinding energy.

v_f Infeed speed.

v_r Radial speed.

v_s Wheel speed.

v_w Workpiece speed.

Acknowledgements

Although it is my name on this thesis, there are many people responsible for bringing it to fruition. My supervisors, Dr. Andrew Warkentin and Dr. Robert Bauer, are first on this list. Their guidance and patience were invaluable, and I hope that their scientific curiosity and professionalism has rubbed off on me over the past two years.

The mechanical engineering staff deserve substantial credit. Angus McPherson and Mark MacDonald made machining approachable and I consider myself a better engineer thanks to their advice. Jon MacDonald's electrical troubleshooting skills saved me from many hours of frustrations and electrocutions. To Peter Jones, Kate Hide, Robert Warner, Reg Peters, Albert Murphy, and my committee members, Dr. Darrel Doman and Dr. Claver Diallo, I appreciate all you have done for me, you are what makes Dalhousie engineering great.

I would be remiss if I did not recognize the enormous role my family's played in getting me here. My sisters have shown me there are many ways to succeed in life; their example pushes me to be better. My parents have never been anything less than loving and supportive. If I have a fraction of my father's strength of character or my mother's kindness and compassion, I am very lucky.

Finally, there's Emma. I hope to spend a long, long time thanking you, for everything.

Chapter 1

Introduction

Cylindrical grinding is an abrasive machining process used to machine round parts to fine tolerances. Abrasive machining uses hard particles (in this case bonded together in the form of a wheel) to cut away material from a workpiece. Grinding is able to machine a wide variety of materials, and can produce parts with extremely close tolerances and a very fine surface finish. Cylindrical grinding is a subset of grinding that produces round parts for many of the products we use everyday; from the shafts that turn in the engine of a car, to the rolls used to print out a daily newspaper. Cylindrical grinding and the grinding wheels that make it happen play a large role in everyday life without most people realizing.

1.1 Motivation

The Grinding Lab is very well equipped to study grinding and has a long history of publishing important research on the topic. However, these papers have been confined to surface grinding (the grinding of flat parts) because of a lack of cylindrical grinding capabilities. Since cylindrical grinding behaves differently than flat grinding much of the Grinding Lab's recent research could be expanded upon if there was a rotary axis available for use. In particular, there is a large gap in knowledge of the effects of modified grinding wheels in cylindrical grinding. Recent studies in the Grinding Lab have shown a significant reduction in grinding forces using modified grinding wheels (specifically wheels with a circumferentially-grooved face) which could be appealing in a cylindrical grinding applications.

1.2 Objectives

The objectives of this thesis were to:

- Design and build a rotary axis for the grinding machine capable of monitoring in-process forces.

- Develop methods to analyze cylindrical grinding using data collected by the rotary axis.

- Compare the effects of grooved grinding wheels and non-grooved grinding wheels on cylindrical plunge grinding.

1.3 Thesis Outline

This thesis was split into seven chapters. Chapter 2 will provide essential background information on abrasive machining in general, and cylindrical grinding in particular. Chapter 3 covers the current literature as well as the niche that this thesis aims to fill. Chapter 4 gives a full description of the rotary axis, including the design criteria and the machine validation experiments performed. Chapter 5 describes the experimental apparatus used in conjunction with the rotary axis, and important parameters that were common to all studies. Chapter 6 details the four preliminary cylindrical plunge grinding studies that were performed. The studies are:

1. The effect of workpiece stiffness in cylindrical plunge grinding

2. A comparison of wheel wear in grooved and non-grooved wheel

3. A comparison of the effect of infeed on grooved and non-grooved wheels

4. The effect of speed ratios on texturing and surface finish for circumferentially grooved wheels

Finally, chapter 7 is a conclusion that summarizes the findings of this thesis and provides recommendations on future work.

Chapter 2

Background

This chapter will provide a background on cylindrical grinding. There will be sections covering the basics of grinding, the kinematics and important variables used to describe cylindrical grinding, and how to analyze cylindrical grinding. This chapter will also highlight how cylindrical grinding differs from surface grinding operations.

2.1   Introduction

Modern industrial grinding operations consist of a rapidly rotating grinding wheel composed of hard abrasive particles and a bonding agent which removes material from a workpiece [1]. Figure 2.1 illustrates a typical surface grinding operation. Grinding is a very useful manufacturing process for many different reasons including: the ability to machine hard materials, a wide range of material removal rates (MRR), superior control of tolerances, and good control of workpiece surface finish [2].

Grinding can be divided into subsets based on the path the grinding wheel follows through the workpiece. The grinding subset of particular interest to this thesis is cylindrical grinding which deals with the grinding of round parts. Cylindrical grinding can be broken down further into two main types; external and internal depending on what surface is being ground as shown in Figure 2.2 [1]. The focus of this thesis will be on external cylindrical grinding.
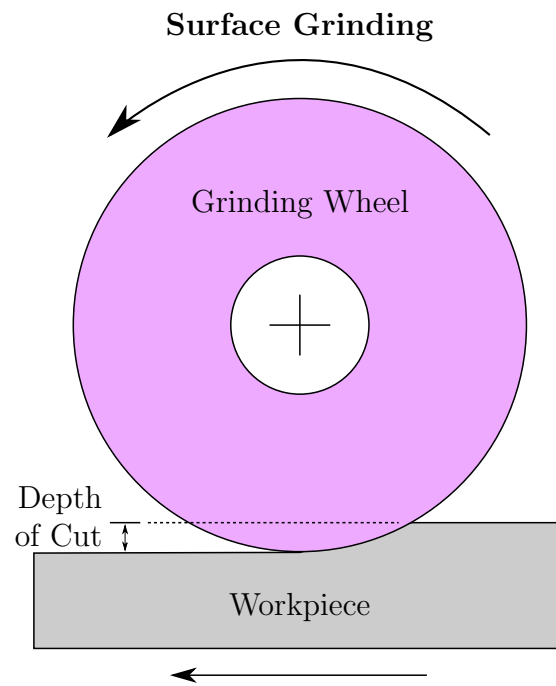
Surface Grinding

Figure 2.1: Example of surface grinding with important variables

External Cylindrical Grinding   **Internal Cylindrical Grinding**
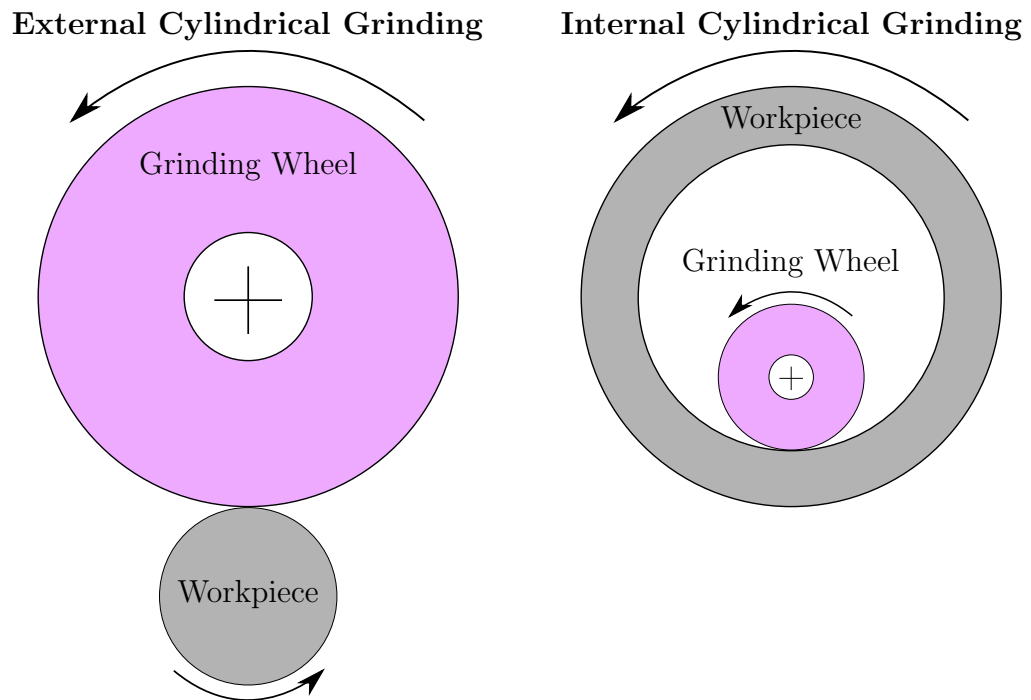
Figure 2.2: External and internal cylindrical grinding

2.2 Abrasive Wheels

Grinding wheels can be thought of as many small hard particles together with some bonding agent. There exists a standard marking system used on the most common types of grinding wheels (those with aluminum oxide or silicon carbide abrasives) that explains their specifications [3]. Shown in Figure 2.3, the system describes most of the important information like grain sizes and bond type both of which have an effect on how the wheel performs during cutting [4].

Prefix	Abrasive Type	Grain Size	Grade	Structure	Bond Type	Wheel ID

$$51-A-36-L-5-V-23$$
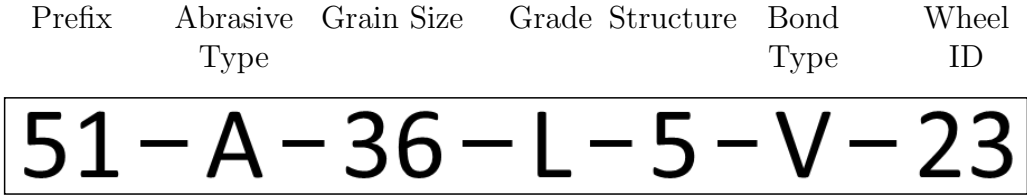
Figure 2.3: The standard grinding wheel marking system for aluminum oxide and silicon carbide abrasives

2.2.1 Rubbing, Plowing, and Cutting

As grinding is performed on a workpiece the active grains can do one of three things: rub, plow, or cut as shown in Figure 2.4 [5, 6]. While cutting is the only one of the three that actual removes material, all three take energy and affect the workpiece. Interestingly, over half of the grinding energy goes into rubbing and plowing which is then transferred into heat [7]. A highly cited paper by Malkin and Guo goes into further detail on how the energy partition works between these three phenomenon [8].
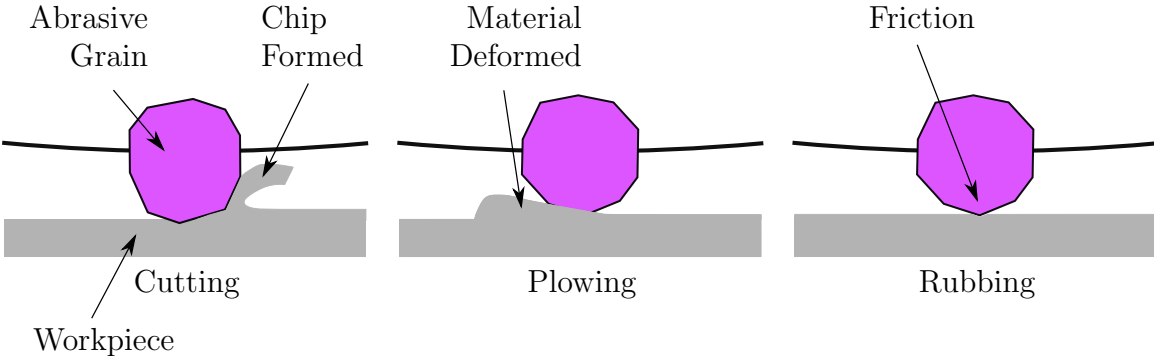
Figure 2.4: Cutting, rubbing, and plowing of abrasive grain

2.3   Kinematics of Cylindrical Grinding

The variables and their relevant equations that are presented in this section will be used throughout this thesis to explain the kinematics of cylindrical grinding and describe the grinding process. This section also highlights some of the differences between cylindrical grinding and surface grinding.

2.3.1   Plunge and Traverse Grinding
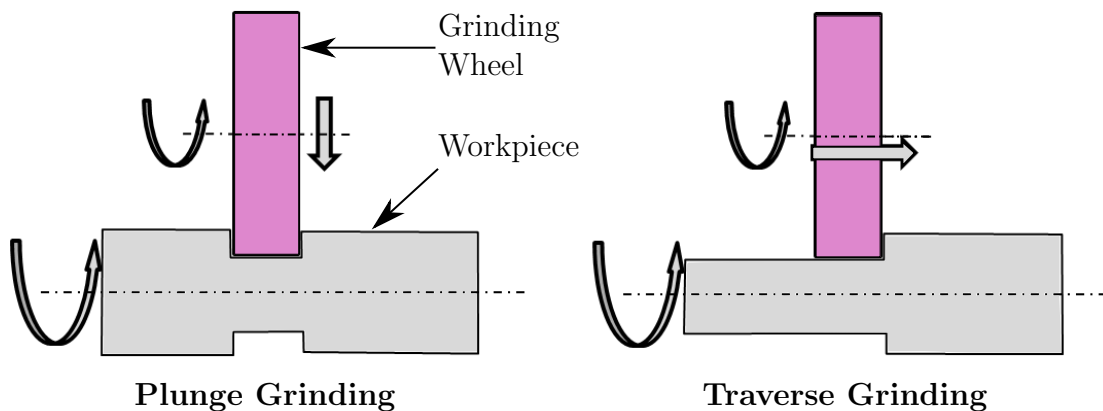
Figure 2.5: Plunge and traverse grinding

While performing a cylindrical grinding operation there are two options for the wheel path during the cut: plunge and traverse, both shown in Figure 2.5. The added axial motion of traverse grinding adds new factors to the analysis of the grinding process such as a radial force component [9]. Both methods of cylindrical grinding have their benefits and drawbacks with respect to surface finish, machine time, and wheel wear [10]. The focus of this thesis will be on plunge grinding.

2.3.2   Geometry of Plunge Grinding

Figure 2.6 shows the variables that describe the geometry in a cylindrical plunge grinding operation. The motion of the grinding operation is typically described in terms of the tangential wheel speed v_s in m/s, the tangential workpiece speed v_w in m/s, and its infeed rate v_f in μm per workpiece revolution. This thesis will also

use the wheel ω_s and workpiece ω_w angular speeds (both in rpm). Other important variables include the infeed a in μm, the diameters of the grinding wheel d_s and the workpiece d_w in mm, and the contact length l_c in mm which will be discussed further in Section 2.3.4.
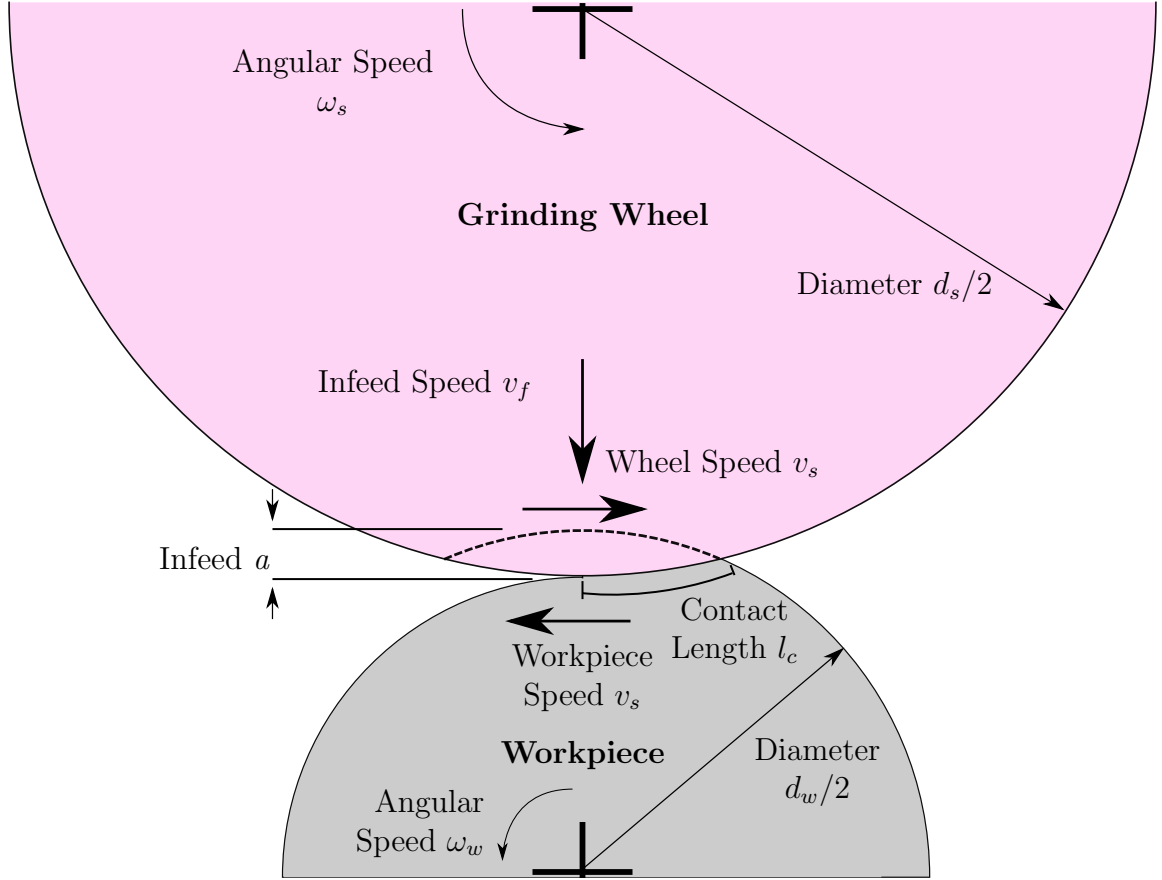
Figure 2.6: The cylindrical grinding geometry

2.3.3   Material Removal Rate

By using these newly introduced variables, the material removal rate MRR can be calculated for plunge feed grinding as shown in Equation 2.1 [11]. An important variable not shown in Figure 2.6 is the width of the grinding area b_w, which for

plunge grinding is equal to the grinding wheel width.

$$\text{MRR} = a \cdot b_w \cdot v_w \tag{2.1}$$

2.3.4 Contact Area and Equivalent Diameter

The contact area is the apparent area where the grinding wheel contacts the workpiece [4]. This area is where the grinding forces are applied and heat transfer occurs. The contact area A_c is the product of the grinding width b_w and the contact length l_c, as shown in Equation 2.2. The contact length l_c can be estimated using Equation 2.3 where d_e is the equivalent diameter, itself calculated in Equation 2.4 [4].

$$A_c = l_c \cdot b_w \tag{2.2}$$

$$l_c = \sqrt{a \cdot d_e} \tag{2.3}$$

$$d_e = \frac{d_s}{1 + \dfrac{d_s}{d_w}} \tag{2.4}$$

The equivalent diameter d_e can be used to highlight how surface grinding is different than cylindrical grinding. For example, Table 2.1 shows how, even with a constant grinding wheel size, l_c is far greater in surface grinding operations than in external cylindrical grinding operations, especially as the workpiece diameter decreases. These lower contact lengths mean that the forces and heat of the cylindrical grinding operation are concentrated in a smaller area [11].

Table 2.1: A comparison of equivalent diameter and contact length for different workpiece diameters undergoing the same grinding operation, d_s=254 mm and a=0.254 mm

Workpiece Diameter	Equivalent Diameter, mm	Contact Length, mm
Surface Grinding	254.0	8.0
254.0 mm (10")	127.0	5.7
127.0 mm (5")	84.6	4.6
25.4 mm (1")	23.1	2.4

2.3.5   Grain Spacing

While a grinding wheel is composed of many different abrasive particles, very few of these actually perform cutting in a given pass. Figure 2.7 shows a portion of the grinding wheel. The protruding grains are the active grains that will actually contact the workpiece and perform cutting, plowing or rubbing, the spacing between the cutting edges is the grain spacing L.
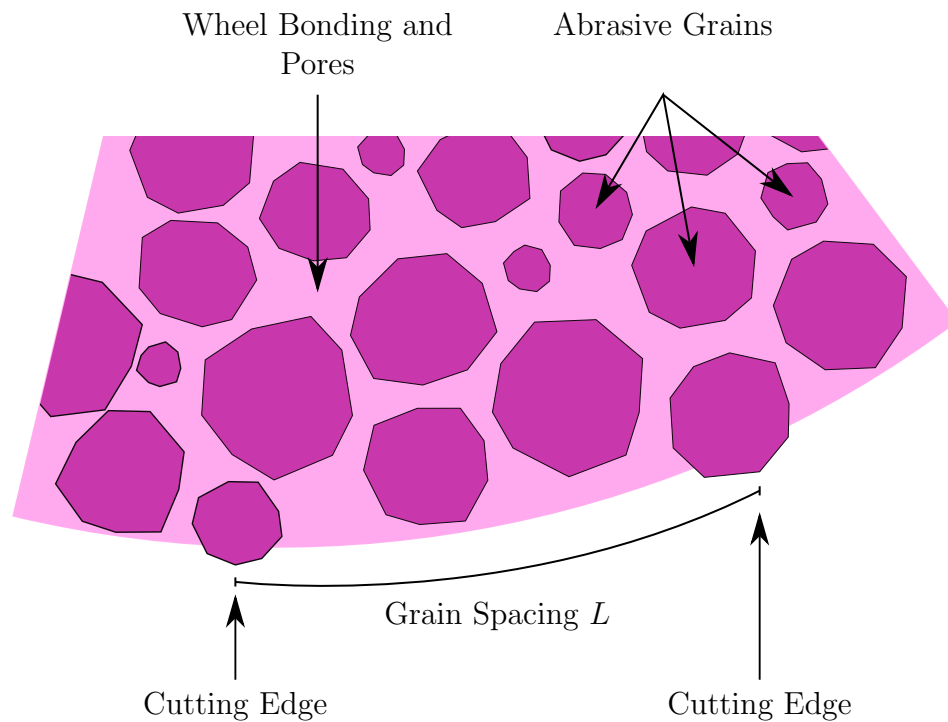
Figure 2.7: A section of a grinding wheel that showing the grain spacing between cutting points.

2.3.6   Undeformed Chip Thickness

Undeformed chip thickness h_m is the maximum cutting depth of one cutting point [4]. It is used frequently in the analysis of grinding operations and can be related to the efficiency of a grinding operation [11]. Figure 2.8 shows what the cross section of a chip looks like for cylindrical grinding. Equation 2.5 is used to calculate the undeformed chip thickness, it assumes that the cutting edges are equally spaced and protrude a constant distance from the surface of the grinding wheel [4]

$$h_m = \sqrt{\text{L} \cdot \frac{v_w}{v_s} \cdot \sqrt{\frac{a}{d_e}}} \tag{2.5}$$
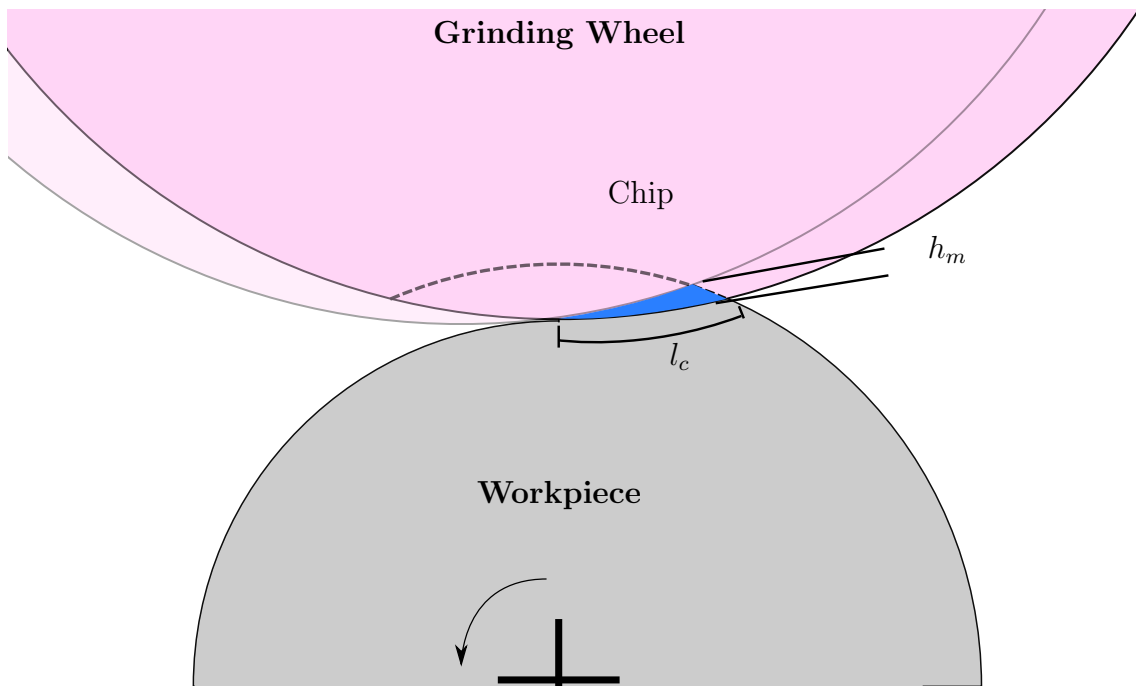
Figure 2.8: The cross section of a chip (blue) formed during plunge cylindrical grinding.

Comparing the chip thickness values for both cylindrical grinding and surface grinding, the undeformed chip thickness is found to be higher in cylindrical grinding [11]. Table 2.2 shows the relationship between workpiece diameter and chip thickness for consistent grinding conditions. This table shows that the chip thickness for a 1"

(25.4 mm) diameter cylindrically ground workpiece is almost twice as thick as the chips formed during surface grinding. Malkin has shown that a larger chip thickness increases the process' efficiency because less energy is wasted in the grain plowing into the workpiece [4], and a paper by Hecker *et al.* [12] has related chip thickness to both the grinding forces and power.

Table 2.2: A comparison of equivalent diameter and chip thickness for different workpiece diameters undergoing the same grinding operation, d_s=254 mm, L=0.1 mm, $\frac{v_w}{v_s} = 5.15 \cdot 10^{-4}$ and a=0.254 mm

Workpiece Diameter	Equivalent Diameter, mm	Chip Thickness, μm
Surface Grinding	254.0	1.27
254 mm (10")	127.0	1.51
127 mm (5")	84.6	1.68
25.4 mm (1")	23.1	2.31

2.4   Analysis of the Grinding Process

Grinding operations are very complex with many variables affecting the process. While there exists computer simulations that estimate forces, power and thermal effects in a cylindrical grinding operation, the results are usually constrained to very specific cutting parameters [13–16]. Experimental results are still needed to confirm these simulations or to develop new ones. This section examines some of the process parameters that are used to analyze a cylindrical grinding operation.

2.4.1   Grinding Forces

Generally the forces are considered in the normal F_n and tangential F_t directions, as shown in Figure 2.9.
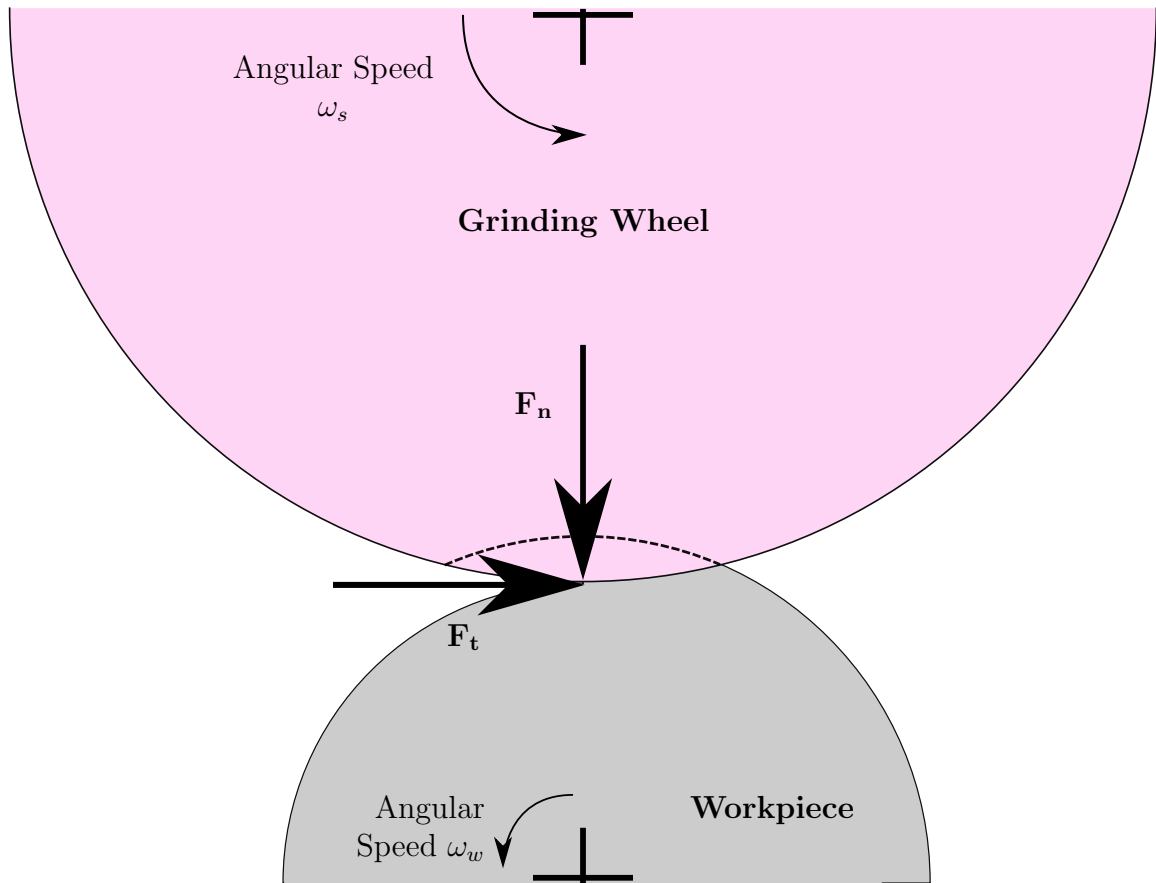
Figure 2.9: The cylindrical grinding geometry

2.4.2 Power and Specific Energy

The power of the grinding operation can be related to the tangential force through the wheel surface speed by using Equation 2.6 [4]. This power can then be used in conjuction with MRR to calculate the specific grinding energy u, as shown in Equation 2.7.

$$P_s = F_t \cdot v_s \tag{2.6}$$

$$u = \frac{P_s}{MRR} \tag{2.7}$$

The specific grinding energy u is the work required to convert a unit volume of material into chips, usually measured in J/mm^3 or $in \cdot lb/in^3$ [9]. The values for specific energy vary with the material, the grinding wheel, and cutting parameters used [9,17]. Table 2.3 gives approximate u values for grinding with various commonly machined metals. These values are taken from Shaw [9].

Table 2.3: Specific grinding energies of various materials, taken from Shaw [9]

| | | u | |
Material	Brinell hardness $(\text{kg} \cdot \text{mm}^{-2})$	$in \cdot lb/in^3 \times 10^{-6}$	J/mm^3
Soft Al	80	5.0	34.5
Hard Al	150	5.0	34.5
Cast iron	215	9.0	62.1
AISI 1020 steel	110	10.0	69.0
Soft A-6 tool steel	240	10.0	69.0
Hard A-6 tool steel	530	10.0	69.0
T-15 HSS	700	12.0	82.7
304 stainless steel	185	12.0	82.7
High-temp alloy	340	12.0	82.7
Titanium alloy	295	10.0	69.0

2.4.3 Surface Roughness

Surface roughness is a measurement of the uniformity of the surface of a workpiece. As grinding is often used as a finishing process, being able to control surface roughness is very important [2]. The typical measurement for surface roughness is the average surface roughness R_a which is the mean value of the average deviation of the surface profile from the centerline of the surface [4]. The surface roughness for grinding operations typically fall in the 0.1 to 1.6 μm range [18].

2.4.4 Roundness Error

Another common measurement of the quality of a cylindrical grinding measurement is the roundness error t_z which is the deviation of a part from a perfect circle. Roundness error is calculated by measuring the radial distance between two concentric circles that

contain the maximum and minimum traces of the shape, as shown in Figure 2.10.
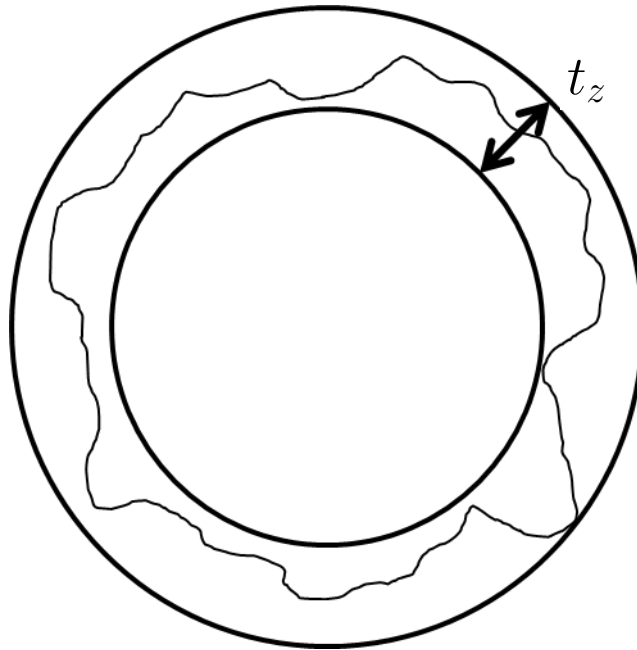
Figure 2.10: Example of roundness error measurement

Roundness is an important dimension in cylindrical grinding because it relates directly to the performance of parts like rolls and crankshafts. Many studies exist that examine the relation of grinding parameters to roundness [19] and the parameters' relative importance [20]. Other papers have examined how to control the roundness [21] and how to measure roundness accurately [22].

2.5 Background Conclusion

This chapter provided the necessary variables and equations to understand the rest of this thesis, particularly pertaining to cylindrical plunge grinding. The effects of the equivalent diameter on contact length and chip size highlighted how different cylindrical grinding is from surface grinding. Finally the important parameters used in later analyses were presented and discussed.

Chapter 3

Literature Review

This chapter will provide an overview of the literature that was relevant to this thesis. The topics include available grinding machine modifications to enable cylindrical grinding, process monitoring techniques used for cylindrical grinding research, types of grooved wheels and their known benefits, and use of grooved wheels in cylindrical grinding.

3.1 Cylindrical Grinding Attachments

Purpose built cylindrical grinding machines, such as the one shown in Figure 3.1, required a prohibitive capital expense; therefore, it was decided that modifying the existing grinding machine with a rotary axis was the only practical option.

Figure 3.1: A Studer S30 conventional cylindrical grinding machine [23].

Commercial rotary axes for milling machines do exist but their speed range of 0-70 rpm is too low for grinding [24–26]. After an exhaustive search only two machines that were designed for cylindrical grinding were found [27, 28]. The two options, shown in Figure 3.2, were excluded for reasons of cost and capabilities. Specifically, the Harig machine could not withstand coolant spray, and the Newbould machine's cost of $7,895.00 USD was beyond the project budget. The lack of commercially-feasible options meant that the rotary axis would need to be a custom design, which is a common route taken in the literature [16, 29–31].
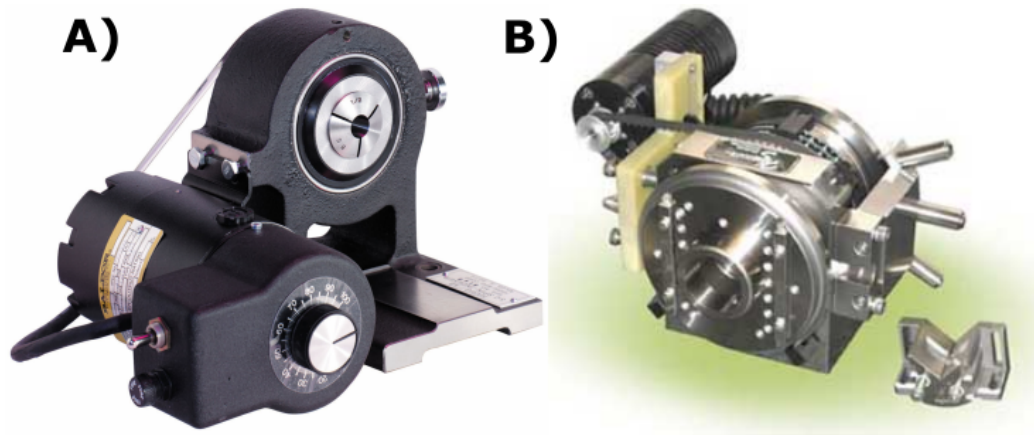
Figure 3.2: The two commercially available rotary axes found. A) is the Harig Spin Indexer [28] and B) is the Newbould Grindit [27].

3.2 Monitoring the Grinding Process

The rotary axis had to not only enable cylindrical grinding, but also allow for the in-process measurement of the grinding operation. According to a summary paper by Tonshof [32], the grinding process can be monitored through the use of force sensors, power sensors, accelerometers, acoustic emission, and temperature sensors. It was decided that force and power monitoring would be the focus of the rotary axis because the Grinding Lab has had a history of success in capturing and analyzing these parameters.

Monitoring the process power is technically straightforward and involves measuring the power sent to the grinding wheel spindle motor, as was done by Mohamed *et*

al. [33]. Force monitoring is more difficult because the sensor must be located on or near the grinding zone and the detection methods reflect this added complexity. The first force monitoring experiments were performed in 1952 by Marshall and Shaw using strain gauges [34], but the machine stiffness had to be dramatically reduced to incorporate them which affected the grinding process. The introduction of the piezoelectric dynamometer allowed for force monitoring without adversely affecting machine stiffness which then became a commonly used method [29, 35–37]. Other force monitoring systems exist, such as the magnetostrictive transducers used by Flatau *et al.* [38] and eddy current sensors used by Jenkins and Kurfess [39], but they are less common.

The rotating workpiece in cylindrical grinding further complicates force monitoring compared to surface grinding. There exists rotary non-contact force dynamometers such as the Kistler 9171A but many systems simply place a three-component dynamometer below the entire rotary axis. Figure 3.3 shows example setups by Choi *et al.* (left) [16] and Drew *et al.* (right) [30]. Some advantages of this method is the large range of forces and high bandwidth that can be measured, as well as the fact that high-precision three-component force dynamometers are readily available and well understood.
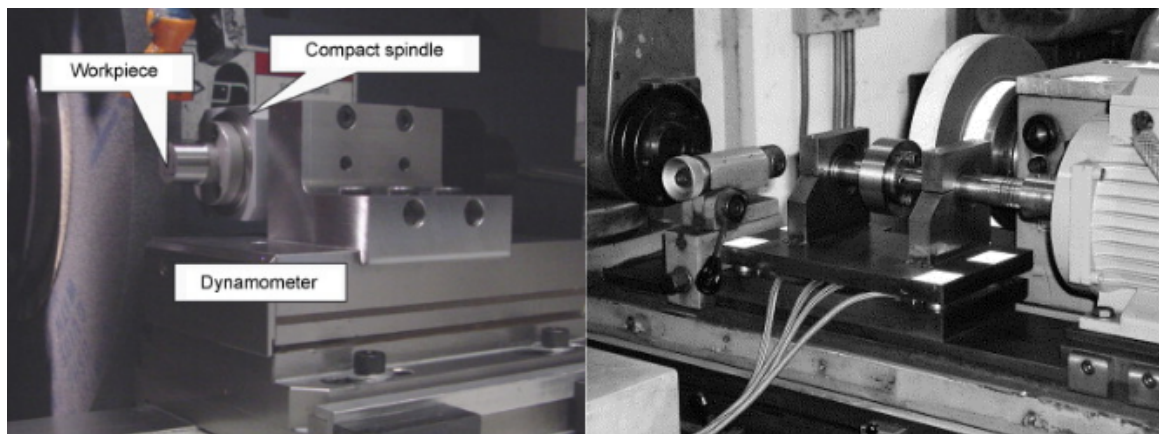
Figure 3.3: Two examples of three component dynamometers used to measure in-process cylindrical grinding forces. Left is taken from Choi *et al.* [16] and right is taken from Drew *et al.* [30].

Force monitoring has been successful at a small scale as well. Couey *et al.* [29]

have equipped an aerostatic spindle with non-contact displacement sensors that can convert the distance between rotor and stator to the grinding force of the process. This system was designed to monitor forces in ultra-precision cylindrical grinding, can detect the lower forces involved in this process, has a resolution of 25 mN, and has a bandwidth of 300 Hz. Their system has been successfully used to explore form error in plunge cylindrical grinding [37].
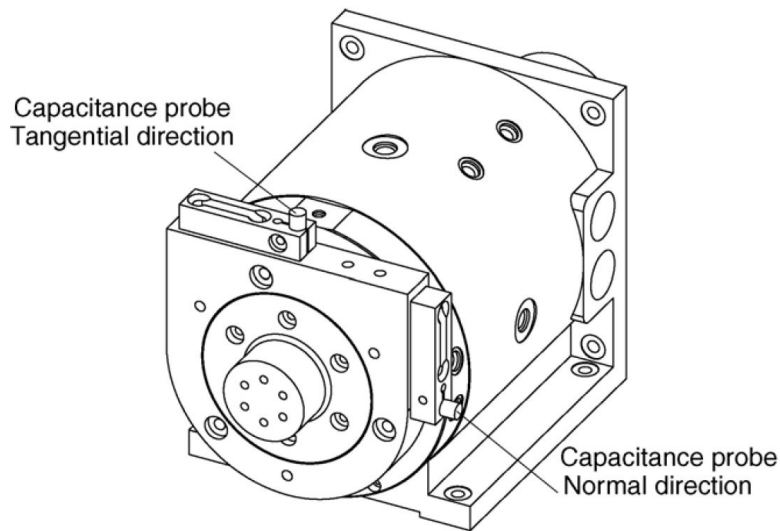
Figure 3.4: The aerostatic spindle used be Couey *et al.* to measure cylindrical grindign forces [29].

Another important force monitoring experiment in cylindrical grinding was performed by Ramos *et al.* [31]. They used an LVDT to measure the normal force during grinding and used that data to experimentally determine the cutting stiffness and the contact stiffness of the grinding process. One drawback of their system is that it was only capable of monitoring the normal force and, therefore, the tangential force had to be determined through the spindle power.

To summarize, the requirement of building a custom rotary axis causes research into cylindrical grinding to be less common than surface grinding. However, there are examples of successful force monitoring in cylindrical grinding, specifically using three component force dynamometers. The production of a simple, low-cost, instrumented rotary axis would make research into cylindrical grinding more accessible.

3.3 Grooved Grinding Wheels

An important development in grinding wheel technology is the addition of grooves to the surface of the grinding wheels. This particular type of wheel modification first appeared in the literature in 1977 with a study by Nakayama *et al.* [40] who found that a helical groove pattern could effectively lower energy consumption without increasing surface roughness and wheel wear.

A helical groove pattern, however, is only one of many potential patterns, three more of which are shown in Figure 3.5. By varying the angle of the grooves the axial (a), helical (b), and circumferential (c) groove patterns can be produced. Verkerk [41] developed a useful way to quantify groove patterns through the groove factor η. η, given in equation 3.1, is the ratio of un-grooved surface area to the total surface area A_o, where A_g is the area of the grooves. The groove factor is an important term used to compare different grooving patterns and is used to correlate groove pattern to grinding behavior.
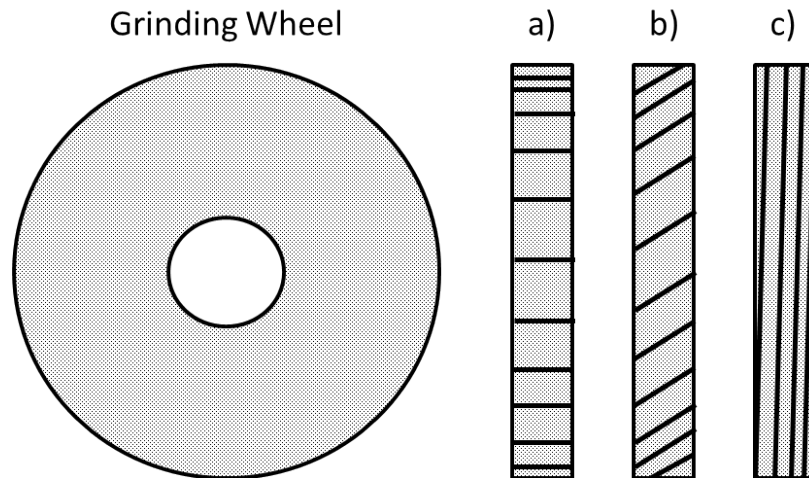
Figure 3.5: Three common types of grooved grinding wheel, a) axial, b) helical, and c) circumferential

$$\eta = \frac{A_o - A_g}{A_o}\%$$
(3.1)

3.3.1 Effects of Grooved Grinding Wheels

A summary of the effects of grooved grinding wheels on the grinding process was written by Forbrigger *et al.* [42]. Having looked at the results of research papers published between 1977 to 2015 that examined a broad range of groove patterns, Forbrigger *et al.* found that grooved wheels conclusively reduced specific energy [43–49], grinding forces [40,46,48–52], and process temperature [40,41,43,45,48,49,51,53]. However the findings for grooved wheel wear varied from no effect [40, 48, 52] to an increase in wear [41, 49]. More interestingly, three studies found a reduction in workpiece finish [49,53,54] while seven studies found that surface roughness increased [41, 44, 47, 48, 50–52]. An explanation for these discrepancies is still unavailable.

3.3.2 Workpiece Texturing

Another effect of using grooved wheels is that they have been shown to impart a texture to the surface of the workpiece [47, 55, 56]. Suh *et al.* [57] showed that workpiece texturing can lower frictional coefficients, and Byun *et al.* [58] showed enhanced tribological properties. The paper recently completed by Mohamed *et al.* [55] provides an analytical model and a simulation that can accurately predict the texture on a flat workpiece when using circumferentially grooved wheels. An example of the texture produced is shown in Figure 3.6.
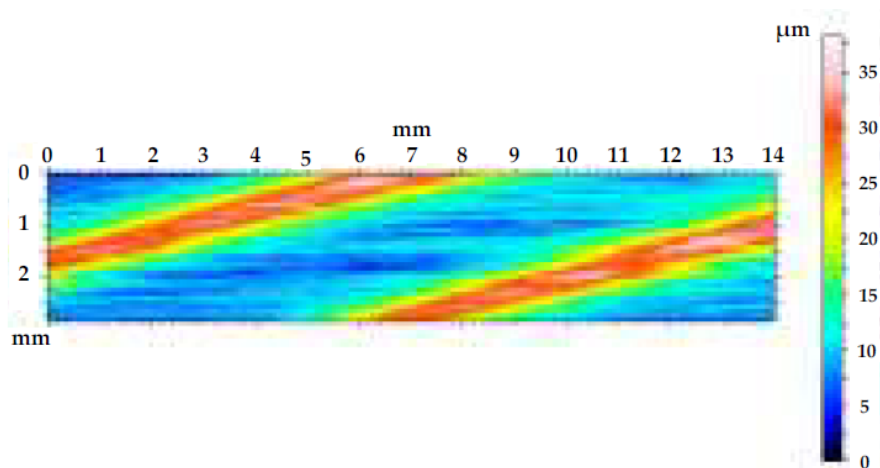
Figure 3.6: An example of a workpiece texture produced using a circumferentially grooved wheel, adapted from [55].

3.3.3 Circumferentially Grooved Wheels

Recently the Grinding Lab has had success in studying circumferentially grooved grinding wheels [33, 48, 55]. An initial study showed that circumferential grooves improve grinding efficiency, reduce workpiece burn, and increase the the achievable depth of cut in creep-feed grinding [48]. The circumferential grooves were also applied to the workpiece without modifying the grinding machine by using a single point dressing tool [48].

The next study further explored the reason for the increase in efficiency and found a 6-8 fold increase in chip thickness h_m and improved coolant flow [33]. The most recent study was able to apply textures to the workpiece (Figure 3.6) and develop a simulation to predict said textures [55]. Overall, this research into this groove pattern shows promising benefits to the grinding process, and has never been applied to cylindrical grinding.

3.3.4 Cylindrical Grinding and Grooved Wheels

Grooved wheels and their application to cylindrical grinding has not been extensively studied. There have been two studies that examine the effects of helical grooves [49,54] and one study that looked at textures that can be produced by grooved wheels [47].

The texturing study by Olivera *et al.* [47] examined a variety of modifications to the wheel face (Figure 3.7 (A)) and their ability to apply a texture to the workpiece (Figure 3.7 (B)). Only two of the wheel modifications could be considered grooved patterns, both of which were helical grooves. The study also showed a reduction in power consumption when using modified wheels.
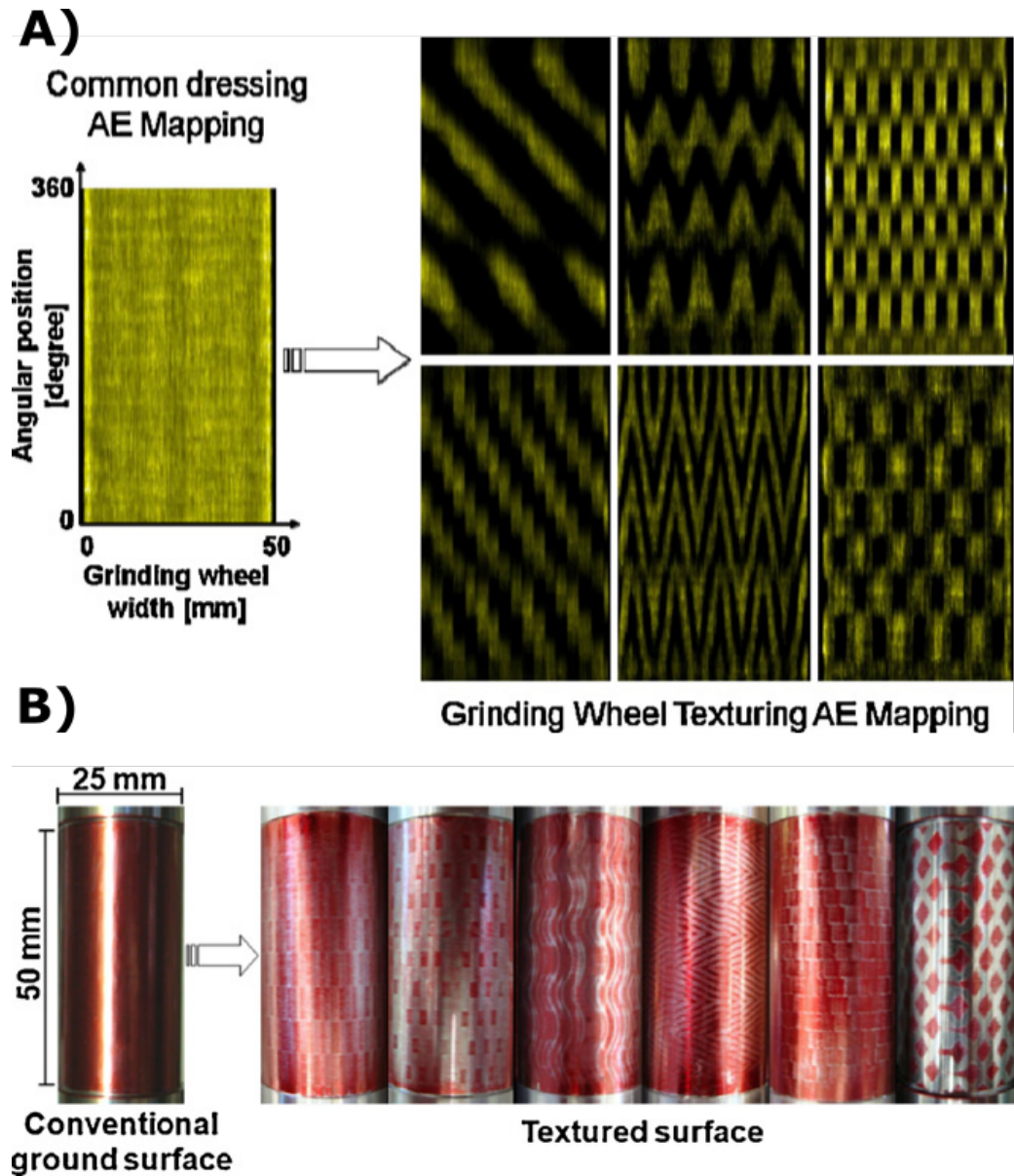
Figure 3.7: The various wheel modifications (A) studied by Olivera *et al.* and their resulting textures (B). Taken from [47].

The research done by Koklu [54] looked into how different angles of helical grooves affect surface finish, dimensional accuracy, and residual stresses for a variety of cylindrical parts. Koklu found that helically grooved wheels improved both the roundness and surface roughness of the workpiece, and that different groove angles performed better for different material hardness values. The other helical groove study by Uhlmann and Hochschild used a rotating dynamometer to monitor forces

during cylindrical plunge grinding, shown in Figure 3.8 [49]. Uhlmann and Hochschild showed an improvement to grinding forces, power, and workpiece temperature, but an increase in wheel wear.
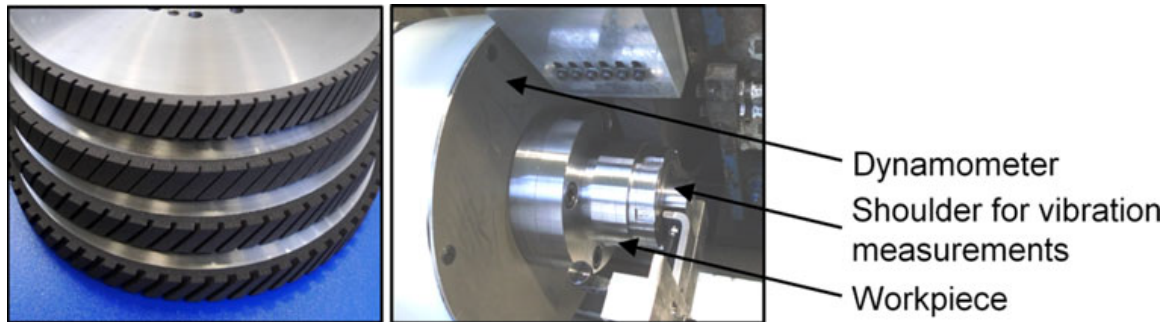
Figure 3.8: The helicallly grooved wheels and force monitoring apparatus used by Uhlmann and Hochschild. Taken from [49]
.

3.4   Summary of Literature Review

To summarize the findings of this literature review, the added complexity of cylindrical grinding from both its requirements for a rotary axis that is likely custom made and the difficulties in instrumenting said rotary axis have made research into this important industrial process scarce. The research is especially lacking surrounding the effects of grooved grinding wheels, particularly the circumferentially grooved wheels that shown promising results in the Grinding Lab. After this review it can confidently be said that an instrumented rotary axis would help the Grinding Lab produce unique and cutting-edge research.

Chapter 4

Rotary Axis

To enable the Grinding Lab to research cylindrical grinding a rotary axis attachment was required for the Blohm Planomat surface grinder. A custom rotary axis attachment was designed, built, and validated as a key component of this thesis. This chapter discusses said attachment, and gives the relevant details on its design and capabilities.

4.1 Design Requirements

The rotary axis was designed to work with the Grinding Lab's existing equipment and to serve as a capable, research-grade machine. To this end, six key design requirements were chosen in the following areas.

1. Achievable speed range and speed regulation

The first design requirement is that the workpiece can rotate at any speed from 0-500 rpm. This range was chosen from examining relevant literature and existing machinery. For example, to achieve the material removal rates (MRR) used in papers by Biera *et al.* [59], Weck *et al.* [60], and Koklu [54] a 1" (25.4mm) workpiece would have to rotate at 355 rpm. Furthermore, this speed range is the same as the fastest available commercial machine, the Newbould Grindit [27]. A secondary aspect of this requirement is that the speed is not allowed to fluctuate under a grinding load. To guarantee an accurate and stable speed there must be less than a 1% variation in workpiece speed under grinding conditions and the actual speed must be within 1% of what was commanded.

2. Sufficient workpiece torque

To maintain a steady workpiece speed under a grinding load the motor must have sufficient torque. The maximum torque required was determined by assuming a tangential force of 150 N on a 1" (25.4 mm) workpiece. This load was taken from previous grinding experiments performed in the Grinding Lab, and was considered an overestimate of the expected force. The motor must be able to apply this torque at a workpiece rotational speed of 500 rpm.

3. Ability to measure in process forces

The rotary axis is meant to measure the forces in the grinding process; therefore, it must be able to accurately measure the grinding forces in all axes. To meet this requirement the rotary axis must be able to accurately measure known loads on the workpiece to within 1% in all axes.

4. High natural frequency

For the rotary axis' dynamic behavior to not interfere with the grinding force measurements its natural frequency must be significantly higher than any excitation frequency in the grinding process. To meet this requirement the dynamic behavior must be measured and the nearest natural frequency of the rotary axis must be an order of magnitude larger than the highest grinding excitation frequency.

5. Waterproof machine

The grinding machine that the rotary axis is designed to use is equipped with a coolant delivery system. To be able to operate in this environment the rotary axis must be able to withstand direct coolant spray and grinding debris without any adverse effects to the rotary axis or its ability to measure forces.

6. Safe to operate

The final requirement is that the rotary axis is safe to operate. There are powerful motors and power supplies involved; therefore, all dangerous equipment must be properly isolated and there must be an easily accessible emergency stop.

4.2   Description

The rotary axis machine built to meet these requirements has three main components: the rotary axis, the main electrical box, and the speed controller, as shown in Figure 4.1, along with the most important sub-components and how they communicate. Each component will be discussed in the following subsections, and a complete list of components used is available in Appendix A.

Speed Controller

Rotary Axis

Main Electrical Box
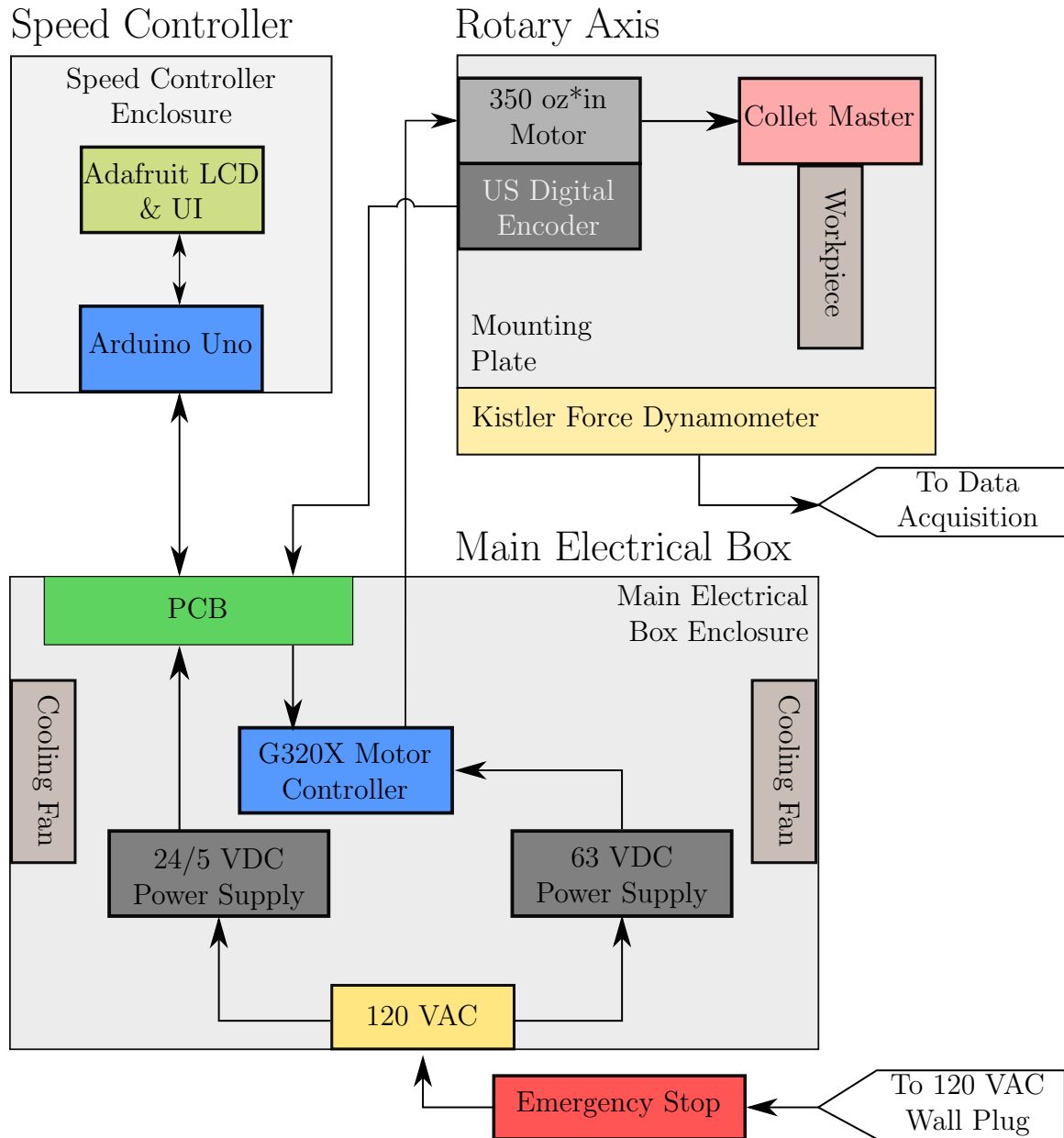
Figure 4.1: A block diagram of the three components of the rotary axis, with arrows showing communication

4.2.1 Rotary Axis

Figure 4.2 shows the rotary axis installed in the grinding machine. The workpiece mount consists of a Collet Master (A), from Suburban Tool Inc., attached to a Kelling 350 oz·in (2.47 N*m) brushed motor (B) via a timing belt with a 6.5:1 ratio. These components are all mounted atop a $^1/_2''$ (12.7 mm) stainless steel plate. The plate, in

turn, mounts to the Kistler 3-axis force dynamometer (C), model 9257b.
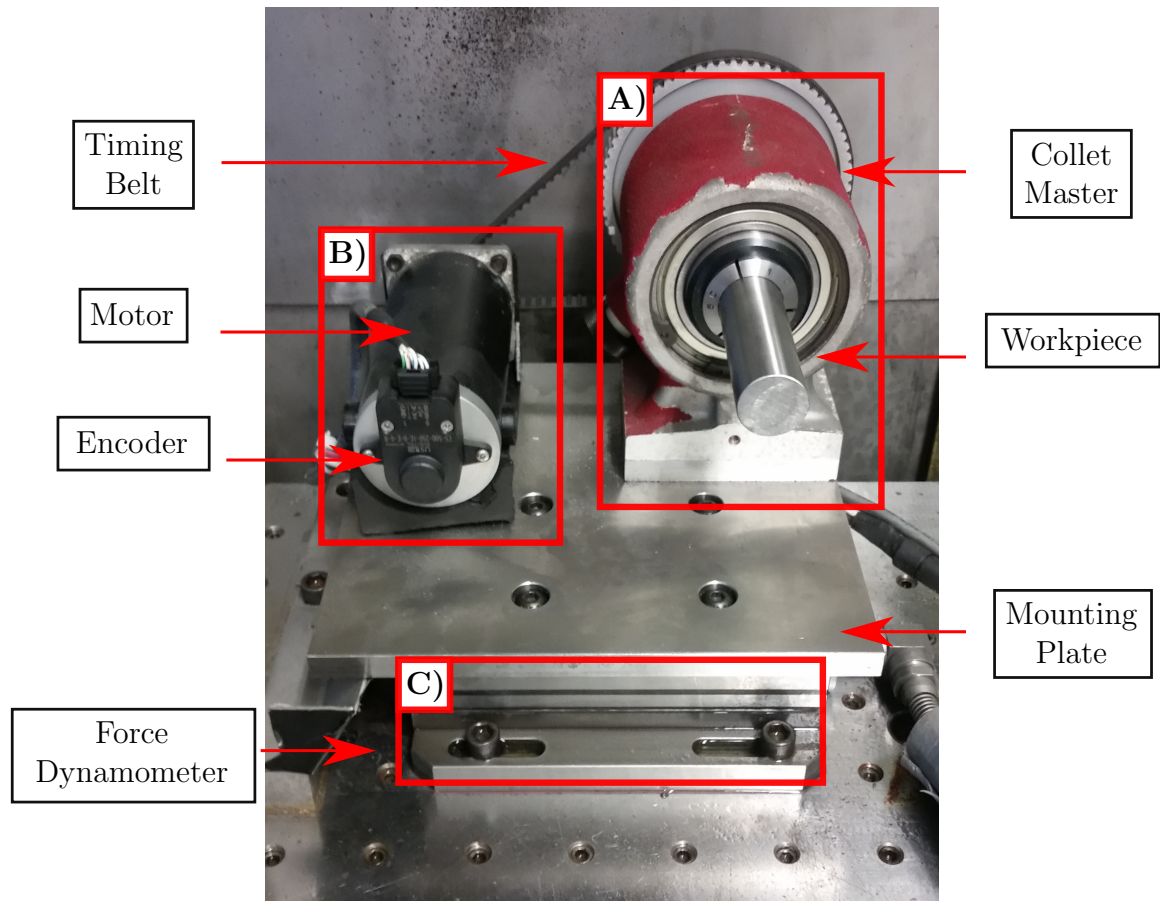
Figure 4.2: The inside of the rotary axis showing; A) the Collet Master with timing belt, B) the motor and encoder, and C) the force dynamometer

The Collet Master was chosen for its sealed bearings, allowing for lubricated experiments, and its low runout of $\pm 0.00005''$ ($\pm 1.27\,\mu m$). It can hold workpieces up to $1''$ in diameter using standard 5C collets. To help maintain the dimensional accuracy of parts ground on the system the mounting plate had to be ground to very fine tolerances. Using a dial indicator the ground plate was found to be within $0.0002''$ over $8''$ (5.08 μm over 203.2 mm). Finally, to enable feedback to the control system a 500 count differential rotary encoder from US Digital was attached to the motor.

To enable aggressive grinding experiments to be performed, the motor had to be sized and geared accordingly. The selected motor has a maximum torque of 2.47 N·m and a no-load speed of 4700 rpm. With the 6.5:1 gear ratio this gives a maximum

torque at the workpiece of 16.2 N·m and no load speed of 720 rpm. Figure 4.3 gives the available torque curve to the rotary axis, as well as the expected operating area of the rotary axis. The expected operating area's torque and speed range come from the design requirements. Figure 4.3 shows that there is ample torque supplied to the workpiece to enable fast and accurate speed control during operation.
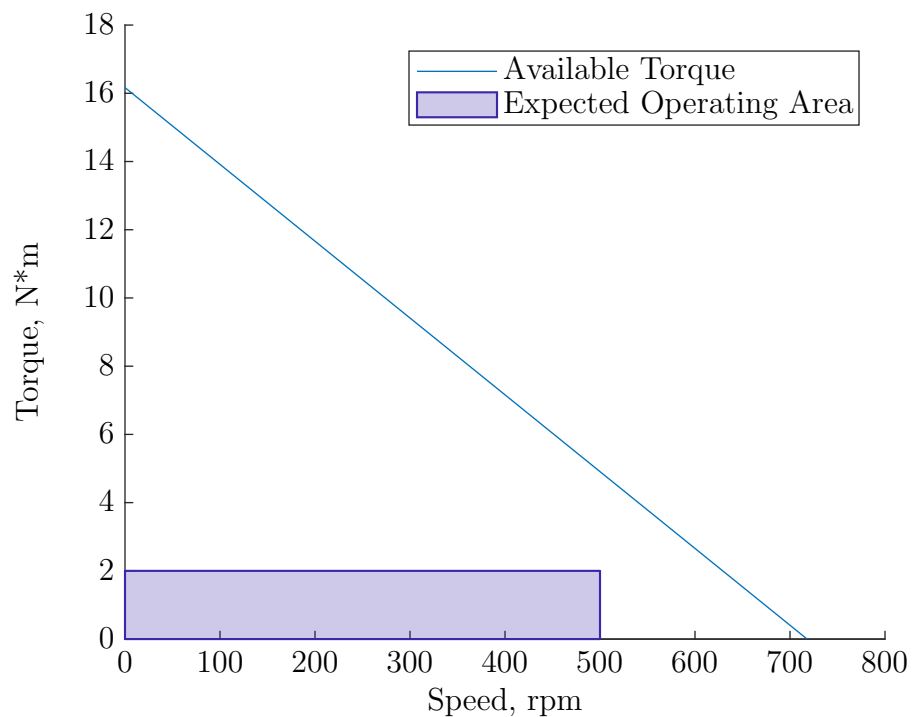
Figure 4.3: The torque curve of the rotary axis.

4.2.2 Main Electrical Box

The main electrical box is $18'' \times 18'' \times 8''$ and houses a 63 VDC, 1 kW power supply for the motor, a 24 VDC\5 VDC power supply for all other components, the motor controller, a PCB to sort inputs and outputs, and two fans for cooling. Figure 4.4 shows inside the main electrical box. The line diagram for the box is shown in Appendix Figure B.1.
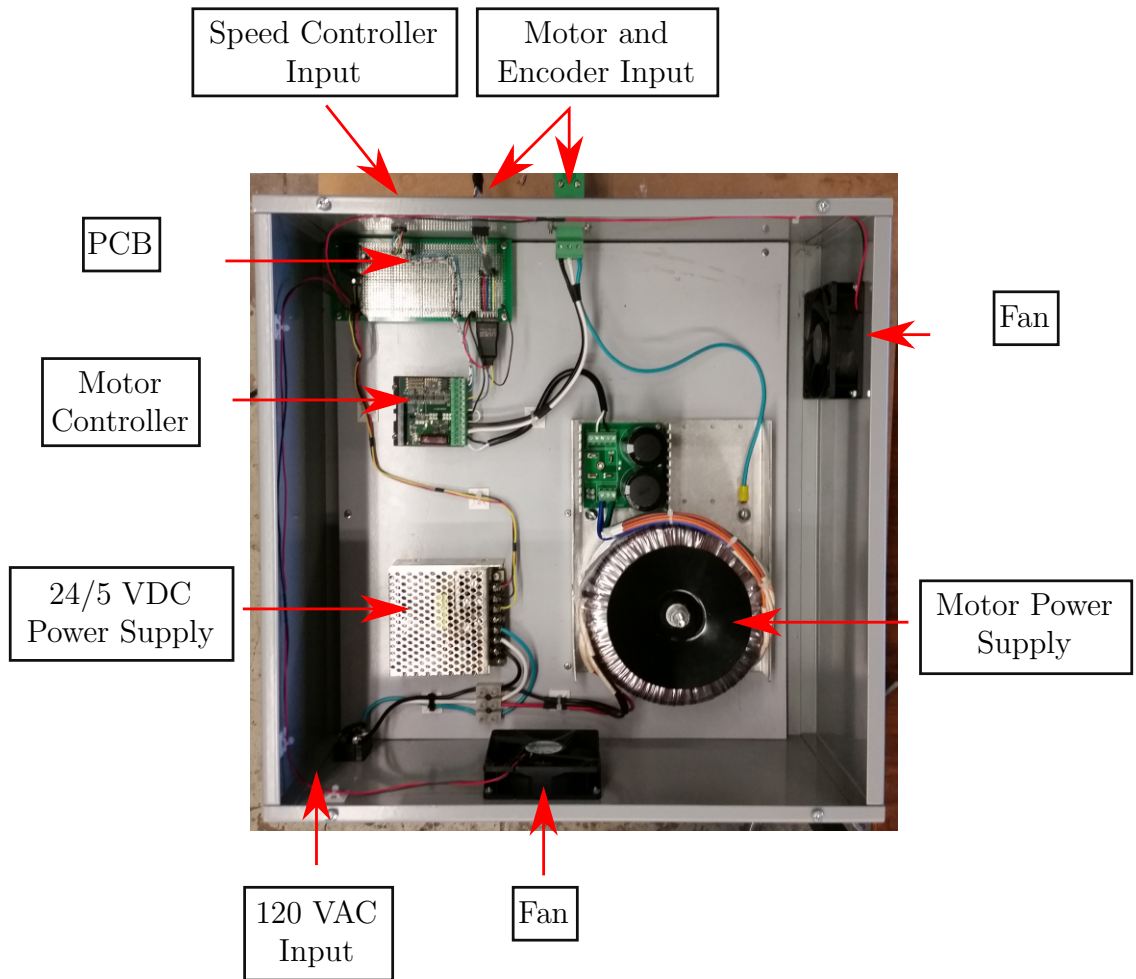
Figure 4.4: The inside of the main electrical box

The speed is controller by a G320x model digital servo motor drive from Geckodrive Motor Controls. This drive features a PID control system with each term adjustable using trim pots on the board. Using an oscilloscope it is possible to view the response of the motor driver to a load. For the purpose of tuning this load was simulated by reversing the direction of the motor when the workpiece was turning at 100 rpm, as this was recommended by the manufacturer.

The system response to tuning is shown in Figure 4.5, the bottom line of the oscilloscope reading is the input to the system, while the top line is the system's response. The system intial response to the input was very under-damped. Figure 4.6 shows the response of the system after tuning; here, there is little overshoot and no excessive oscillation. The response is also greater than three times faster than the

original tuning, reaching a steady state in 60 ms instead of 200 ms. The system could have been further tuned to an even faster response, but over tuning led to excessive motor dithering (the rapid movement of the motor between encoder counts).

100 ms/block
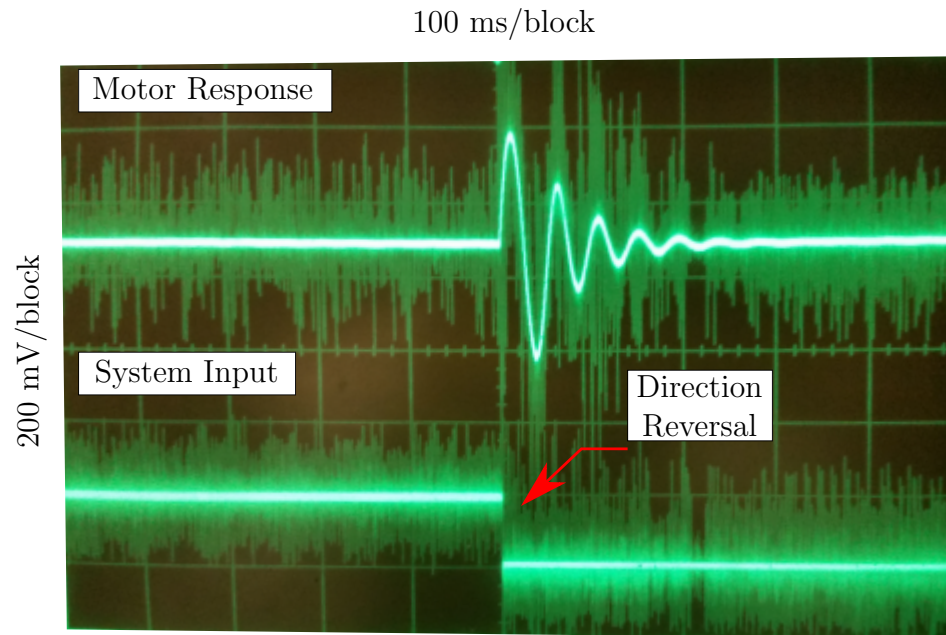
Figure 4.5: The initial response of the motor controller, top, to the input, bottom.

20 ms/block
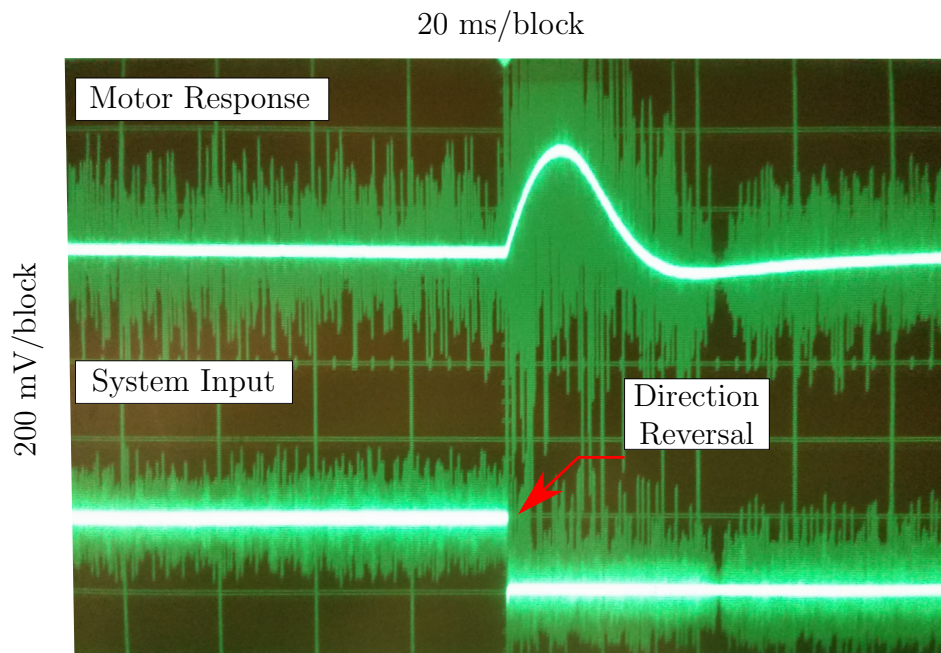
Figure 4.6: The response of the system after final tuning

4.2.3 Speed Controller

The speed controller is used to send square wave pulses and a directional signal to the motor controller. These signals are sent using an Arduino Uno R3 with a LCD keypad shield from Adafruit which is mounted to a 3D printed faceplate, as shown in Figure 4.7 (left). The speed controller itself is mounted on top of the grinding machine controls for ease of use, Figure 4.7 (right).

Figure 4.7: The speed controller, left, and its location, right.

4.2.4 Waterproofing

The motor and timing belt had to be protected from coolant and grinding debris. The Collet Master was not a concern becasue it was designed to work in a grinding environment. The waterproofing consisted of two parts: a custom aluminum enclosure and a plastic covering for the motor itself.

The aluminum enclosure, shown in Figure 4.8 A), was designed to deflect direct spray from the motor and timing belt. The inside of the enclosure was designed to separate important sections of the rotary axis to help further reduce spray and grit from reaching the timing belt and motor. Figure 4.8 B) shows the three different sections. It was also important that this enclosure did not adversely effect the

performance of the rotary axis. To this end a covered access panel, shown in Figure 4.8 C), was built so workpieces could still be removed and installed without removing the enclosure. Also to prevent the enclosure from effecting force measurements it was mounted to the grinding machine's mounting plate and had no direct contact with the rotary axis or force sensor. The last waterproofing line of defense is a plastic bag with waterproof tape for the motor and encoder to prevent moisture ingress.
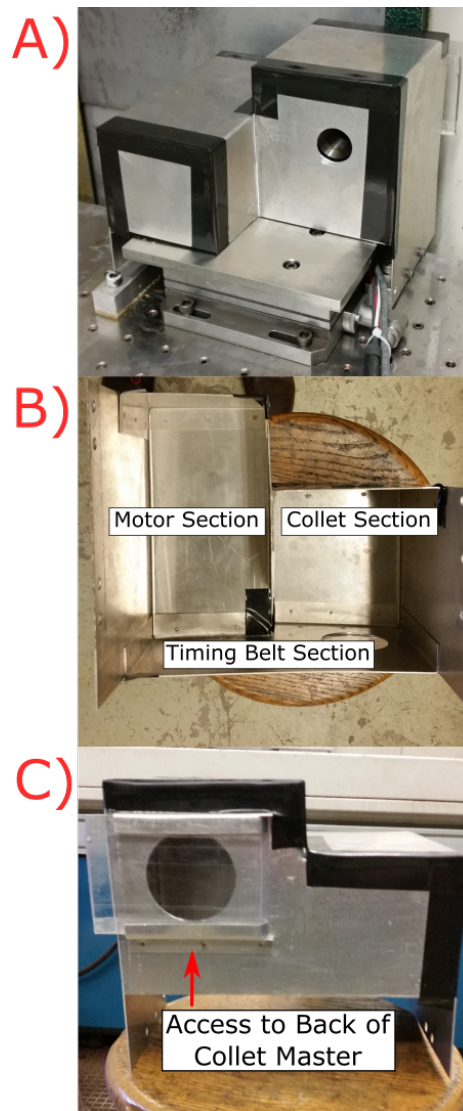
Figure 4.8: Aluminum waterproofing box showing: A) installed, B) internal sections to help prevent water ingress, and C) back access panel to Collet Master for workpiece changing

While the waterproofing is difficult to validate quantitatively, qualitatively it has

performed quite well. After more than 50 lubricated grinding experiments there have been no noticeable effects to the rotary axis' operation and no evidence of water inside the plastic bag.

4.2.5 Safety

Machine safety was an important design consideration for the rotary axis. The existing safety mechanisms of the grinding machine covered most important aspects; however, there are two that were built for the rotary axis. First, the rotary axis had to be able to shut down rapidly in case of emergency. The power switch for the rotary axis also serves as an emergency stop switch. Shown in Figure 4.9, the panel switch is located close to the door of the grinding machine, within easy reach when operating the machine. When hit, it stops the workpiece rotation in under one second. Second, the main electrical box is CSA approved, properly grounded and isolated, and all components have been rated for their respective voltages.

Figure 4.9: Emergency stop switch

4.3 Rotary Axis Validation

The attachment was extensively tested for its capabilities. These tests included speed range and accuracy, vibration testing, and force measurement abilities. This section looks at these tests and their results in detail.

4.3.1   Speed

One of the most important features of this rotary axis is the range of speeds over which it can be used and its ability to maintain its speed under grinding load. To test the speed range, a simple benchtop experiment was set up by mounting a $1''$ plain carbon steel workpiece, commanding various speeds and confirming them using a hand-held tachometer. Speeds from 5-600 were successfully confirmed which is greater than the required range.

A more involved experiment was used to determine how the rotary axis reacted under load. One of the encoder differential channels was captured using a BNC-2120 data acquisition unit from National Instruments. The signal was first processed by a INA128P low power instrumentation amplifier to filter out noise. This encoder pulse train could then be converted to speed and used to detect changes under load on a small timescale. In order to apply a load to the workpiece an aggressive plunge dry grinding operation was performed with angular workpiece speed ω_w of 300 rpm and an infeed rate v_f of 0.16 thou/rev (4.06 μm/rev).

The results this experiment showed little to no noticeable deviation from the expected pulse train. Figure 4.10 shows the results in three different graphs. The top graph gives the measured spindle power over time. With a maximum power of 730 W during grinding wheel engagement; this test is a good representation of aggressive plunge grinding. The middle graph shows the encoder pulse train converted into speed as well as the commanded speed over the same time period as the power graph. It was found that the mean ω_w during the experiment was 301.02 rpm and the standard deviation was 2.13 rpm, or 0.71% of the commanded speed. This range was considered acceptable. The bottom graph gives a closer look at the same pulse train, which shows more clearly that there is little change in speed or response during this plunge grinding experiment.
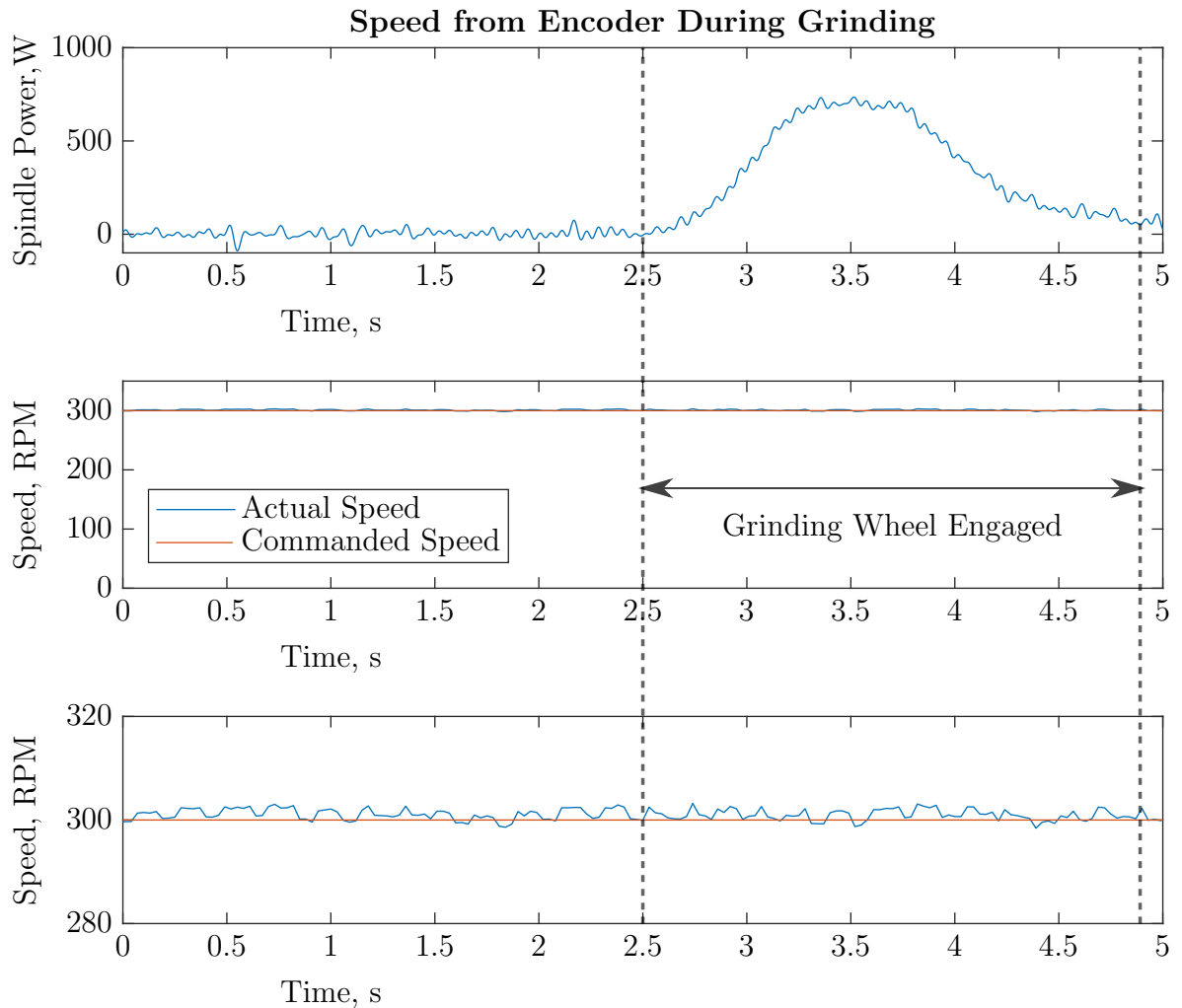
Figure 4.10: Workpiece speed validation graphs. Top, the spindle power during plunge grinding operation. Middle, the commanded and actual v_w during the same grinding operation. Bottom, close up of v_w.

4.3.2 Forces

To test the ability of the rotary axis to accurately measure forces in all axes two simple experiments were performed. First, the calibration of the force dynamometer in the z axis (the normal force) was tested. A weight was measured using a Sartorius LP1200S scale. A known load of 25.7 N was then applied to the mounting plate and the workpiece. Figure 4.11 shows the result of this test. The force dynamometer read 25.72 N on the plate and 25.67 N on the workpiece. This proves that the normal force measurements are accurate and not effected by the location of the workpiece.
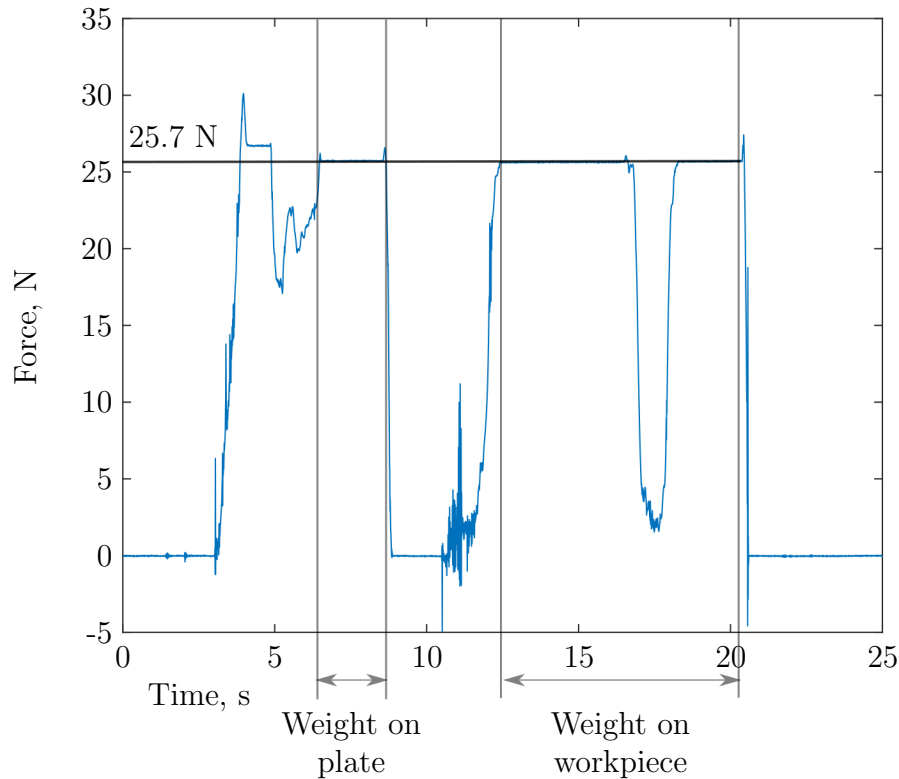
Figure 4.11: Test to see if F_n is read the same directly on the mounting plate as on the workpiece.

To test the tangential F_t and radial F_r the weight was applied to the workpiece through the apparatus shown in Figure 4.12 (here set up to measure F_t). Examining the results for F_t, Figure 4.13 shows the curve after applying a 4.45 N load to the workpiece. The measured F_t values ranged from 4.31-4.57 N, but had a mean value of 4.43 N. This larger variation in measured forces is attributed to friction and elasticity in the experimental apparatus, however this setup was deemed sufficiently accurate. In the axial direction F_r the range of results was 4.29-4.58 N with a mean of 4.46 N. These results together prove the force dynamometer is capable of accurately measuring forces in all three axes.

Figure 4.12: Experimental setup to test F_t axis.
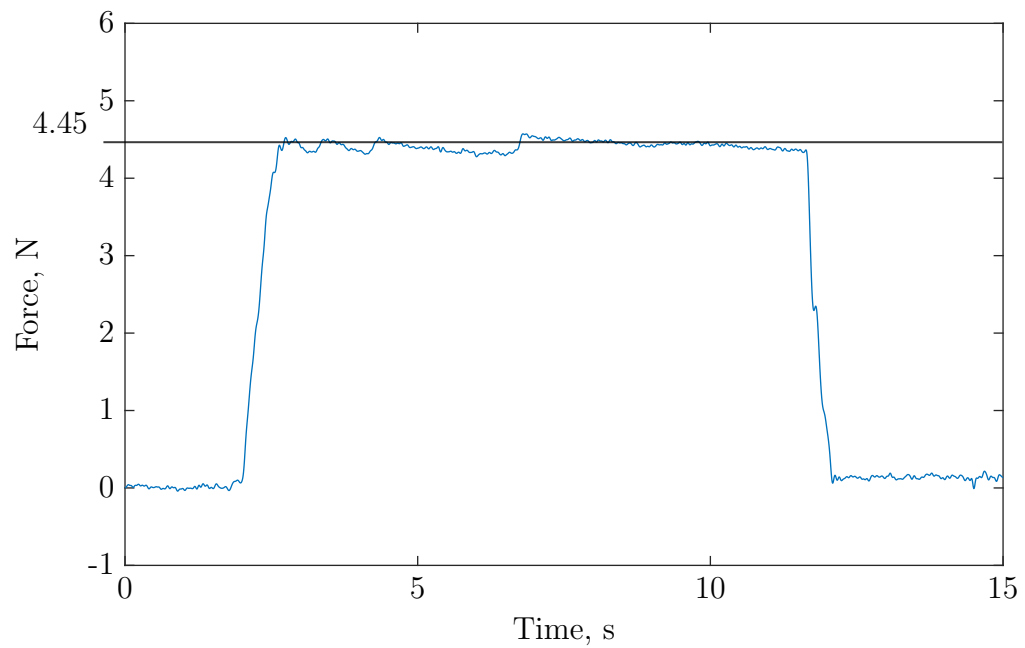
Figure 4.13: The tangential force calibration plot showing the measured force and the expected 4.45 N force.

4.3.3   Vibration

The following work was done to characterize the dynamic characteristics of the system. First, the important dynamic features were identified, shown in Figure 4.14. Another grad student, Zhipeng Sun, performed hammer tests on the individual components of the system [61]. His findings are summarized in Table 4.1. His research showed that the natural frequency of the Collet Master is significantly higher than the dynamometer and, therefore, not a concern. Also, because the motor's natural frequency was so low a rubber motor dampener was added to the system, as shown in Figure 4.14.
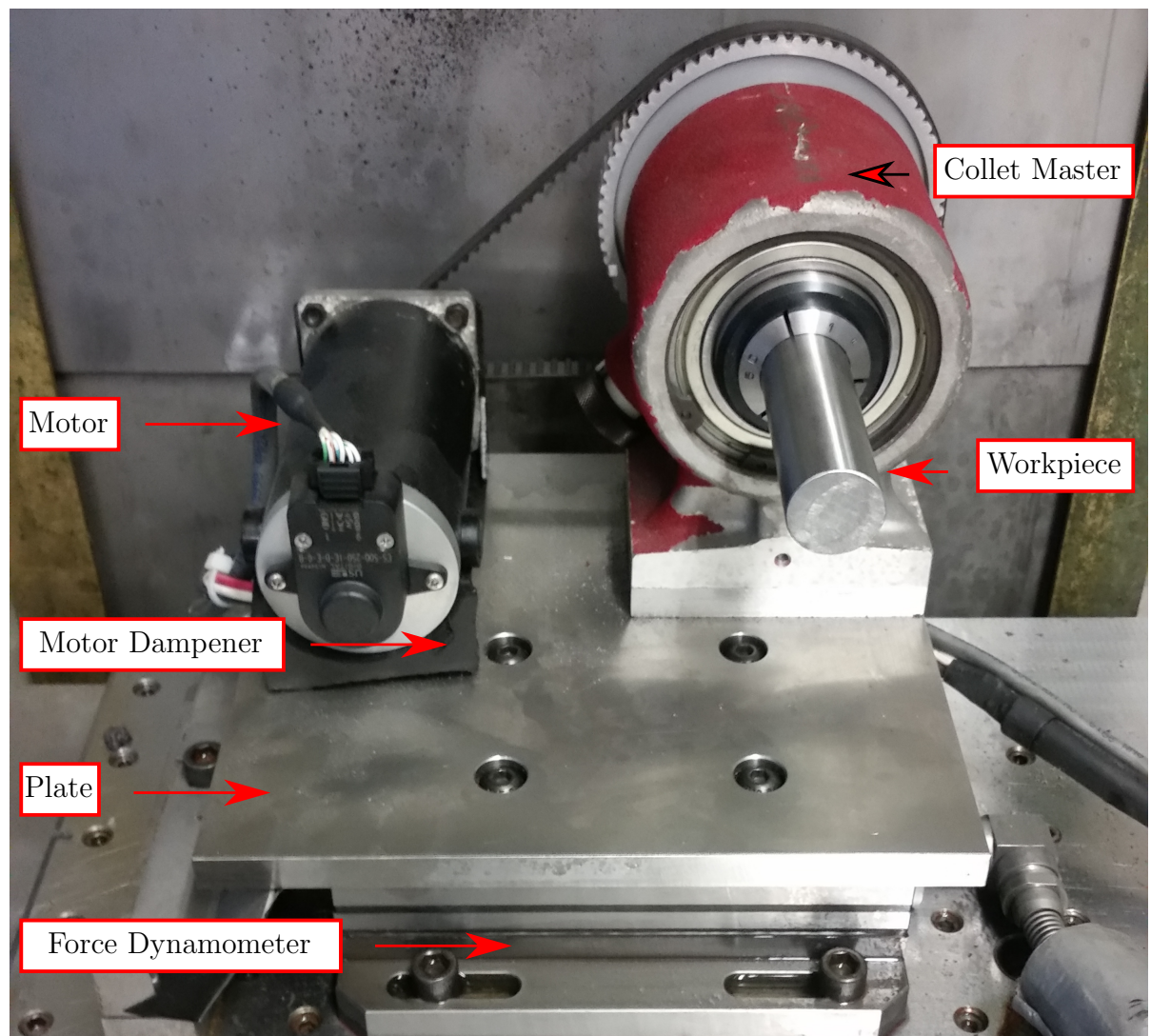
Figure 4.14: Important dynamic features on the rotary axis.

Table 4.1: The individual natural frequencies of the rotary axis' components [61].

Component	Natural Frequency, Hz
Motor	75
Plate	330
Workpiece (6" overhang)	510
Dynamometer	3150
Collet Master	5350

System excitation while using the rotary axis in grinding can come from a combination of four sources: the workpiece rotation, the grinding wheel rotation, the motor rotation, or the impact of individual abrasive grains. The excitation frequencies of the rotating components for a plunge grinding operation at a workpiece angular speed of 300 rpm are given in Table 4.2. To help minimize the power of the excitation all the rotating components have been balanced within reasonable tolerances. The impact of the individual abrasive grains behaves more like a white noise and could potentially excite a broad range of frequencies.

Table 4.2: The potential excitation sources and their frequencies during plunge grinding at a workpiece angular speed of 300 rpm.

Excitation Source	Frequency, Hz
Workpiece Rotation	5
Grinding Wheel Rotation	16
Motor Rotation	32.5
Abrasive Grain Impact	White Noise

To analyze the dynamics of the system as a whole a fast fourier transform (FFT) was performed using data collected from grinding experiments. The results are shown in Figure 4.15. There are peaks at 360 Hz and 730 Hz, associated with the mounting plate and the workpiece respectively. The reasons these frequencies differed from the findings of Zhipeng Sun are that the workpiece was shorter in the FFT test (4" overhang vs. 6" overhang) making it stiffer, and a tighter mounting of the plate to the force dynamometer increased its associated frequency. The rubber motor dampener is also the reason there are no peaks associated with the motor. Figure 4.15 also gives lines marking the rotational excitation frequencies given in Table 4.2. These

excitation frequencies are much lower than the nearest natural frequency (the plate) which means they are unlikely to cause excessive vibration.
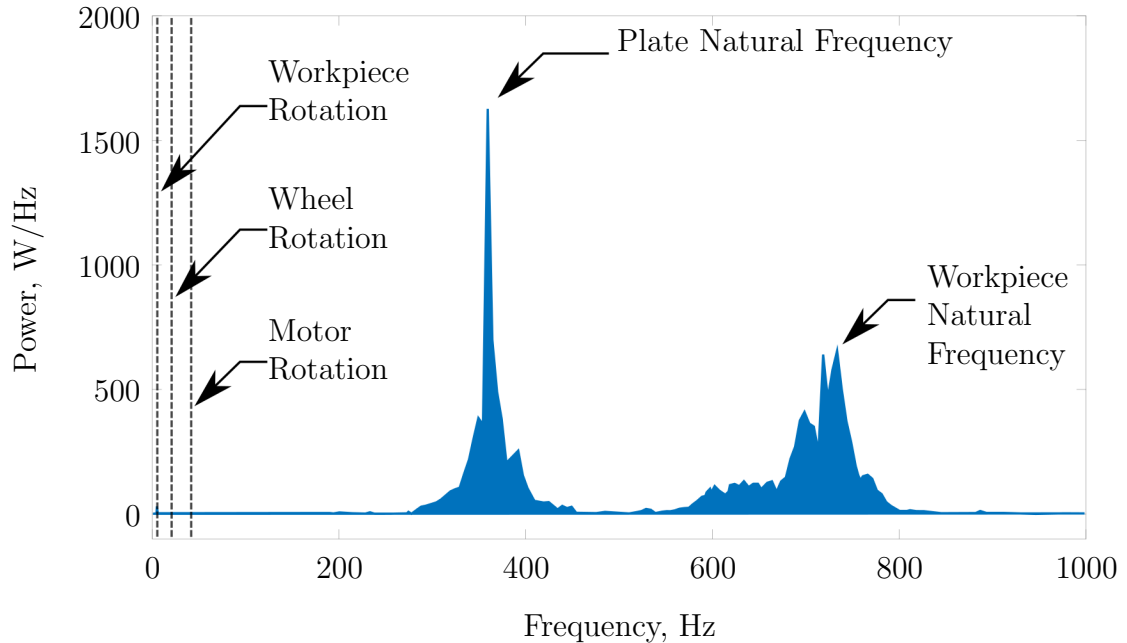
Figure 4.15: The FFT of the Rotary axis showing the peaks of the plate and workpiece, as well as the excitation frequencies from the rotating motor, grinding wheel, and workpiece.

These results lead to two discussions: how best to use the system as it currently behaves, and what further improvements could be made. As for the system as is, it performs quite well but the raw force data it receives is quite noisy. To interpret this raw data a low pass filter was applied to all dynamometer measurements to allow for the important trends to be observed. The cutoff frequency for this filter was chosen to be 30 Hz (an order of magnitude lower than the plate's natural frequency) to effectively filter out any plate vibrations. The cutoff frequency was not set any lower to enable observation of the in-process forces over one revolution of the workpiece or wheel (16 Hz and 5 Hz respectively).

The system was used as is because it was deemed adequate for the current research; however its dynamics could still be further improved. There are two suggestions to improve the system. First, add a live center to support the workpiece and, second, to better support the mounting plate. The live center will stiffen the workpiece as

well as be very beneficial to traverse grinding, and a stiffer mounting plate would further increase the 360 Hz plate frequency. The mounting plate could be stiffened by making it thicker or by adding supports.

4.4   Conclusion of Rotary Axis Chapter

The rotary axis successfully meets all design requirements. It has accurate speed control over the 0 - 500 rpm range and under loading. The motor provides enough torque for aggressive grinding operations at any speed in this range. The grinding forces can be accurately measured in all axes. The natural frequency of the system is high enough to not experience excessive vibration under grinding load. The waterproofing of the rotary axis is successful at protecting the motor, encoder, and timing belt from coolant and grinding debris. Finally, the system is safe to operate and is performing reliably.

Chapter 5

Experimental Apparatus

This chapter will cover the experimental design of the grinding tests. It will cover what equipment and samples were used in conjunction with the rotary axis and how measurements of the relevant parameters were taken. There are also sections that discuss the grooving method used on the wheel, and that address repeatability and wheel wear.

5.1 Blohm Planomat

The grinding machine used in these experiments is a Blohm Planomat 408 grinder, shown in Figure 5.1. The machine's technical specifications can be found in Table 5.1. It is controlled using a Fanuc 18i-m CNC controller.

Figure 5.1: Blohm Planomat 408 used for all grinding experiments

Table 5.1: Technical specifications for the Blohm Planomat 408

Specification	Value	
	Metric	**Imperial**
X-Stroke	900 mm	35 in
Y-Stroke	550 mm	22 in
Z-Stroke	360 mm	14 in
X-Speed	30-30,000 mm/min	1-1180 in/min
Y-Speed	4-3750 mm/min	0.16-148 in/min
Z-Speed	4-4000 mm/min	0.16-157 in/min
Wheel Speed	1450 rpm	
Output	7.5 kW	10.1 hp

5.1.1 Coolant

Thanks to the rotary axis' waterproofing, experiments could use a coolant spray to better resemble industrial grinding. The coolant system in use on the grinding machine is a custom setup built to provide high flow and a coherent jet stream. Using an inline flowmeter a coolant flow of 10 gallons per minute was used for all experiments, while the nozzle diameter was 8mm.

The coolant used throughout the experiments was CIMTEX 310 with InSol. A refractometer was used to maintain a consistent concentration of 5.1%. This concentraion was checked before every experiment.

5.2 G-code

The Grinding Lab's Blohm Planomat was designed for flat grinding and the pre-programmed routines (also known as G-code macros) reflect this. To use the machine for cylindrical grinding new macros had to be coded into the machines Fanuc 18i-m CNC controller. This section describes the two macros built (one for plunge grinding and one for traverse grinding) and their respective capabilities.

The plunge grinding operation, as shown in Figure 2.5, is fairly simple. The macro tells the grinding wheel to plunge at a desired location on the workpiece, at

a commanded infeed rate v_f to a specified depth. The speed and direction of the grinding wheel can be specified here as well. The program also allows for the wheel to dwell, or wait, after completing the plunge. This dwell time serves as a spark out for the operation. For the traverse grinding operation, after the initial plunge the wheel travels along the workpiece axis to a desired end position. This speed v_r is controlled through the macro and can be set as high as 157 in/min (3.99 m/min), which is the speed limit of the machine. Table 5.2 gives the variables that can be adjusted in each macro along with their description. Appendix C gives the macro codes in their entirety.

Table 5.2: The variables used in G-code macros for plunge and traverse cylindrical grinding

Variable	Plunge Macro	Traverse Macro
S	Peripheral Wheel Speed, v_s	Peripheral Wheel Speed, v_s
H	Wheel Rotation, CW or CCW	Wheel Rotation, CW or CCW
R	Safety Height in Y axis	Safety Height in Y axis
Y	Depth of Plunge, d	Depth of Plunge, d
U	Infeed Rate, v_f	Infeed Rate, v_f
T	Dwell Time, T_d	Dwell Time, T_d
Z	Z Position of Back Wheel Face	Start Position of Back Wheel Face
K	-	End Position of Back Wheel Face
W	-	Traverse feed rate, v_r

5.3 Samples

The samples used in our experiments were $1''$ (25.4 mm) precision ground 1045 steel bar cut to $4\frac{1}{2}''$ lengths as shown in Figure 5.2. There were two main benefits to using these samples. First, the carbon content of 1045 steel makes it well suited to grinding. Second, while any workpiece that is mounted in a collet needs a light grind (or initial clean up) to become concentric with collet spindle. These precision ground workpieces only require 0.002" (50.8 μm) of grinding to achieve concentricity, compared to 0.010-0.020" (254-508 μm) for a cold rolled sample. It was found that the intial roundness of a fresh sample inserted into the Collet Master was about 0.001" (25.4 μm). Also, to ensure consistency all workpieces were marked to have $3''$ (76.2

mm) of overhang measured from the end of the collet. This length was chosen to allow traverse experiments to be performed in case future comparisons between plunge and traverse grinding will be made. For this thesis, however, traverse grinding is outside the scope of work.
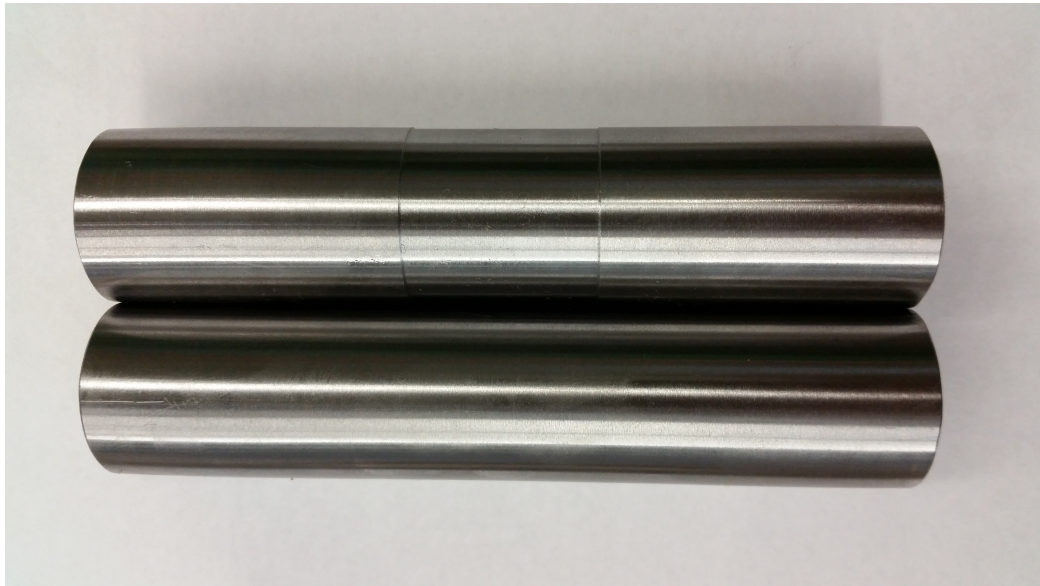
Figure 5.2: The precision ground 1045 samples used in the grinding experiments. Top is after a plunge operation was performed.

5.4 Instrumentation

To capture the experimental force and power data the instrumentation shown in Figure 5.3 was used. Force data capture starts at a Kistler type 9257B three-component dynamometer. The signal from the dynamometer was then sent to a Kistler model 5019A charge amplifier. Finally the signal was captured using a National Instruments BNC-2120 connector block attached to an in-computer PCI-MIO-16XE-10 data acquisition card and processed with LabView. For the spindle power a PH-3A power transducer from Load Controls Inc. converts the power directly into a measureable voltage and sends it to the same connector block as the charge amplifier.
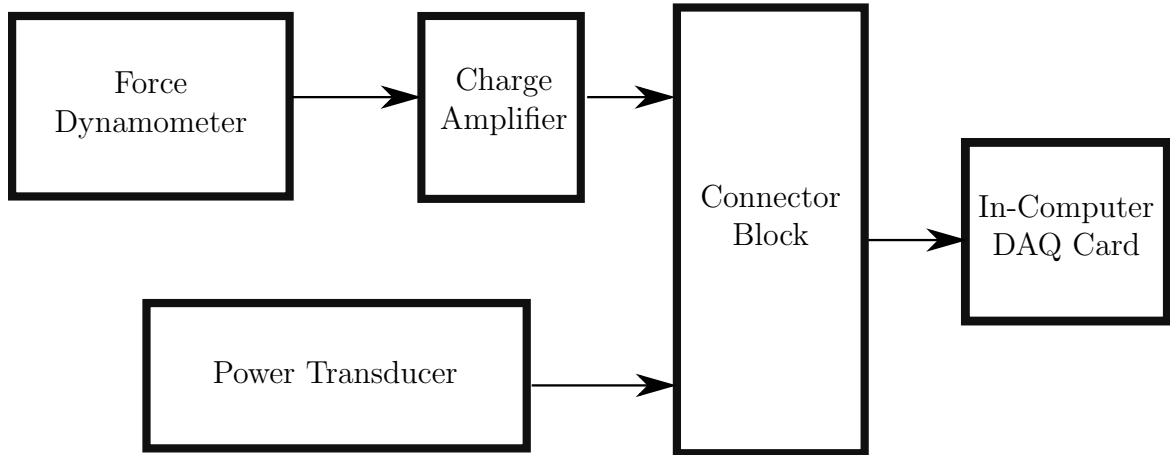
Figure 5.3: Layout of instrumentation used to capture forces and spindle power

5.4.1 Roughness Measurements

The two instruments were used to measure the surface roughness of the samples are a Mahr Federal Pocket Surf, and a Nanovea profilometer with a $130\,\mu$m pen, both shown in Figure 5.4. The Pocket Surf was the main instrument used because it can quickly take multiple readings from a workpiece still installed in the rotary axis. It can read surface roughness with a $\pm 0.01\,\mu$m accuracy. Each sample was scanned at five random locations on the ground workpiece.

The Nanovea profilometer was used for special cases because it was more time consuming to use. It was used to scan larger lengths, to confirm the pocket surf readings, and it can give the profiles for workpiece textures.
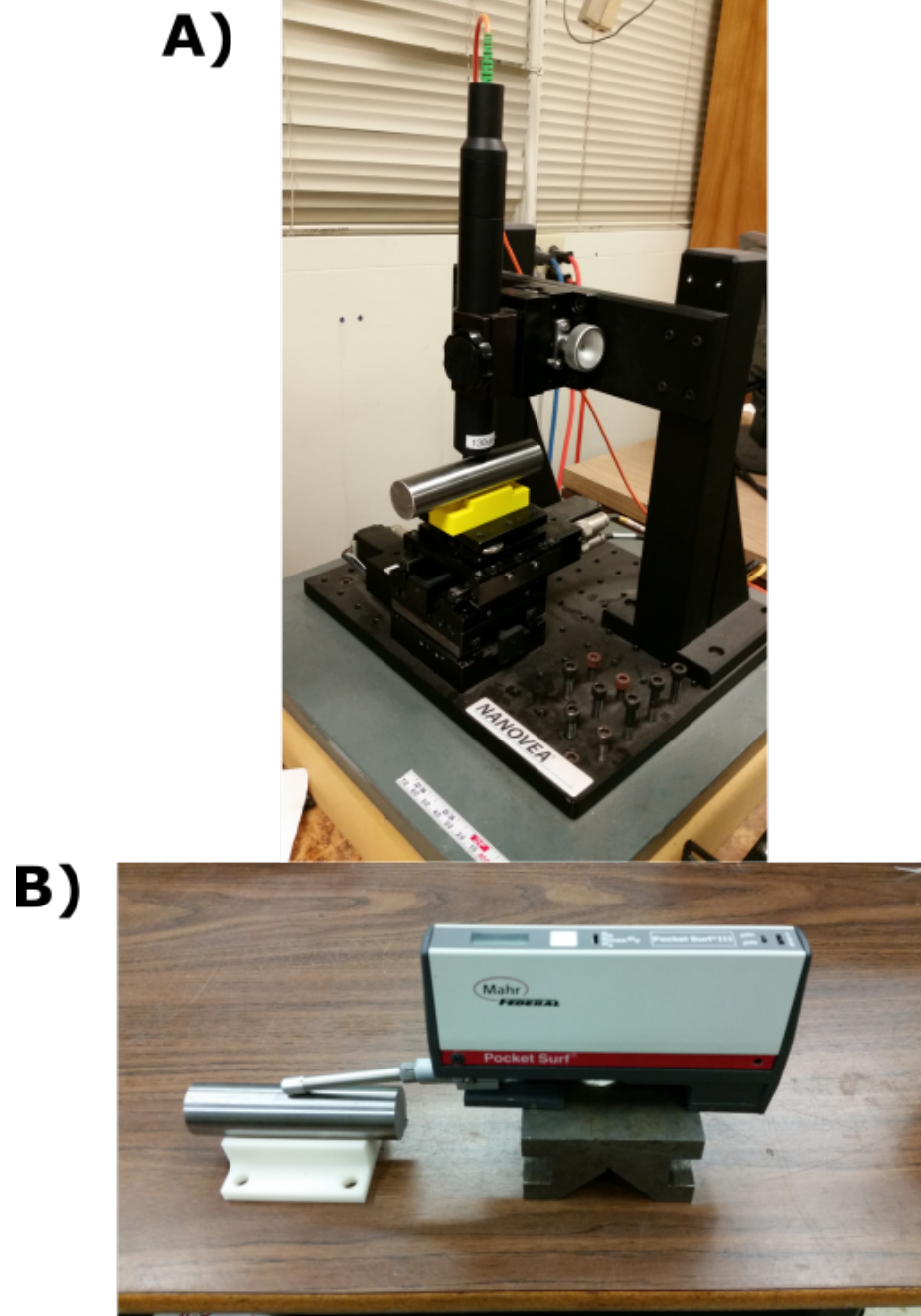
Figure 5.4: The instruments used for surface roughness measurements. A) the Pocket Surf, and B) the Nanovea profilometer.

5.4.2 Roundness Measurements

To measure the roundness of finished parts a Mitutoyo dial indicator was mounted to the grinding machine as shown in Figure 5.5. The dial indicator can accurately

measure to ± 0.0001" ($\pm 2.54 \mu$m). This level of precision allows confirmation that the parts are within acceptable roundness values.

Figure 5.5: The roundness measurement apparatus with Mitutoyo dial indicator

5.5 Grinding Parameters

No two grinding experiments can be exactly the same because of the variability in factors such as coolant flow and wheel condition; however, for the experiments to reflect realistic and relevant grinding conditions a study of grinding parameters used

in industry and other similar research was performed, [59], [54], [60]. This data influenced the design of the rotary axis and was used to select the parameters that were common to all studies in Chapter 6, and is shown in Table 5.3.

Table 5.3: The grinding parameters used in the next chapter

Grinding Parameters	Imperial		Metric	
Wheel	WRA60-J5-W Radiac			
Wheel Material	Aluminum oxide			
Wheel Grit	60			
Wheel Width	1.05	in	26.7	mm
Wheel Diameter	15.6	in	396.2	mm
Wheel Speed	20.3	ft/min	20.32	m/s
Workpiece Material	Precision ground AISI 1045			
Workpiece Diameter	1	in	25.4	mm
Workpiece Speed	300	rpm		
Sparkout Time	10	s		
Lubricant Used	CIMTECH 310 with InSol			
Lubricant Concentration	5.1%			
Lubricant Flowrate	10	gpm	37.9	lpm

5.6 Dressing Parameters

The initial dressing conditions of the grinding wheel are known to have a significant effect on the grinding process. The dressing parameters used throughout this thesis are presented in Table 5.4. The single point diamond tool width b_g was measured using a Celestron Digital Microscope Pro and processed using Celestron's software. Figure 5.6 shows the resulting image of the diamond tip with $b_g = 0.0310$" (788 μm) at the dressing infeed of 0.0004" (10.2 μm). This diamond tool was also used for wheel grooving.

Table 5.4: The wheel dressing parameters used throughout the thesis

Dressing Parameters	Value	Units
Radial Feed Rate v_r	103	mm/min
Wheel Speed ω_s	970	rpm
Depth of Cut d	10.2	μm
Tool Width b_g	788	μm
Overlap Ratio	7.5	-
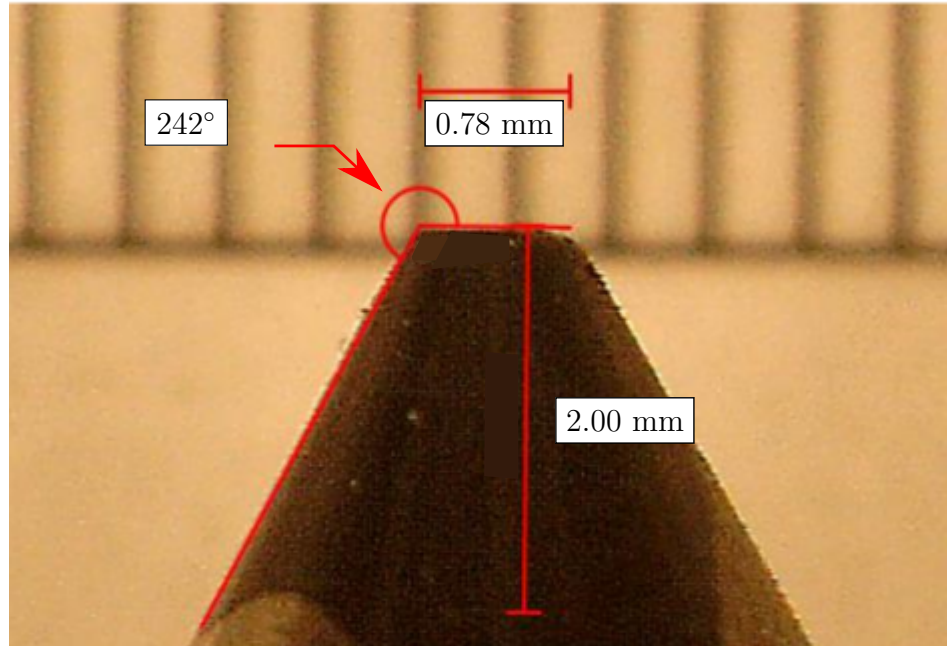
Figure 5.6: The geometry of the diamond tip used for wheel dressing and grooving

5.7 Groove Parameters

The wheel groove pattern used throughout this thesis was a 50% groove factor shallow cicumferential groove, i.e. 50% of the wheel surface remained after grooving. This groove is considered shallow because it is only 0.004" (101.6 μm) deep which allowed for it to be applied in a single pass by a single point diamond tool. The grooving parameters were calculated using Equation 5.1 where L is the groove lead, b_g is the groove width, and η is the groove factor. Figure 5.6 shows how these parameters relate to the grinding wheel.

$$L = \frac{b_g}{1 - \eta} \qquad (5.1)$$
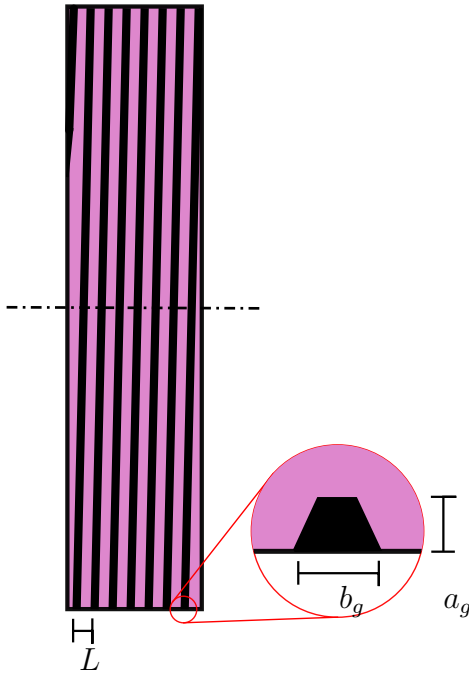
Figure 5.7: The important parameters used when discussing circumferential grooves

The 50% groove factor was used because it was shown to have the most significant effect on the grinding process in surface and creep-feed grinding operations by Mohamed *et al.* [48]. Figure 5.6 was used to find the groove width b_g of 0.0348" (884 μm) and an infeed of 0.004" (102 μm). Table 5.5 summarizes the parameters that describe the groove pattern.

Table 5.5: The groove parameters that define the wheel used in the experiments

Groove Parameter	Value	Units
Groove factor η	50%	-
Groove width b_g	884	μm
Groove depth a_g	102	μm
Lead L_g	1768	μm/rev

5.8 Conclusion of Experimental Apparatus Chapter

This chapter presented the instrumentation and equipment that will be used in conjunction with the rotary axis to explore the grinding process. This information,

along with the grinding, dressing, and groove pattern parameters, are used throughout the studies in the next chapter. Techniques and parameters unique to each study are presented in the section pertaining to each study.

Chapter 6

Plunge Grinding Experiments

This chapter covers the four cylindrical plunge grinding studies performed. They are presented in chronological order as the results of one experiment were used to guide subsequent experiments. Each of these studies holds value in and of themselves, and together they highlight the versatility and effectiveness of the rotary axis as a research apparatus.

6.1 Effect of Workpiece Stiffness in Cylindrical Plunge Grinding

The first study performed explored the effect of workpiece stiffness in plunge grinding. Since the workpiece is held in a cantilever fashion the workpiece stiffness varies significantly with the grinding location. This grinding configuration translates into large changes in workpiece deflection, causing changes to other grinding parameters such as forces. Plunge grinding experiments were performed at two different grinding locations and the resulting effects on forces, spindle power, roundness, and surface roughness were investigated.

6.1.1 Setup for Workpiece Stiffness Study

Grinding experiments were performed using the wheel describe in Table 5.3 without any grooving on 1" AISI 4140 steel samples. The wheel was initially dressed according to the parameters in Table 5.4 and the specific plunge parameters for this study are given in Table 6.1. The grinding forces, spindle power, workpiece surface roughness, and workpiece roundness were measured.

Table 6.1: Grinding parameters used in the plunge location comparison

Grinding Parameters	Value	Units
Workpiece Speed	300	rpm
Wheel Diameter	402	mm
Infeed Rate	2.54	μm/rev
Depth of Cut	127	μm
Dwell Time	15	s

Figure 6.1 shows the two grinding locations used in the experiment. Distances were measured from the end of the collet to the back face of the wheel. Location 1, at 12.7 mm, was chosen because it was as close to the collet as possible without touching the waterproofing enclosure. Location 2 was at 38.1 mm.
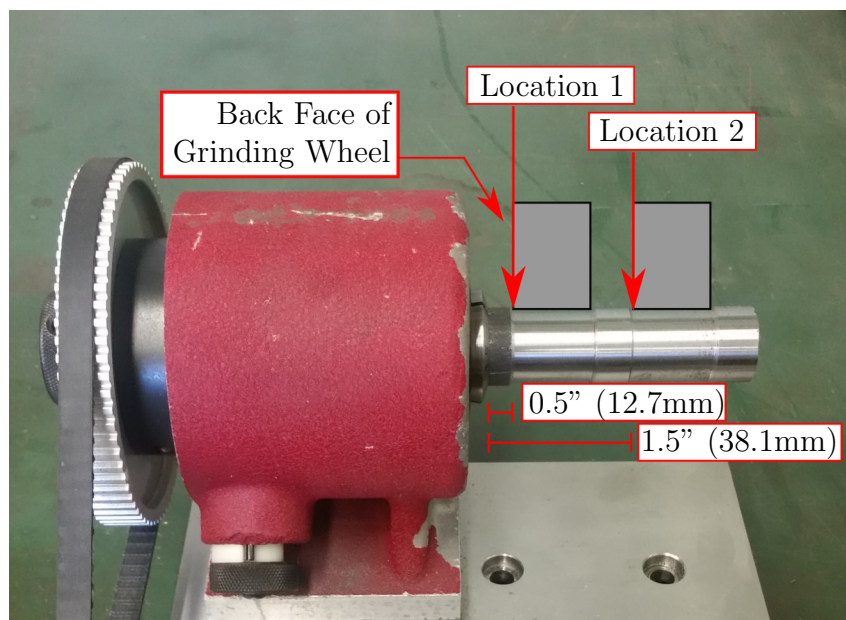
Figure 6.1: The two locations used in the grinding experiment, at 12.7mm and 38.1mm

6.1.2 Results of Workpiece Stiffness Study

The results of the study are now presented and analyzed. There is particular attention paid to how the force data was interpreted, as well as the importance of time constants and how they were calculated. Where relevant, this section also highlights what lessons were carried onto future studies.

Forces Results

The normal force data collected from location 1 (12.7 mm) plunge grinding experiment is presented in Figure 6.2. The graph shows the raw data in blue and the filtered data in black for the complete plunge grinding operation. As discussed in Section 4.3.3, this raw data was too noisy to easily interpret without a low pass filter, therefore, the filtered data is used for the analysis. This low pass filter is applied to all force data in all subsequent experiments.
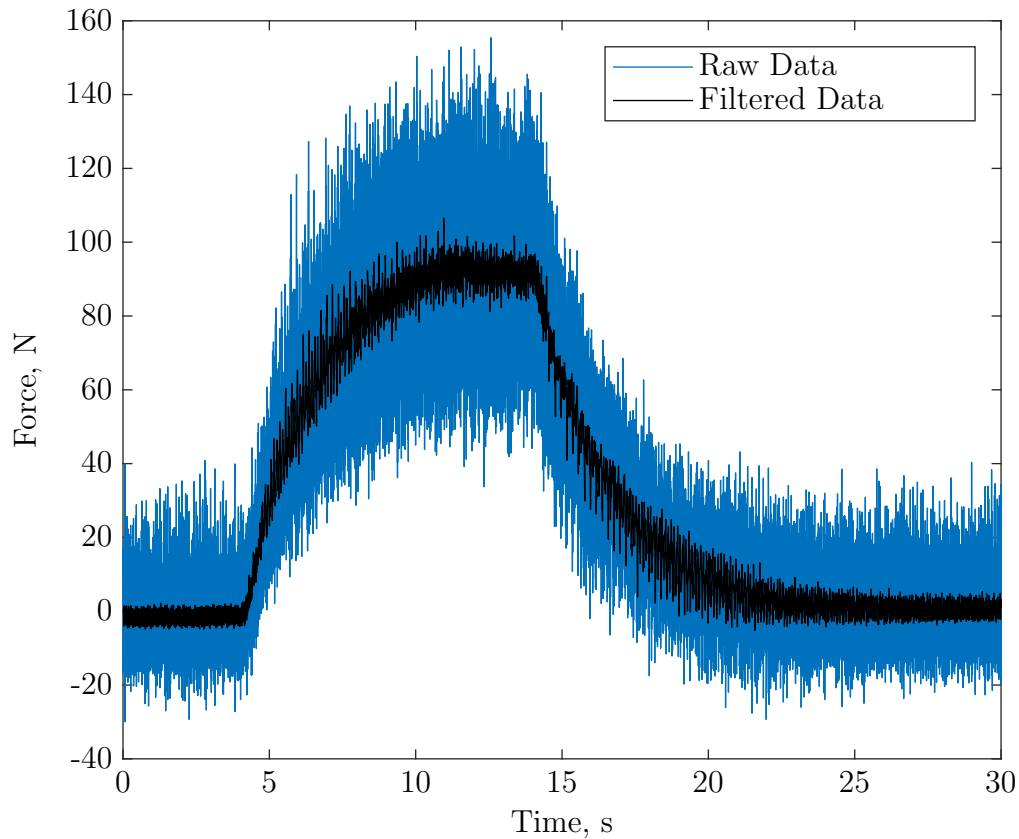
Figure 6.2: The raw and filtered normal force data taken from grinding at location 1 (12.7 mm).

Figure 6.3 shows the filtered force data for all axes at location 1 (12.7 mm). The normal and tangential forces show a similar curve shape, while the radial force remains near 0 N. Figure 6.4 presents the filtered force data for all axes at location 2 (38.1 mm) as a comparison to the data from location 1 (12.7 mm). Again the radial

force remains near 0 N and the normal and tangential curves have similar shapes to eachother; however, the shape of the normal and tangential curves varies significantly between the two locations.
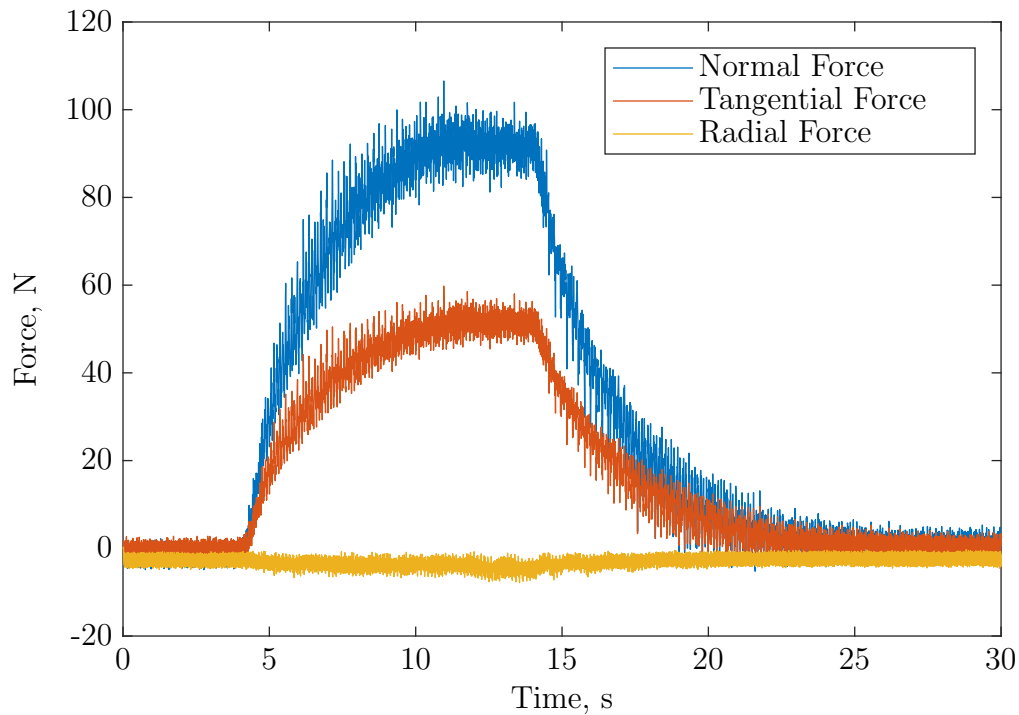
Figure 6.3: Graph of all the grinding forces at location 1 (12.7 mm

The difference in curve shape is further highlighted in Figure 6.5. This figure overlays the filtered normal force curves for the two grinding locations. Features of note are the lower peak force for location 2 (38.1 mm), the exponential shape of both curves, and the fact that the curve for location 2 (38.1 mm) does not reach 0 N by the end of the grinding operation. The analysis of these features and how to extract usable data from the force curves is the topic of the next section.
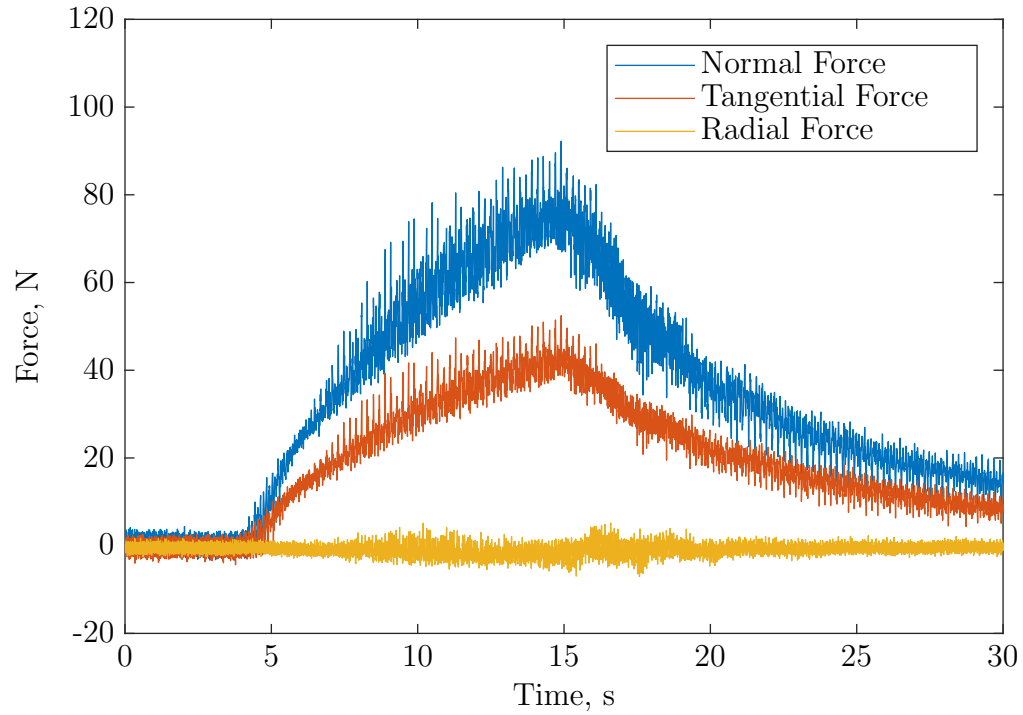
Figure 6.4: Graph of all the grinding forces at location 2 (38.1 mm)
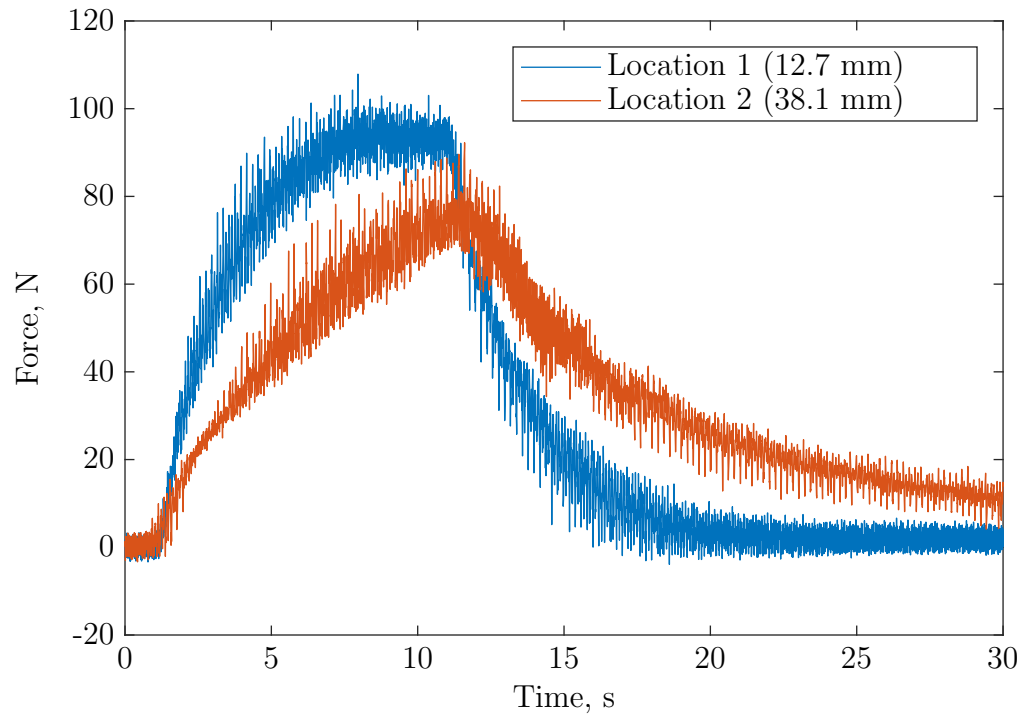
Figure 6.5: Comparison of normal force curves for plunge grinding at locations 1 and 2.

Force Analysis and the Continuous Infeed Model

The key to understanding the shape of the force curves was Malkin's continuous infeed model [4]. This model described the effects of workpiece deflection during plunge grinding operations and can be used to analyze the infeed of the wheel into the workpiece and the resulting forces.

Figure 6.6 shows the wheel infeed commanded by the grinding machine (blue) and the actual infeed into the workpiece (red) of a plunge grinding operation based on Malkin's model. There are three distinct phases to the curve: the spark in, the steady state, and the spark out. Spark in begins after the wheel contacts the workpiece. During spark in the workpiece is deflecting, causing the actual infeed to be less than the commanded infeed. Eventually the difference in the infeed rates will reach a steady state; the time it takes to get to that steady state is dependent on the system's stiffness. Together the spark in and steady state phases describe the infeed portion of the grinding operation while the spark out is the dwell portion.

During dwell the wheel no longer penetrates the workpiece but the elastic deflection of the workpiece causes cutting until it too reaches the commanded depth of cut. The rate of the spark out is also dependent on the system stiffness.
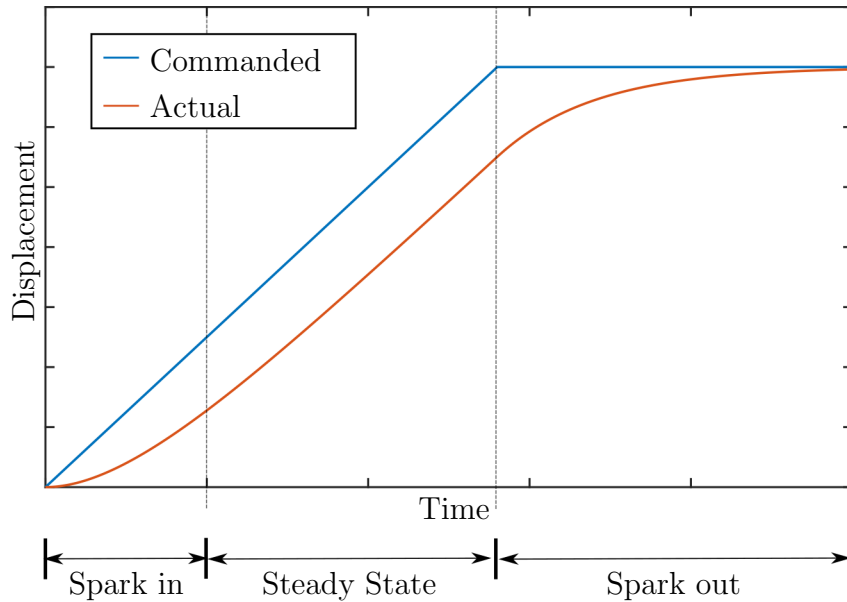
Figure 6.6: Malkin's continuous infeed model showing the commanded infeed vs. the actual infeed during plunge grinding

A paper by Ramos *et al.* [31] was used to convert the infeed model into a force model. Equation 6.1 relates the normal force F_n to the cutting stiffness k_c and the instantaneous infeed a. At steady state, the instantaneous infeed is equal to the commanded infeed.

$$F_n = k_c \cdot a \qquad (6.1)$$

Applying Equation 6.1 to the instantaneous infeed from Figure 6.6 produced Figure 6.7. Figure 6.7 gives the normal force vs. time curves for commanded (blue) and the actual (red) infeed. The three phases of plunge grinding apply to the normal force curve just like the infeed curve. After wheel contact, the actual force increases during spark in until it reaches a steady state value. This steady state value is equivalent to the cutting stiffness and the instantaneous commanded infeed, and is the maximum force of the grinding operation. During spark out (dwell) the actual force decreases to zero as the elastic deflection is cut away.
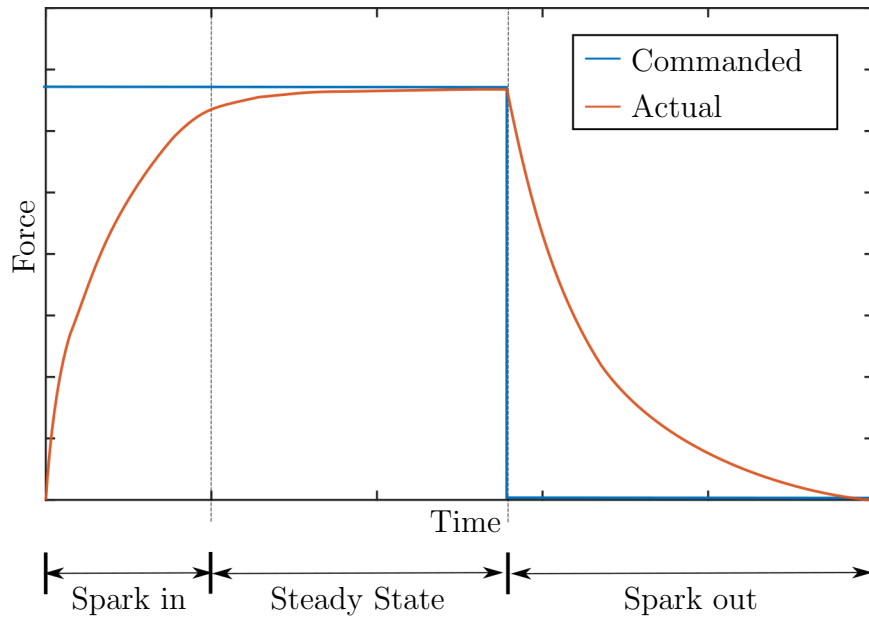
Figure 6.7: Example of the commanded vs. the actual cutting force during plunge grinding

The theoretical normal force curve could then be compared to the measured force curve. Figure 6.8 gives the filtered normal curves from the plunge grinding operation at location 1 (12.7 mm). The spark in, steady state, and spark out phases are highlighted, and the shape agrees with the continuous infeed model. Measuring the steady state value of 92 N for the normal force was then straightforward through inspection.

Figure 6.9 shows that the force curve from the grinding at location 2 (38.1 mm) also agreed with the continuous infeed model. However, in this case the operation did not reach a steady state by the time the dwell began. Furthermore, the spark out was not completed by the end of the grinding operation which means there was still some elastic deflection and, therefore, the commanded depth of cut was not achieved.
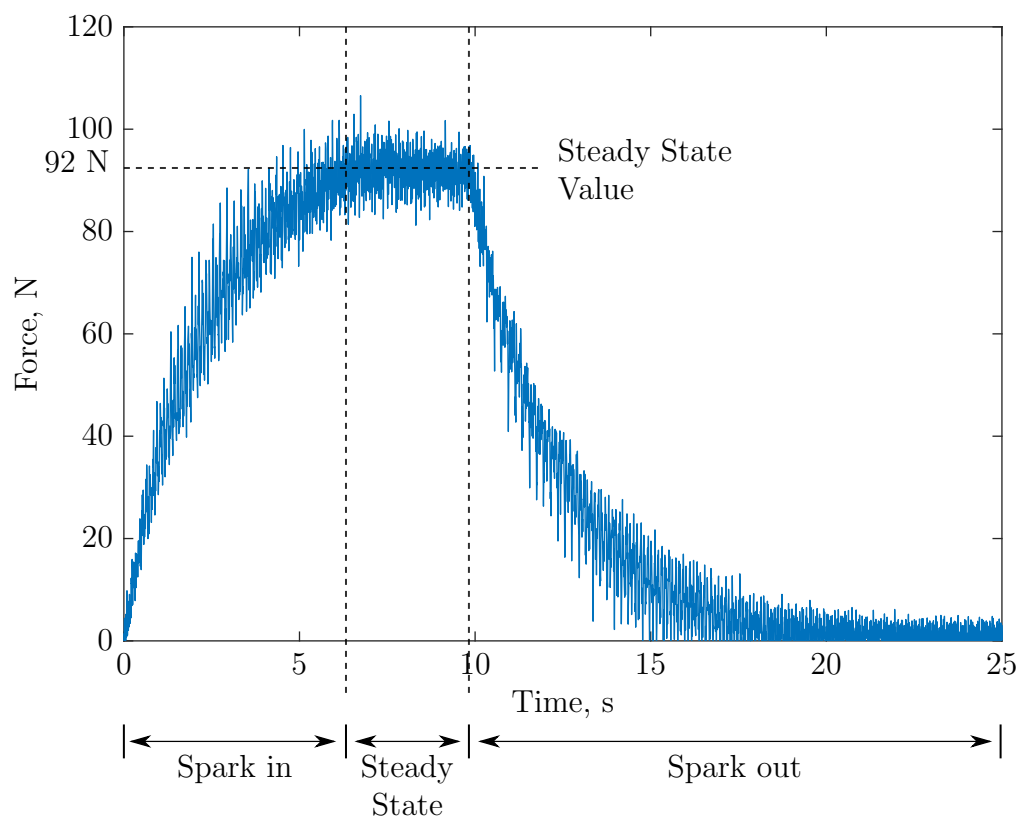
Figure 6.8: The measured normal force curve at grinding location 1 (12.7 mm) with the spark in, steady state, and spark out sections highlighted.
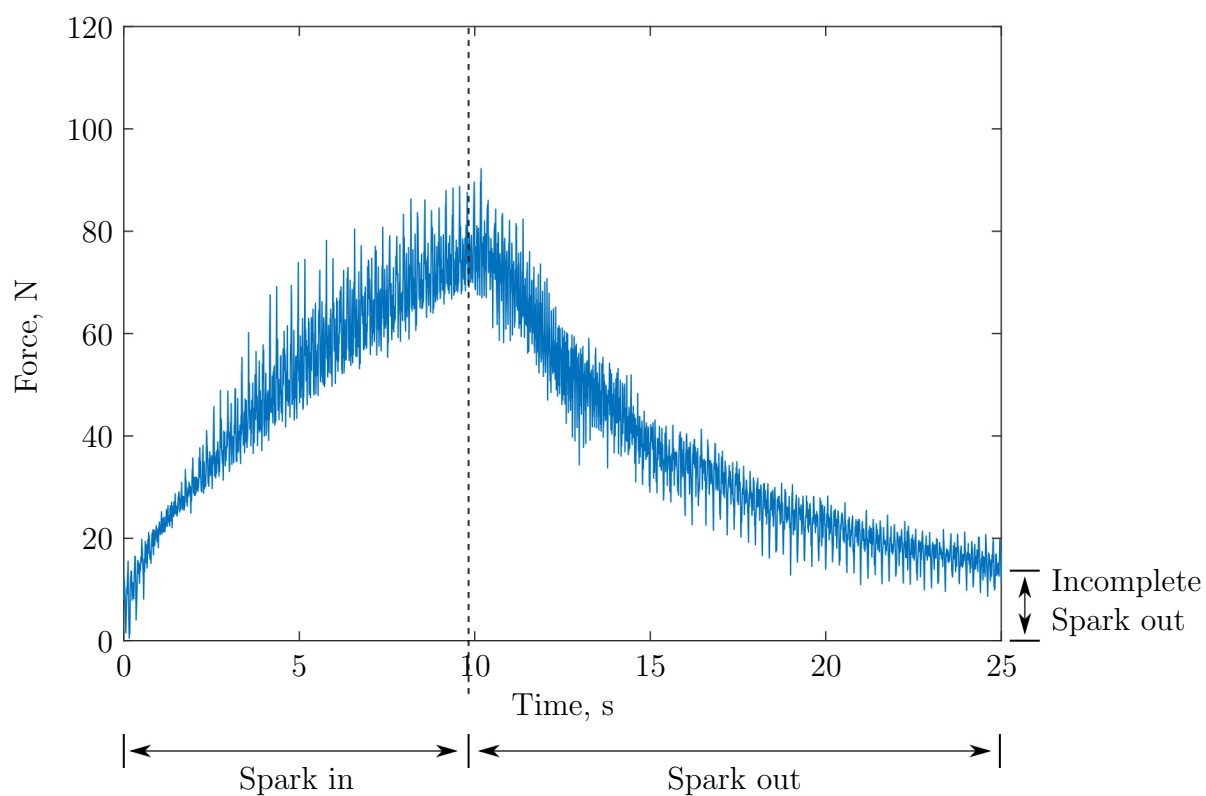
Figure 6.9: The measured normal force curve at grinding location 2 (38.1 mm) with the spark in and spark out phases highlighted.

Since grinding at location 2 (38.1 mm) did not reach a steady state it was difficult to compare the normal force values of the two grinding operations. However, according to Snoey *et al.* [62] cutting stiffness is dependent on the workpiece material, the grinding wheel composition, the wheel's dressing condition, and the speed ratio between the wheel and workpiece. Since these variables did not significantly change between the two grinding location tests, Equation 6.1 could then be used to calculate the cutting stiffness k_c for both operations from the steady state normal force F_n at location 1 (12.7 mm). k_c was found to be 36.2 N/μm, and since the commanded infeed was the same in both tests it is likely that the steady state normal force for location 2 (38.1 mm) would be 92 N as well.

For a fair comparison to be made in future studies, plunge grinding should be performed to a depth that allows the system to reach steady state. However, the methodology presented here for analyzing the force data is effective and gives a good understanding of the grinding process.

Time Constant Analysis

Malkin's continuous infeed model also found that the rate of spark in and spark out were exponential functions with the same time constant τ as shown in Equation 6.2 where k_e is the effective stiffness of the system. By measuring the time constant for the two grinding locations the effective stiffnesses of the two grinding locations could then be compared.

$$\tau = \frac{F_n}{k_e \cdot v_f} \tag{6.2}$$

The exponential decay of the spark out phase is described using Equation 6.3. The time constant could then be measured by applying Matlab's exponential fit function to the spark out of the normal forces. Figure 6.10 shows the spark out phase for location 1 (12.7 mm) (grey) and the exponential fit (black). It can be seen that the fit follows the spark out closely with an r^2 value of 0.938 and it was, therefore, used

to calculate the time constant of 2.9 s.

$$F(t) = F(0) \cdot e^{-\frac{t}{\tau}} \tag{6.3}$$
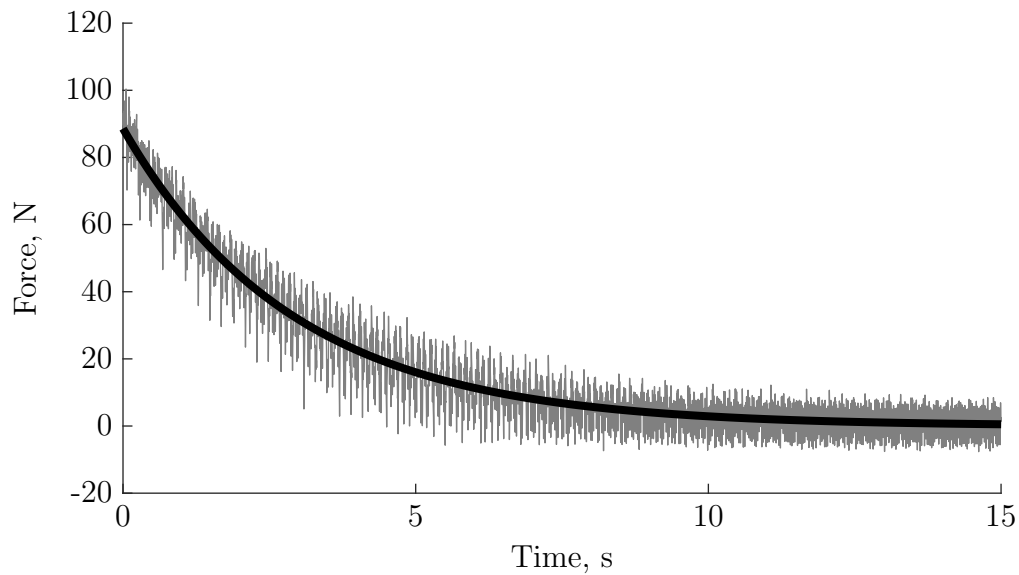
Figure 6.10: The exponential curve fit from the spark out at location 1, the time constant is 2.9s.

Figure 6.11 shows the spark out data for the normal force (grey) and the applied exponential fit (black) for location 2. Even though the grinding operation at location 2 (38.1 mm) did not reach a steady state, the exponential curve fit still accurately followed the spark out with an r^2 value of 0.947. Here the time constant value is 7.2 s.
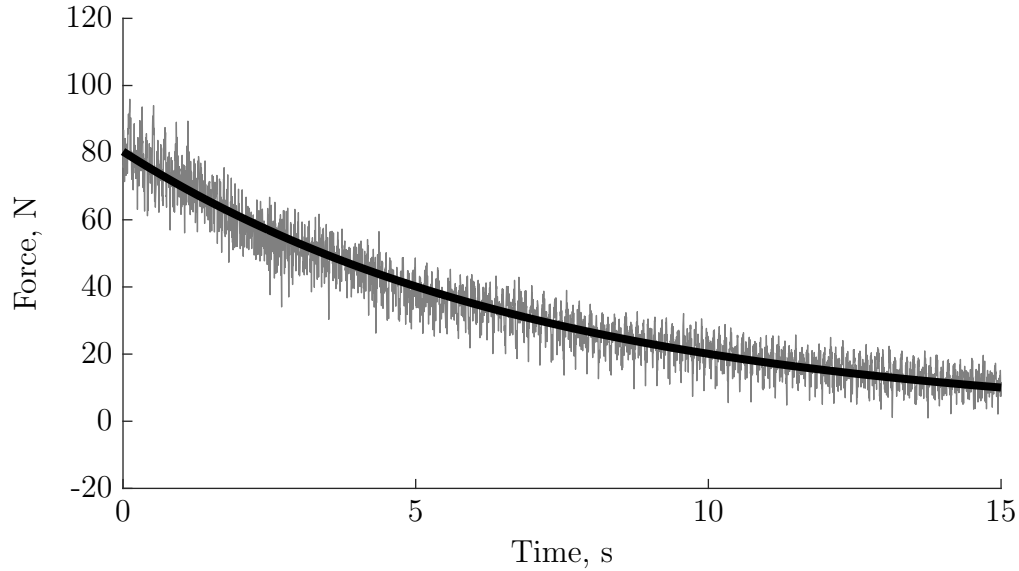
Figure 6.11: The exponential curve fit from the spark out at location 2, the time constant is 7.2s.

These measured time constants were then converted into stiffness using Equation 6.2. Table 6.2 gives the results of the calculation. Now it could be concluded that the difference in grinding location caused a 2.5 times decrease in the effective stiffness.

Table 6.2: The effective stiffnesses and time constants for the workpiece stiffness study.

Test	Time Constant τ	Effective Stiffness k_e	Cutting Stiffness k_c
Location 1	2.9 s	2.50 N/μm	36.2 N/μm
Location 2	7.2 s	1.01 N/μm	36.2 N/μm

The effective stiffness k_e is not the same as the cutting stiffness k_c. k_e can be thought of as three springs in series (as shown in Figure 6.12) that represent the stiffness of the whole grinding system. k_w is the stiffness of the rotary axis, k_s is the stiffness of the grinding machine, and k_a is the contact stiffness [4]. The change in grinding location will affect k_w and from the significant difference in k_e seen between the two grinding locations, k_w and k_e are heavily dependent on the stiffness of the cantilevered workpiece.
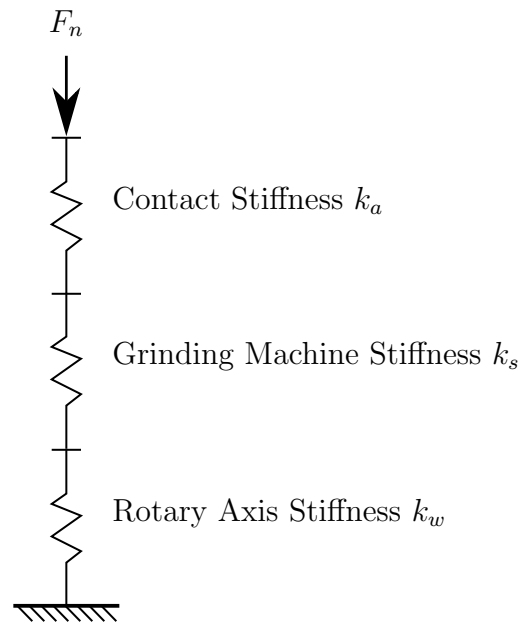
Figure 6.12: The stiffness of the grinding system in the normal axis.

Stiff grinding systems and the resulting lower time constants are important in manufacturing because they speed up production. For example, the grinding operation at location 1 (12.7 mm) takes 13.4 s of spark out to be within 1% of it's desired depth of cut. The grinding operation at location 2 (38.1 mm), however, takes 33.2 s to reach the same level of spark out. This extended spark out requirement explains the incomplete spark out at location 2 (38.1 mm), and further proves the benefits of stiff grinding systems.

Spindle Power, Surface Roughness, and Roundness Results

The same raw data filtering and curve fitting analysis that was used in the force analysis was used to analyze the spindle power. The raw data was filtered using the same low pass filter and the power value was taken at the steady state. Figure 6.13 shows the power curves for both locations. The general shape of the power curves is the same as the force curves. A steady state spindle power of 1306 kW can be measured for location 1 but, as in the force analysis, location 2 does not reach steady state.
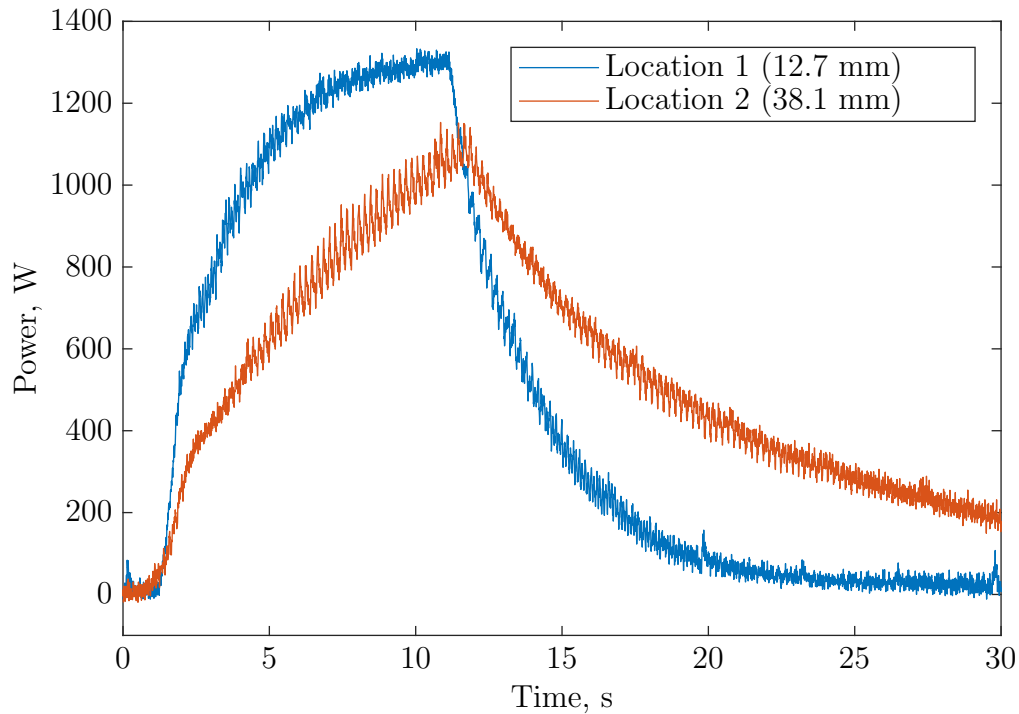
Figure 6.13: Comparison of spindle power curves for plunge grinding at locations 1 and 2.

The roundness and surface roughness values were measured using the techniques describe in Sections 5.4.1 and 5.4.2. Table 6.3 gives the mean values from the measurements for the two grinding locations. It is apparent that grinding at location 2 gave both increased roundness error values and surface roughness. The likely reason for the higher roughness and roundness values at location 2 (38.1 mm) is the incomplete spark out. These results provide more proof that grinding at the stiffer location 1 is preferable.

Table 6.3: Roundness and surface roughness values from the plunge location comparison

Test	Roundness, μm	Surface Roughness, μm
Location 1 (12.7 mm)	72.0	0.37
Location 2 (38.1 mm)	156.6	0.46

6.1.3 Conclusion of Workpiece Stiffness Study

The most important conclusion drawn from this study is that plunge grinding operations should be performed as close to the collet as possible to improve the system's stiffness. The study proved that higher stiffness leads to improved tolerance in the finished workpiece, lower time constants, and a faster production rate. The other conclusions from this study are that the rotary axis mounted on the force sensor is effective at measuring in-process forces and can be used to measure time constants. The process of analyzing the raw force and spindle power was also presented, and found to work well. These findings will be used to design future studies.

6.2 Comparison of Wheel Wear for Grooved and Non-grooved Grinding Wheels

To better understand wheel wear and it's potential effects on the experimental results, a study was performed to compare wheel wear for grooved and non-grooved grinding wheels. Through repeated aggressive grinding with no dressing operations in between, the ability of the wheel to withstand wear can be explored. Surface roughness measurements were taken from the finished workpieces, which are used as wear indicators, as suggested by Guo *et al.* [63]. The findings were then analyzed and used to improve subsequent research.

6.2.1 Setup of Wheel Wear Study

The grinding parameters for the study are given in Table 6.4. There were five tests performed with a range of infeeds from light to aggressive, chosen to reflect the range of infeeds in the next study (Section 6.3).

These five tests were performed with both grooved and non-grooved wheels. The grinding wheel is the same as in Table 5.3, the groove parameters are those described in Table 5.5, and the initial dressing parameters are given in Table 5.4. Before each test a light clean up grind with an infeed rate of 1.0 μm/rev and a depth of cut of 50.8 μm was performed to provide a consistent starting condition. The surface roughness

Table 6.4: The grinding parameters used in the grooved wear study

Grinding Parameters	Value	Units
Workpiece Speed	300	rpm
Wheel Speed	969	rpm
Wheel Diameter	399	mm
Infeed Rate	1.0 - 5.1	μm/rev
Depth of Cut	254	μm
Dwell	15	s

after this light clean up grind was then used for this comparison.

6.2.2   Roughness Measurements from Wheel Wear Study

Figure 6.14 shows the surface roughness after the workpiece cleanup for grooved and non-grooved wheels for each grinding operation. These measurements were captured with the Pocket Surf as described in Section 5.4.1. The variability in the error bar size reflects how variable the grinding process is, even over a the surface of one workpiece. The visible trend of this data was that while the roughness of the non-grooved wheel increased slowly as the trial progresses, the roughness of the grooved wheel gets significantly worse which indicated significant wheel wear.
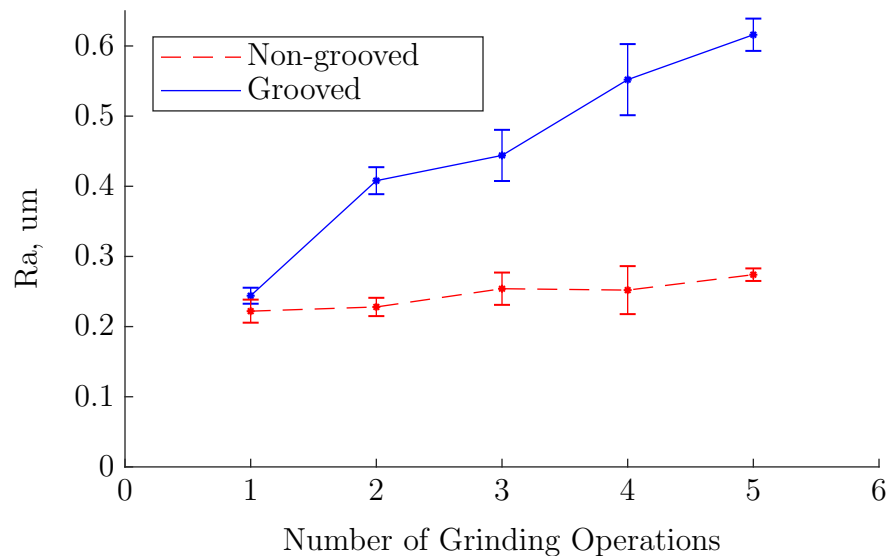
Figure 6.14: Surface roughness comparison after workpiece clean up for first trial

According to Shaw, the three main mechanisms of wheel wear are [9]:

1. The fracture of the bonds holding the abrasive grain in the grinding wheel.

2. The fracture of the abrasive grain which leaves a new sharp grain surface.

3. The wear of the abrasive which dulls the cutting edge.

The two fracture wear mechanisms result in an irregular workpiece surface and have a detrimental effect on surface roughness; therefore, the wear observed in Figure 6.14 is likely fracture wear. Since fracture wear occurs when the grinding forces exceed the bond or abrasive grain strength [11], the act of grooving a grinding wheel has likely weakened the abrasive grains or the bonds that hold the grains together. This conclusion about the weakening of the grinding wheel from grooving is also suggested in a paper by Uhlmann and Hochschild [49].

6.2.3 Modification to Depth of Cut

Three methods were identified to reduce wheel wear: using a grinding wheel with harder bonding material, changing the wheel's groove pattern, and reducing the material removed. A harder grinding wheel would be less susceptible to bond fracture [11], but that would require a repetition of the previous study (Section 6.1). A different groove pattern could have reduced wear compared to the 50% circumferentially grooved wheel, but that would require a significant number of experiments to find the optimal groove pattern, which was beyond the scope of this study. Therefore, a reduction of material removal was deemed the most logical method of addressing wheel wear.

Wheel wear increases with material removed [4] [11] [9]; therefore, a straightforward way to reduce wheel wear is to reduce the total material removed between dressing operations. To reduce the influence of grinding wheel wear on subsequent experiments and to avoid dressing between experiments the total material removed was reduced through the following method.

Figure 6.15 shows a sample normal force curve with an infeed rate of 2.03 μm/rev and depth of cut of 254 μm. Steady state grinding was achieved after 6.5 s, or a depth of cut of 66 μm, but grinding continued until the commanded depth of cut of 254 μm was achieved. If this grinding operation was stopped at a depth of cut of 71 μm, the grinding operation would still have reached steady state but the removed material would be significantly reduced.
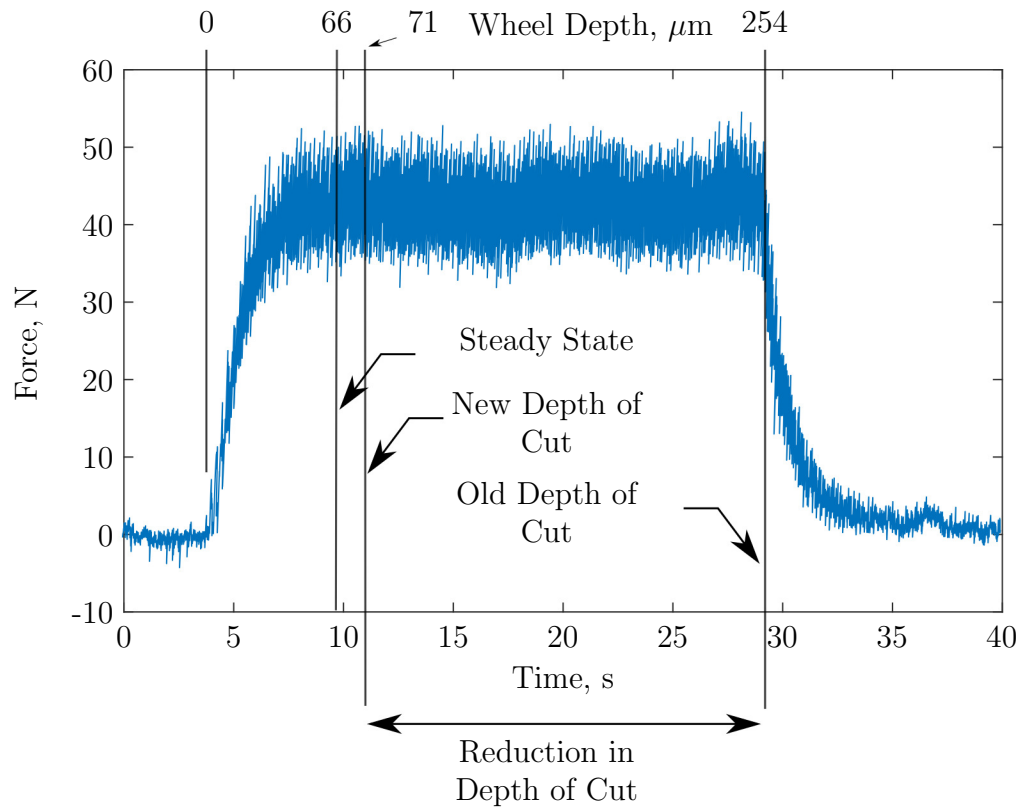
Figure 6.15: The normal force curve from a plunge grinding experiment. The infeed rate is 2.03 μm/rev, and the depth of cut is 254 μm. Lines are depicted where: the experiment reached steady state, the new depth of cut was chosen, the commanded depth of cut was, and the relative reduction in depth of cut.

By examining the force curves for each experiment, the depth of cut of each trial was reduced from 254 μm for each operation to the depths of cut shown in Table 6.5. These new depths of cut represents a 52% decrease in material removal.

Looking ahead to the results of this reduction, Figure 6.16 gives the surface roughness after the workpiece cleanup for the following two trials. Again, the roughness

Table 6.5: The new depths of cut chosen for second and third trials

v_f μm/rev	New Depth of Cut μm
1.02	36
2.03	71
3.05	107
4.06	142
5.08	178

is given for both grooved and non-grooved wheels as a function of grinding operations. The figure shows that while the roughness is slightly worse for grooved wheels there is little if any progressive wear through the trial. These results were used to conclude that the modified depth of cut values significantly reduced wheel wear.
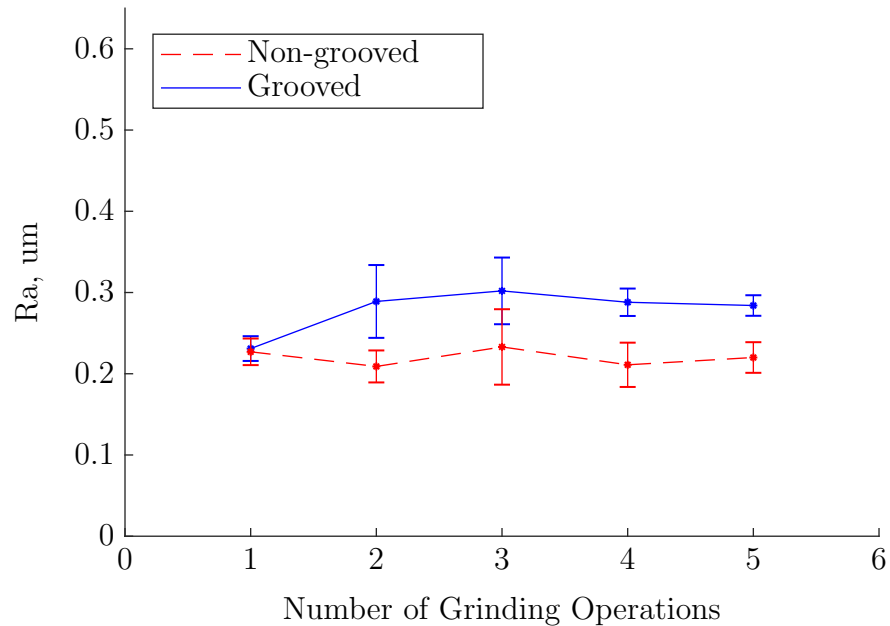
Figure 6.16: Surface roughness comparison after workpiece clean up for second and third trials

6.2.4 Conclusion to Wheel Wear Study

These wear studies prove a few important facts. First, the groove pattern used throughout these experiments is more susceptible to wear than a non-grooved wheel. Second, minimizing the material removed between dressing is an effective way to

prevent wear, and observing where an operation reaches steady state through force analysis is a good way to optimize this. Finally, wheel wear can have an important impact on the surface roughness of finished workpieces and therefore needs to be addressed in any experiment with significant material removal.

6.3 Comparison of the Effect of Infeed for Grooved and Non-grooved Wheels

This study is a comparison on the effects of infeed on the grinding process for grooved and non-grooved wheels. With 30 samples, it is the most extensive study performed with the rotary axis. These samples each have their in-process forces and spindle power measured, as well as the post-process roundness and surface finish. The results of these trials are used to throughly examine the relative performance of the circumferential groove pattern. The performance of this groove pattern in a cylindrical plunge grinding operation has never been studied before, which makes this study unique.

6.3.1 Setup of Infeed Comparison

This study involves performing plunge grinding at five different feed rates with both grooved and non-grooved wheels and comparing the results. Each experiment was done three times to show repeatability. The grinding parameters are the same as those given in Table 5.3, the groove pattern is described in Table 5.5, and the dressing parameters are shown in Table 5.4. The five infeed rates v_f and their respective depths of cut d are given in Table 6.6. As discussed in the wear study (Section 6.2), the depth of cut was changed after the first trial to address wheel wear. The effects of this change on the results will be discussed where relevant. Finally, all workpieces were prepared with a light grind at an infeed rate of 1.27 μm/rev at a lower workpiece angular velocity of 200 rpm to a depth of 50.8 μm to provide a consistent starting condition for all tests.

Table 6.6: The infeed rates and respective depths of cut used for the infeed comparison study.

v_f, μm/rev	Trial 1 d, μm	Trials 2 & 3 d, μm
1.02	254	36
2.03	254	71
3.05	254	107
4.06	254	142
5.08	254	178

Repeatability and the Order of the Trials

Repeatability is typically difficult to address in grinding experiments because of unavoidable changes over time from process parameters such as wheel condition, wheel size, and coolant delivery. Steps need to be taken to minimize the effects of these changes while still performing enough experiments to prove repeatability. Therefore it is desirable to minimize the number of re-grooves since re-grooving the wheel significantly changes the aforementioned wheel diameter which affects the process parameters.

As a result, the three trials were ordered into three blocks of similar diameter, shown in Figure 6.17. The first block of experiments after dressing is done with the non-grooved wheel. The wheel was then dressed and grooved and, again, the experiments were repeated. After this block of tests the grooves were removed and the next non-grooved trial was performed at the new diameter. Also, to address any effects that the order of the infeed rates might have on the results their order was reversed in the second trial.
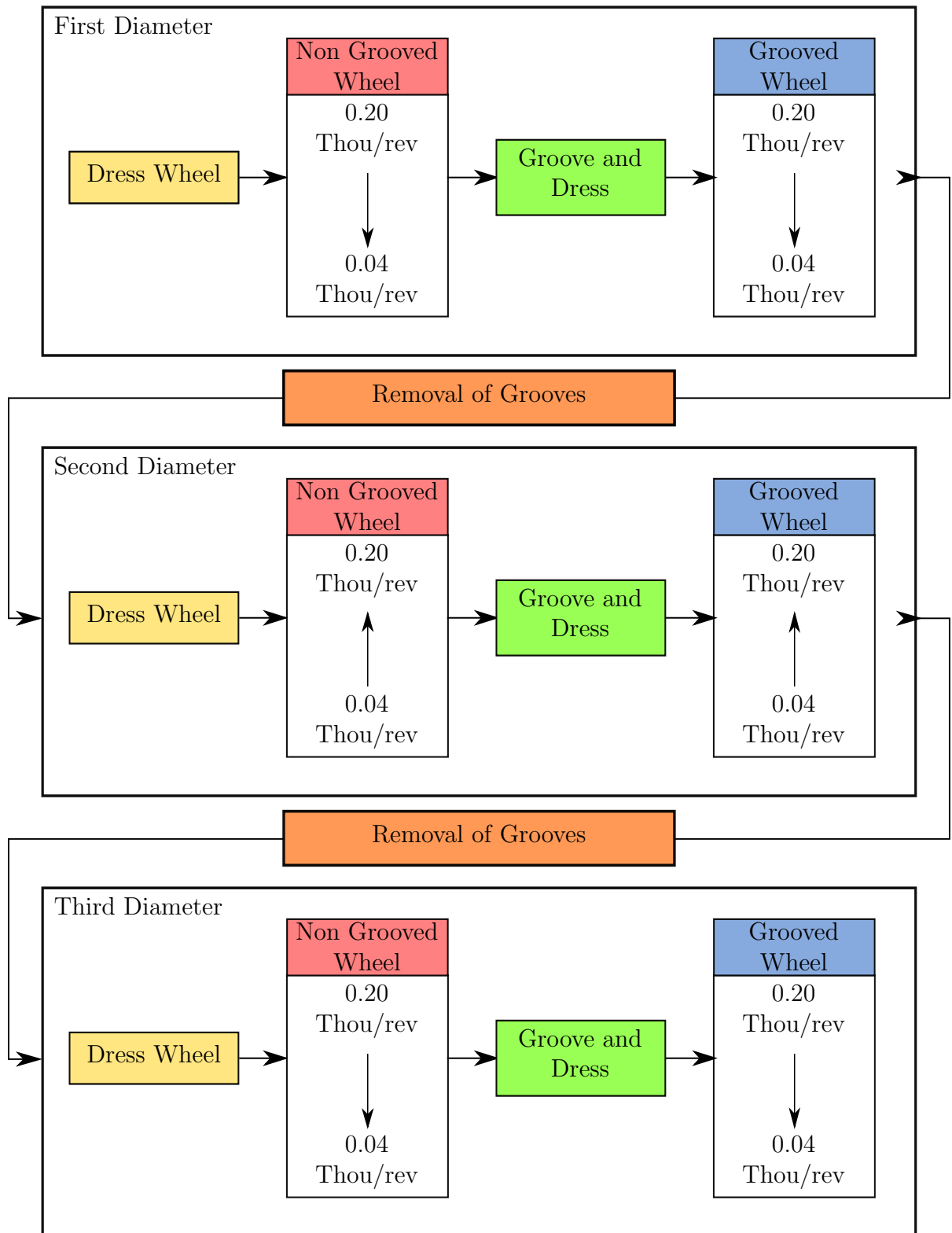
Figure 6.17: The experimental order used to address repeatability

6.3.2 Results of Infeed Comparison

The results presented here are for both the grooved and non-grooved plunge grinding experiments. The power, forces, surface roughness, and roundness are looked at with an emphasis on the relative performance of the grooved wheel compared to a non-grooved wheel. There is also discussion of any conclusions that can be derived from the data, such as specific energy and time constants.

Spindle Power

The spindle power P_s as a function of infeed is given in Figure 6.18 for the grooved (blue) and non-grooved (red) wheels. The results are shown using error bars of one standard deviation with a linear fit drawn between them. The linear fit show an increase in power with increasing infeed for both the grooved and non-grooved wheels. Notable however, was that spindle power for the grooved wheel operations were, on average, 29% lower than for the non-grooved wheel.
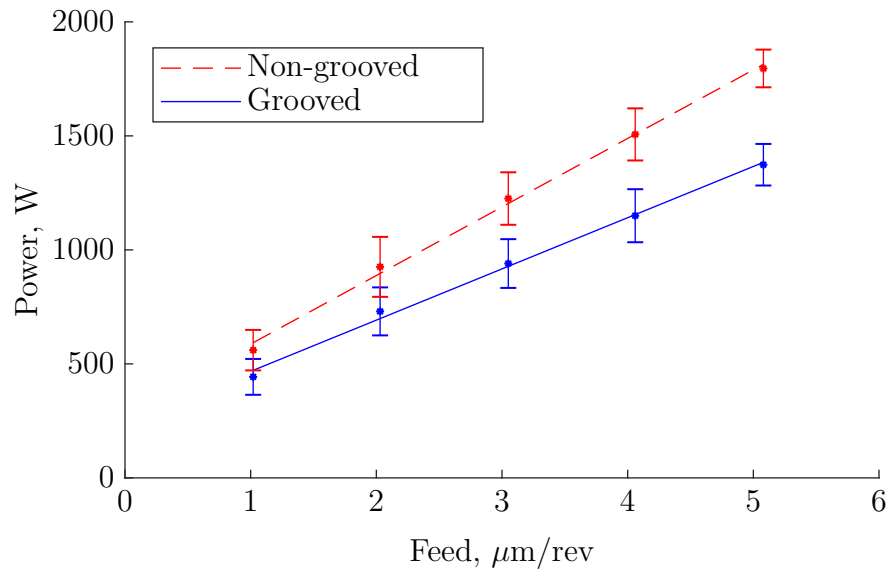
Figure 6.18: Spindle power vs. infeed for plunge grinding of grooved and non-grooved wheels

To highlight the improved efficiency of grooved wheels, the specific energy u of the grinding operation can be derived from P_s using Equation 6.4, where a is the infeed

in mm, b_w is the width of material ground in mm, and v_w is the workpiece speed in mm/s [4]. Shown in Figure 6.19, these results show a clear benefit to using grooved grinding wheels with, in this case, an average reduction of 28% in u across all infeed rates.

$$u = \frac{P_s}{a \cdot b_w \cdot v_w} \tag{6.4}$$
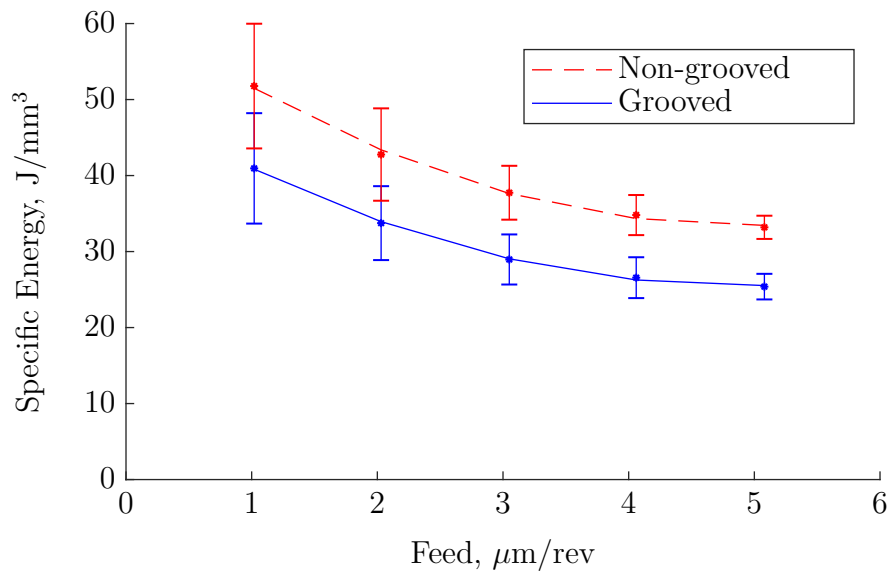
Figure 6.19: Specific energy vs. infeed for plunge grinding of grooved and non-grooved wheels

The shape of the specific energy curves can be explained through the size effect theory, which states that, as the chip size of the removed material increases, the specific energy required to remove that material decreases [4, 64] as illustrated in Figure 6.20. Since an increase in infeed will result in an increase in uncut chip thickness there will be an exponential decline in specific energy similar to that in Figure 6.19.
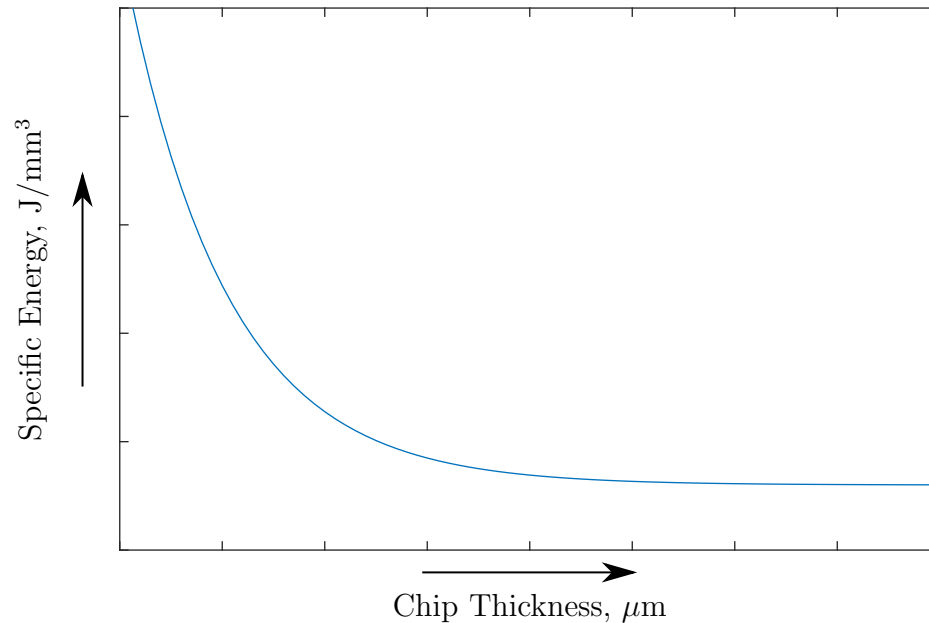
Figure 6.20: The effect of increasing chip thickness on specific energy, adapted from [4]

According to Mohamed *et al.* [33] the specific energy reduction found for the grooved wheel is due to two factors. First, the leading edge of a groove produces a large chip compared to a non-grooved wheel resulting in an increased process efficiency from the size effect. Second, the groove in the wheel allows more coolant into the grinding zone, reducing friction.

Forces

Figure 6.21 shows the normal force as a function of infeed rate for the plunge grinding experiments. The non-grooved (red) and grooved (blue) results are presented using error bars of one standard deviation with a linear fit drawn between them. The linear fit was chosen because it best followed the trend, and all values were taken from the steady-state region of the filtered force curve. Figure 6.21 shows an increase in normal force with increasing infeed. However, as with the power measurements, the normal force of the grooved wheel was about 36% lower than for the non-grooved wheel.
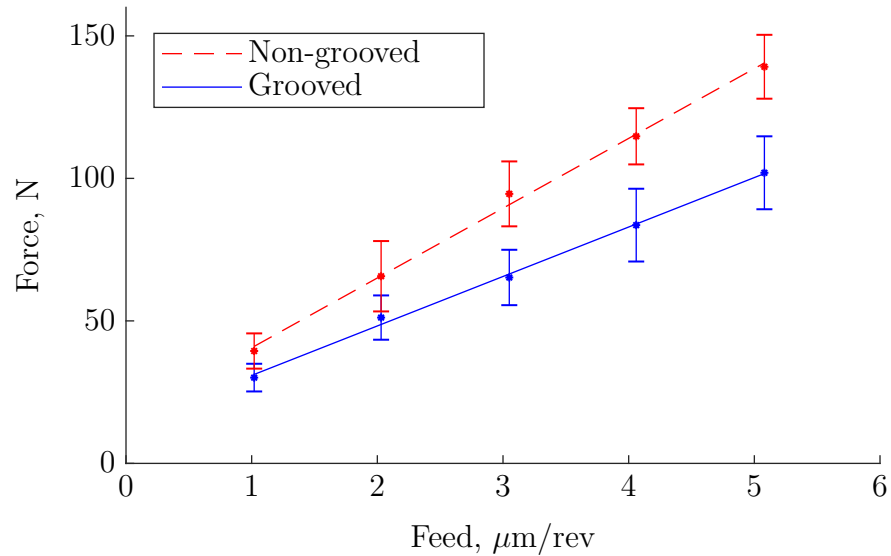
Figure 6.21: Normal force vs. infeed for plunge grinding of grooved and non-grooved wheels

Figure 6.22 is similar to Figure 6.21, except that it shows the tangential force instead of the normal force. Again the non-grooved (red) and grooved (blue) results are presented using error bars of one standard deviation with a linear fit drawn between them to illustrate the trend. That trend is, again, similar to Figure 6.21 in that the force increases with infeed and that the tangential force is lower (in this case by 32%) for the grooved wheel.
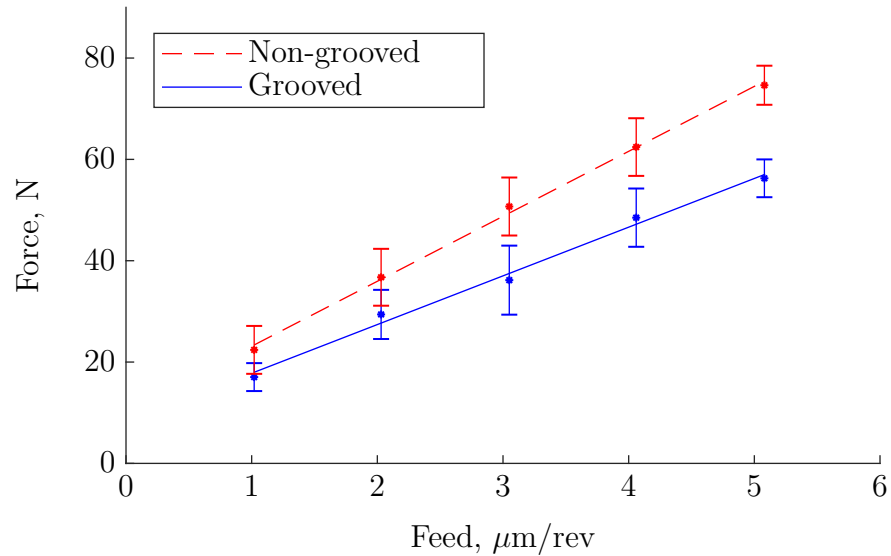
Figure 6.22: Tangential force vs. infeed for plunge grinding of grooved and non-grooved wheels

The increase in force with increasing infeed is predicted with Equation 6.1. This equation could also account for the lower forces observed in the grooved grinding wheel force data if the groove pattern lowers the cutting stiffness k_c. This lower cutting stiffness is likely the result of improved cutting performance from the size effect theory discussed earlier in this analysis, as well as an improved lubricant flow into the contact area, which is a known effect of grooved wheels [33, 42].

Surface Roughness

Figure 6.23 shows the final roughness values for the last two trials, with the non-grooved wheel in red and the grooved in blue. Surface roughness was measured five times per sample with the Pocket Surf (Section 5.4.1) so the error bars here represent one standard deviation of 10 samples over two trials. The grooved wheel data showed increasing surface roughness with infeed while the non-grooved results showed no consistent change over the infeed.
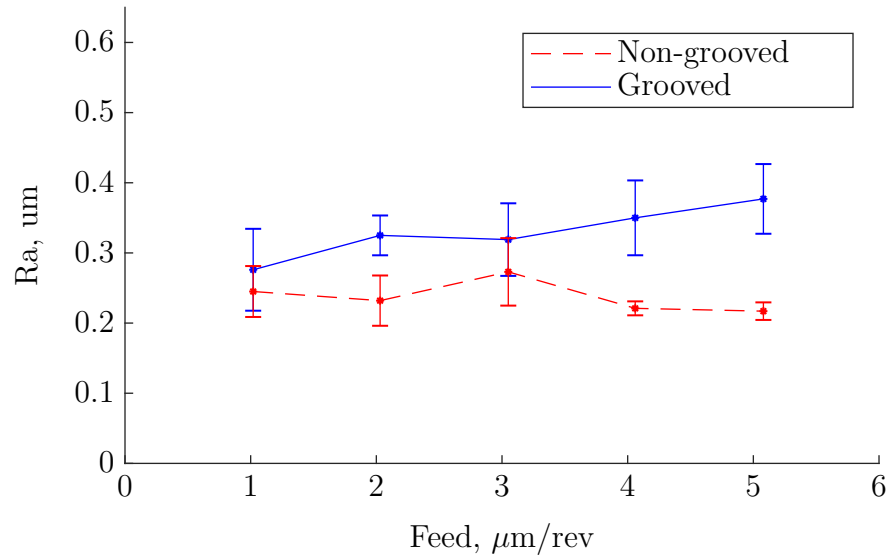
Figure 6.23: Surface roughness vs. infeed for plunge grinding of grooved and non-grooved wheels

There is debate over the effects of grooved wheels on surface roughness [42]. The findings here suggest that grooved wheels perform worse than non-grooved wheels, and that grooved wheels perform worse with increasing infeed. The proposed reason for this increase in surface roughness is that grooved wheels are more susceptible to increased grain fracture as discussed in Section 6.2.2.

Since the wheel wear study had already shown that the grooved wheel pattern used here was more susceptible to fracture wear, it is believed that the higher forces at higher infeed rates accelerated fracture wear which caused increased surface roughness. However, it should be noted that surface roughness values in the range of 0.2 to 0.5 are considered a good quality grinding surface finish [18]. This result means that, while the surface finish after a grooved grinding operation was on average 38% worse, the grooved wheel still gives a satisfactory surface finish for many applications.

Finally, it must be noted that data from all trials was used for the forces and spindle power but not for the surface roughness data. The surface roughness results showed a noticeable effect from wheel wear during the first trial, which was then significantly reduced through modifying the depth of cut. However, the results for the

forces and spindle power were similar through all trials, therefore they were included in the analysis. This inclusion allowed for more confidence in the repeatability of the tests.

Roundness

Roundness was measured using the dial indicator setup described in Section 5.4.2. The dial indicator measurements showed a consistent 0.0003" (7.62 μm) roundness for all ground workpieces independent of whether a grooved or non-grooved wheel was used. The consistency in the roundness measurements was believed to be because of the long spark out time and the inability of the dial indicator to detect changes below 0.0001" (2.54 μm). Therefore it can only be concluded that the roundness of the grooved and non-grooved wheels is the same to a resolution of 0.0001", or 2.54 μm. It is recommended for any future research to use some other form of roundness measurement with a higher resolution.

Time Constants

The time constants were measured using the same method described in Section 6.1.2. Figure 6.24 shows the time constants for grooved (blue) and non-grooved (red) grinding wheels as a function of infeed. They are presented with error bars of one standard deviation. There is a linear fit to show the trend of the data, which is flat and, therefore, not dependent on infeed. The data showed that the time constant is, on average, 12% percent lower for the grooved wheel than the non-grooved wheel. This reduction in time constants means that the grooved wheels completed spark out to within 1% of the commanded depth of cut in an average of 6.81 s, while the non-grooved wheels took 7.72 s to reach the same level of spark out.
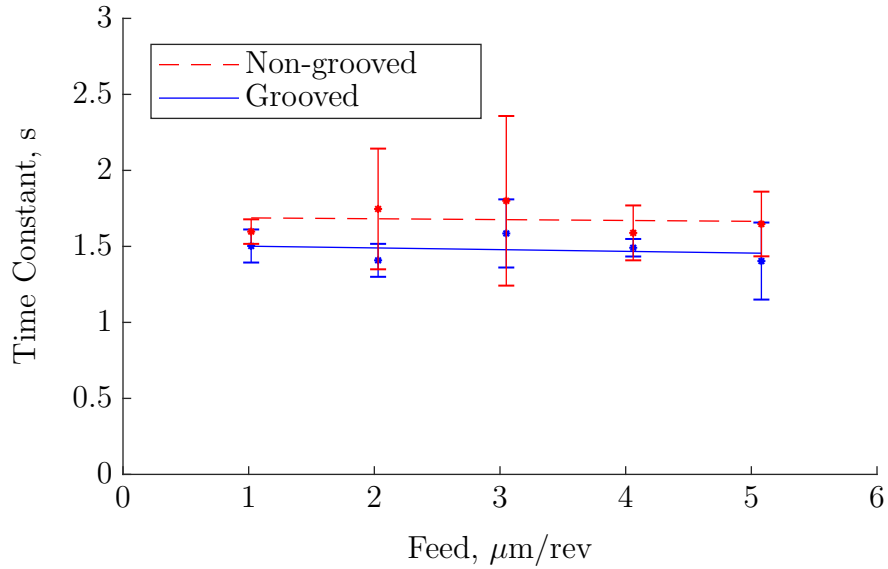
Figure 6.24: Time constants vs. infeed for plunge grinding of grooved and non-grooved wheels

Knowing that the infeed rate v_f is the same for the grooved and non-grooved tests, and that the normal force F_n has already been found to be 36% lower for grooved wheels, Equation 6.2 predicts a similar 36% drop in the time constants. The fact that Figure 6.24 shows the time constants were independent of infeed rate and that the reduction in the time constants for grooved wheels was only 12%, suggests that the effective stiffness k_e was impacted by both the wheel grooving and the infeed rate.

As discussed in Section 6.1.2, the effective stiffness k_e can be represented as three springs in series. Equation 6.5 gives the relationship between the effective stiffness and the three springs, where k_w is the stiffness of the rotary axis, k_s is the stiffness of the grinding machine, and k_a is the contact stiffness [4]. k_w and k_s are dependent on the rigidity of the rotary axis and the grinding machine, respectively, so they would not change significantly between experiments. k_a is, therefore, the important term in this analysis.

$$k_e^{-1} = k_w^{-1} + k_s^{-1} + k_a^{-1} \tag{6.5}$$

While diffcult to quantify exactly, Snoeys and Brown [62] proved that the contact stiffness k_a is dependent on the contact area between the wheel and the workpiece and the normal force applied. As F_n increases, so does the k_a, which explains why the time constants for both the grooved and non-grooved wheels in Figure 6.24 are independent of infeed.

Figure 6.25 shows a cross-section of the contact between the wheel and workpiece for grooved and non-grooved wheels. The groove pattern causes a significant decrease in the amount of wheel in contact with the workpiece at a given time. For the groove pattern in Table 5.5 the decrease is 50%. This decrease in contact area likely decreases contact stiffness for grooved wheels compared to non-grooved wheels, which in turn could explain why the reduction in time constants was not greater than 12% for the grooved wheel.
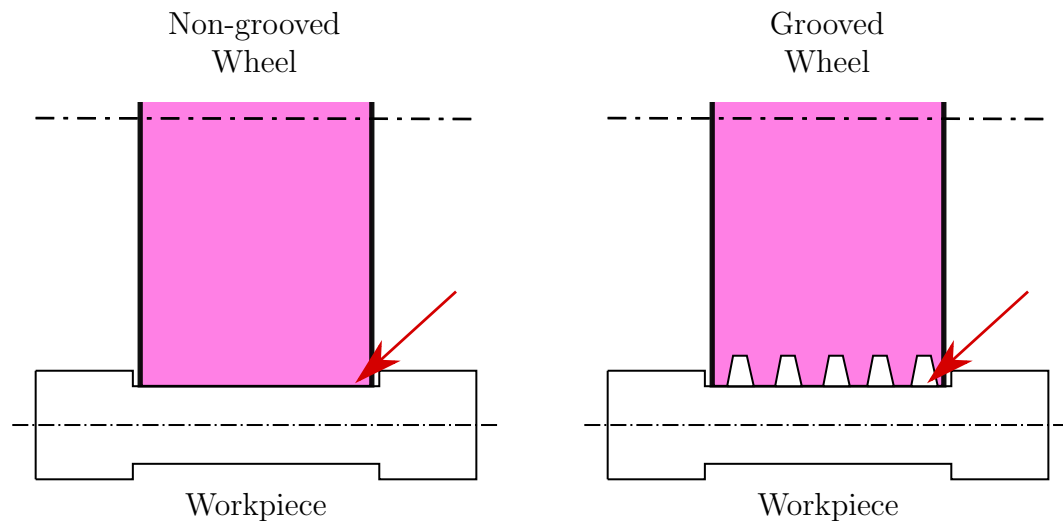
Figure 6.25: The difference in the amount of wheel in contact with the workpiece for grooved and non-grooved wheels

6.3.3 Conclusion for Infeed Comparison

Overall the use of circumferential grooving greatly impacted the plunge grinding process. There were beneficial changes to the grinding forces, spindle power, specific energy, and time constants of the process, while the surface roughness was negatively impacted. There was also no measurable difference to the roundness. Table 6.7 gives

a summary of the impacts. These characteristics of circumferential grooved wheels makes them well suited to roughing operations where surface finish is not as much of a concern.

Table 6.7: The benefits of using grooved grinding wheels in cylindrical grinding

Effects of Grooved Wheel	
Normal Force	-36%
Tangential Force	-32%
Spindle Power	-29%
Specific Energy	-28%
Surface Roughness	+38%
Roundness	No Effect
Time Constants	-12%

Benefits of Grooved Wheels	Points of Debate	Other Effects
Lower Forces	Improves Coolant Flow	Texturing
Lower Specific Energy	Increased Wheel Wear	
	May Worsen Suface Finish	

6.4 Effect of Speed Ratios on Texturing and Surface Finish for Circumferentially Grooved Wheels

The final plunge grinding study explored the significance of the angular speed ratio r_ω between the grinding wheel and the workpiece. This study of angular speed ratios (which are described using Equation 6.6) with grooved wheels in plunge grinding is a new area of research that is not seen in the literature. A series of experiments were performed at various speed ratios and the effects on forces, spindle power, and surface roughness were observed. This study produced some interesting results, including the ability to apply textures to the workpiece using a circumferentially grooved wheel, and a proposed explanation of how texturing is achieved.

$$r_w = \frac{\omega_s}{\omega_w} \tag{6.6}$$

6.4.1 Setup

For these plunge grinding experiments, five tests were performed. Four of the tests were with a grooved wheel (with the same parameters described in Table 5.5) and the fifth was with a non-grooved wheel. The test parameters are given in Table 6.8, the initial dressing conditions are shown in Table 5.4, and the five tests and their respective speed ratios r_ω are given in Table 6.9. The other notable difference from previous studies is that the dwell time was reduced from 15 s to 5 s to prevent any textures from being wiped off from excessive spark out. Finally, all workpieces were prepared with a light grind at an infeed rate of 1.27 μm/rev to a depth of 50.8 μm to provide a regular starting condition for all tests.

Table 6.8: The grinding parameters used in the speed ratio study

Grinding Parameters	Value	Units
Workpiece Speed	200-250	rpm
Wheel Speed	1000	rpm
Wheel Diameter	385	mm
Infeed Rate	1.27	m/rev
Depth of Cut	76.2	m
Dwell Time	5	s

Table 6.9: The speed ratios used for the six tests

Test	Workpiece Speed, rpm	Wheel Speed, rpm	Speed Ratio	Grooved Wheel
1	200	1000	5.00	Yes
2	205	1000	4.88	Yes
3	210	1000	4.76	Yes
4	222	1000	4.50	Yes
5	250	1000	4.00	Yes
6	222	1000	4.50	No

6.4.2 Results

Forces and Spindle Power

Figure 6.26 shows the spindle power over time for the $r_\omega = 4.88$ experiment (A) and the $r_\omega = 5.00$ experiment (B). The spindle power curves for integer speed ratios are

unlike the typical plunge grinding curves seen in previous studies. After the initial spark in the spindle power continues to increase without reaching a steady state. The grinding forces for integer speed ratios also show this linear increase. For Figure 6.27, as well as for Figure 6.28, the values for the force and spindle power were taken right before spark out. This behavior is the same for the $r_\omega = 4.00$ curves as well. The effects of texturing is the suspected reason for this difference in curve shape, as will be discussed. To compare these curves to the non integer speed ratio curves the force and power values were taken right before spark out.
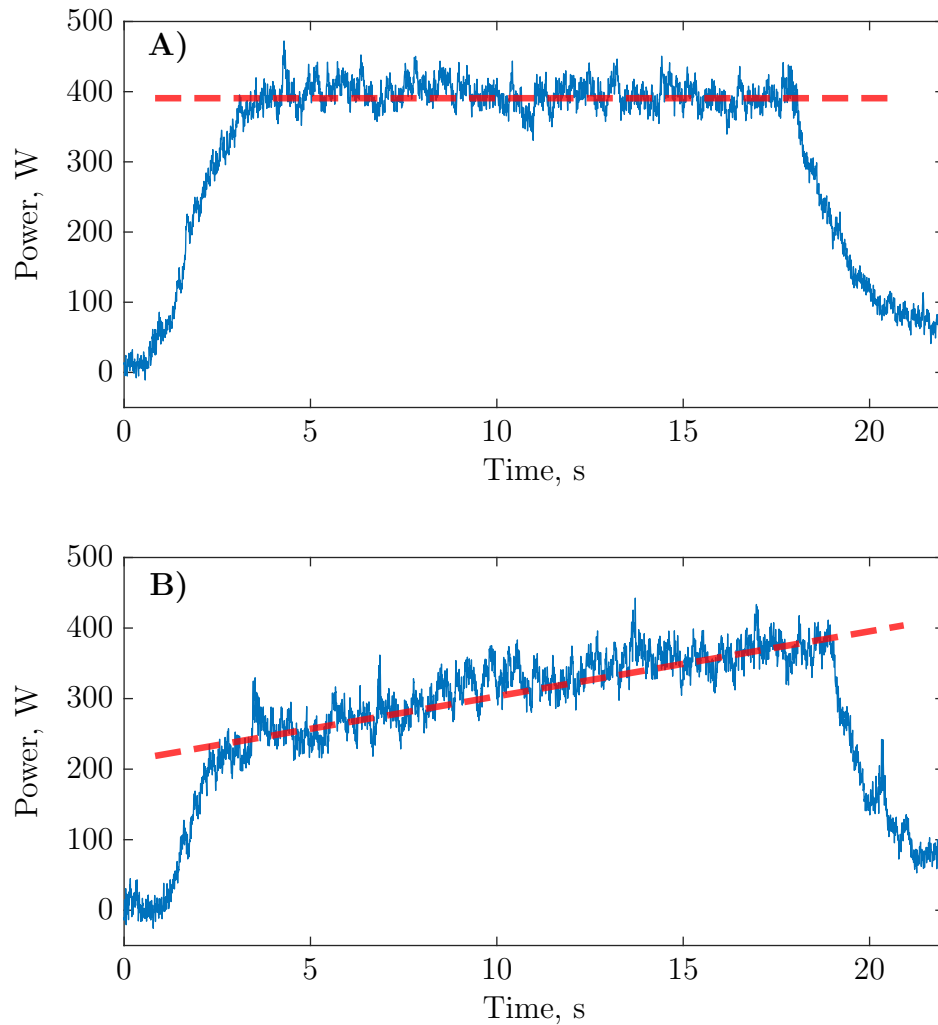
Figure 6.26: The spindle power curves for the plunge grinding experiments at r_ω=4.88 (A) and r_ω=5.00 (B).

Figure 6.27 shows the normal force measurements from all six experiments. The

results from the grooved wheel are blue while the non-grooved wheel is red. The forces involved were low compared to the last study (Section 6.3), because of the lower workpiece speeds and low infeed rate. This less aggressive grinding could explain why there is not a large difference between the grooved and non-grooved forces at $r_\omega = 4.50$. There is a linear downward trend to the results, with some interesting data points at $r_\omega = 4.76$ and 4.88.
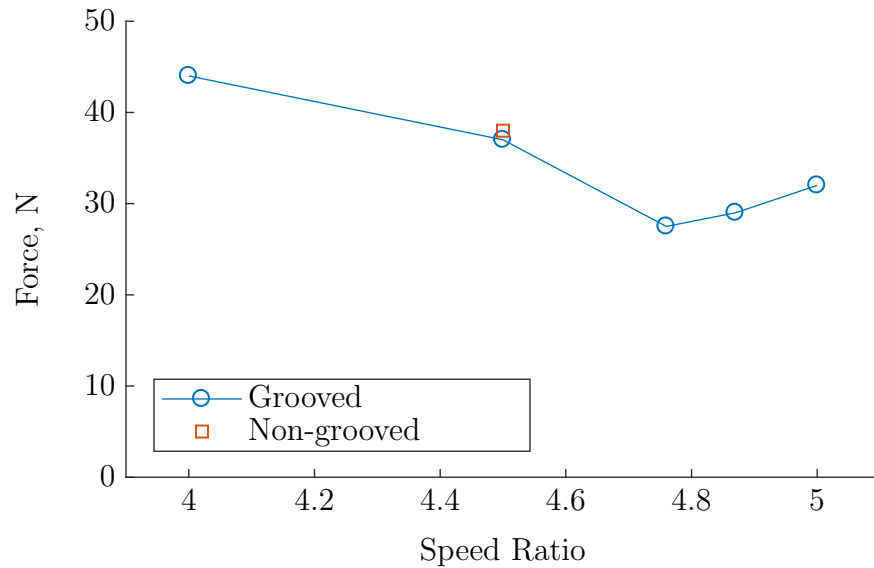
Figure 6.27: The normal force results for the plunge grinding speed ratio study.

The spindle power data for all tests is presented in Figure 6.28. It follows the same trend as the normal force data, with the power decreasing linearly with increasing r_ω except for nonlinear results at $r_\omega = 4.76$ and 4.88. Again, as expected, the non-grooved grinding wheel uses more power than the grooved wheel at $r_\omega = 4.50$.
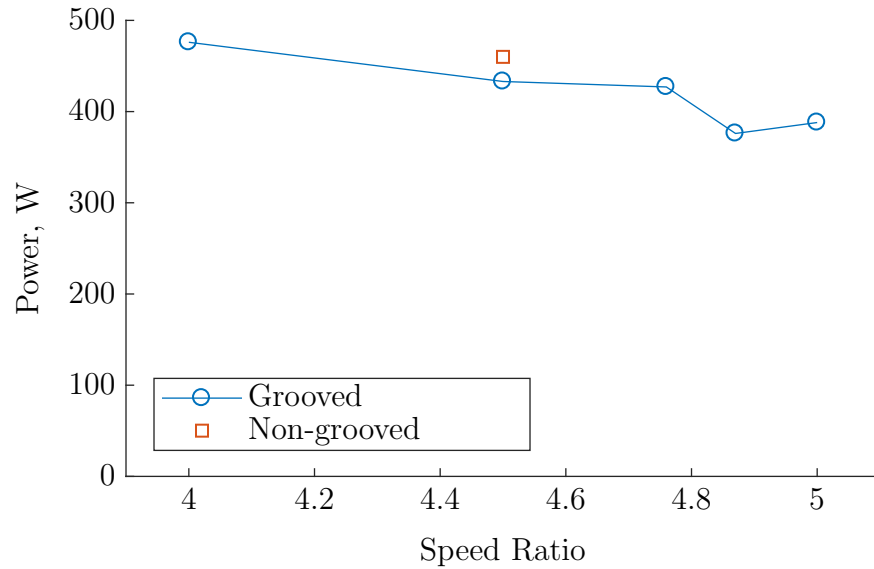
Figure 6.28: The spindle power results for the plunge grinding speed ratio study.

The downward trend of the forces and power with increasing speed ratio is because of the lower workpiece speed and the associated lower MRR. However that is not to say the speed ratio does not have an effect, which might be seen in the results at r_ω = 4.76 and 4.88. To further explore the effect speed ratios have on spindle power and forces it is recommended that more aggressive tests be performed over a larger range of speed ratios.

Texturing

The most striking effect of using integer speed ratios is the texture that is imparted on the workpiece. Figure 6.29 shows the ground samples for the 4.76, 4.00, and 5.00 speed ratios. A threadlike pattern is visible on the integer speed ratios, while the 4.76 speed ratio sample, which is a fair representation for all non integer samples, is included as comparison. This section will examine this pattern using the r_ω = 5.00 sample as an example.
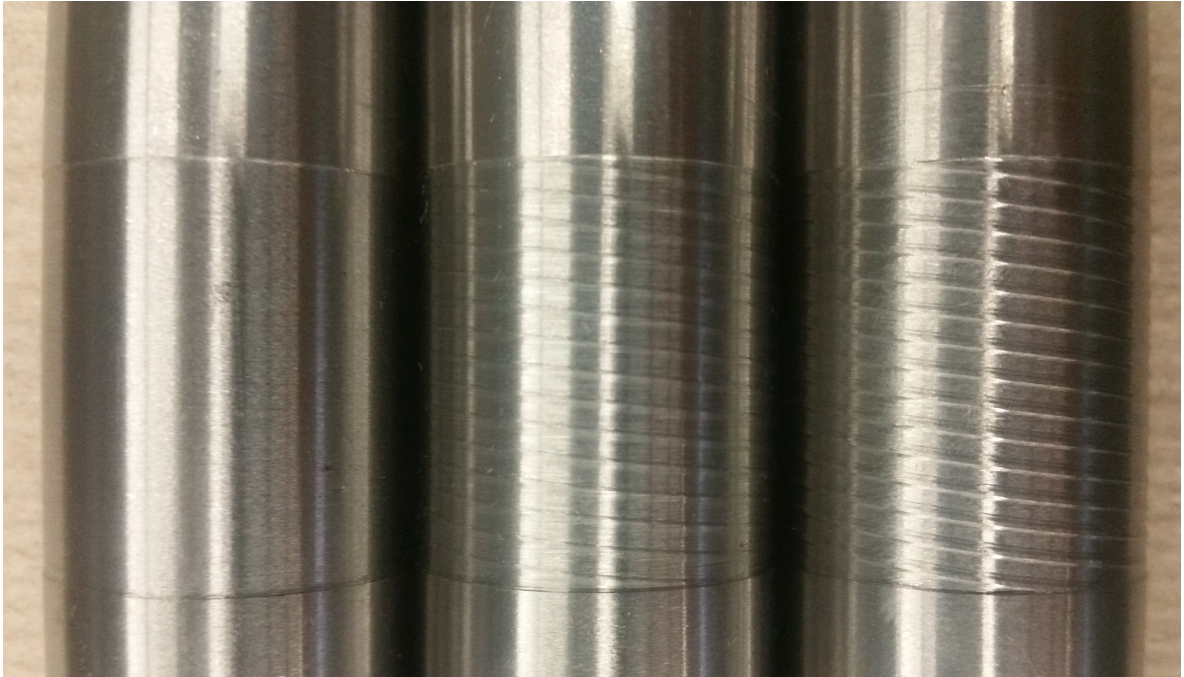
$r_\omega = 4.76$ $\qquad\qquad\qquad$ $r_\omega = 4.00$ $\qquad\qquad\qquad$ $r_\omega = 5.00$

Figure 6.29: Visible texturing at speed ratios of 4.00 and 5.00. Sample from speed ratio 4.76 test shown for comparison.

Using the Nanovea profilometer the shape of the texture can be further explored. Figure 6.30 shows a 3D view of the pattern for the $r_\omega = 5.00$ sample. Visible are threads with a flat top, with smoothly ground workpiece sections between them. Figure 6.31 shows a profile of this same sample. The regularity of the thread pattern is apparent, as is the thread height of 77 μm. This thread height is significant because it is approximately the depth of cut for the test; therefore, the top of the threads were not ground at all during the plunge or dwell of the grinding operation.
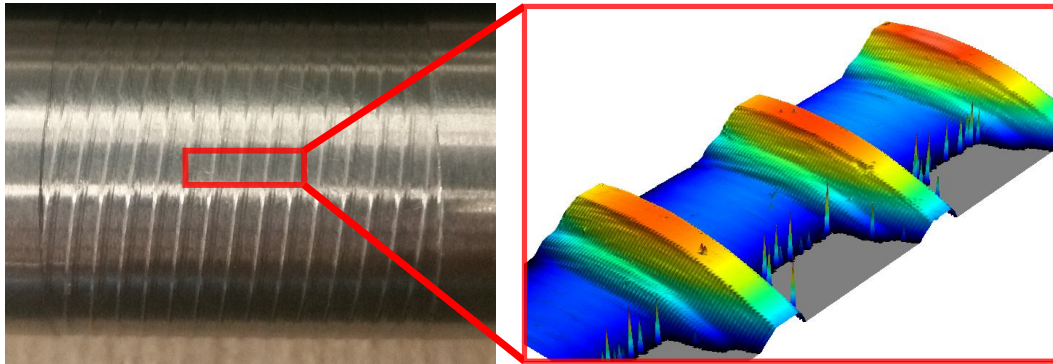
Figure 6.30: A 3D rendering of the area scan for $r_\omega = 5.00$ shows the texture's shape.
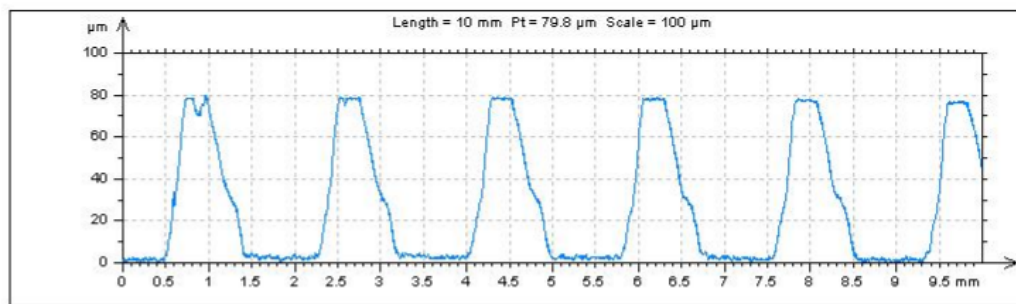
Figure 6.31: The profile of the grooves from the $r_\omega = 5.00$ test.

Comparing the $r_\omega = 4.00$ sample to the $r_\omega = 5.00$ sample the notable difference is that there are four distinct threads around the circumference for the former and five distinct threads for the latter. This thread number will be important in the texturing hypothesis in Section 6.4.3.

Finally, the profile can also provide an explanation to the gradually increasing forces and power seen in Figure 6.26. As the depth of cut increases through the plunge grinding operation, more of the grinding wheel is engaged with the workpiece which would cause increasing forces and spindle power.

Roughness

Figure 6.32 gives the surface roughness results for all tests. Unlike previous studies, the Nanovea profilometer was used for these roughness measurements. The profilometer was used because it allows for surface roughness measurements of the ground portion

between the threads of the integer speed ratios. The pattern for the grooved wheel results is similar to the normal force and spindle power, with the dip around $r_\omega = 4.88$. This dip in the data lends more credibility to possible benefits of speed ratios near integer values. Also, as seen in the previous study (Section 6.3) the non-grooved wheel has a better surface finish than the grooved wheel at $r_\omega = 4.50$.
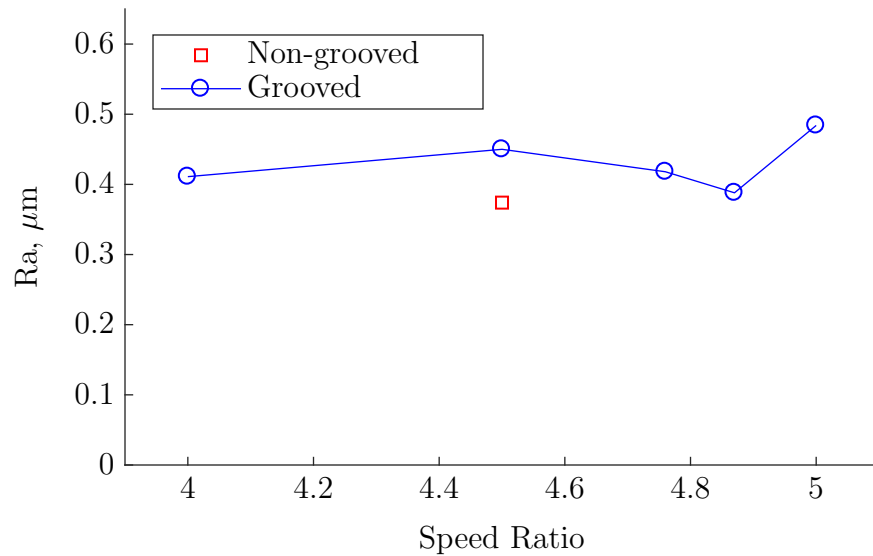
Figure 6.32: The surface roughness measurements for the non integer speed ratios for grooved and non-grooved tests.

6.4.3 Texturing Explanation

This section aims to explain the texturing phenomenon by adapting Tlusty's chatter wave formula [65]. The equation will be introduced, applied to cylindrical grinding, and then compared to the experimental results. Overall it was found that this phasing equation fits well with the experimental results and can be used to help design future experiments.

Chatter Wave formula

Chatter is a self-excited vibration that can occur in machining that causes large periodic variations in cutting forces and leaves a wavy finish on the workpiece.

According to Tlusty, one of the mechanisms that can cause this self-excitation is the regeneration of waviness. Figure 6.33 shows how the chip thickness can vary as the tool oscillates along a workpiece. The size of the chip is dependent on the phase between the tool oscillation frequency and the existing surface wave.
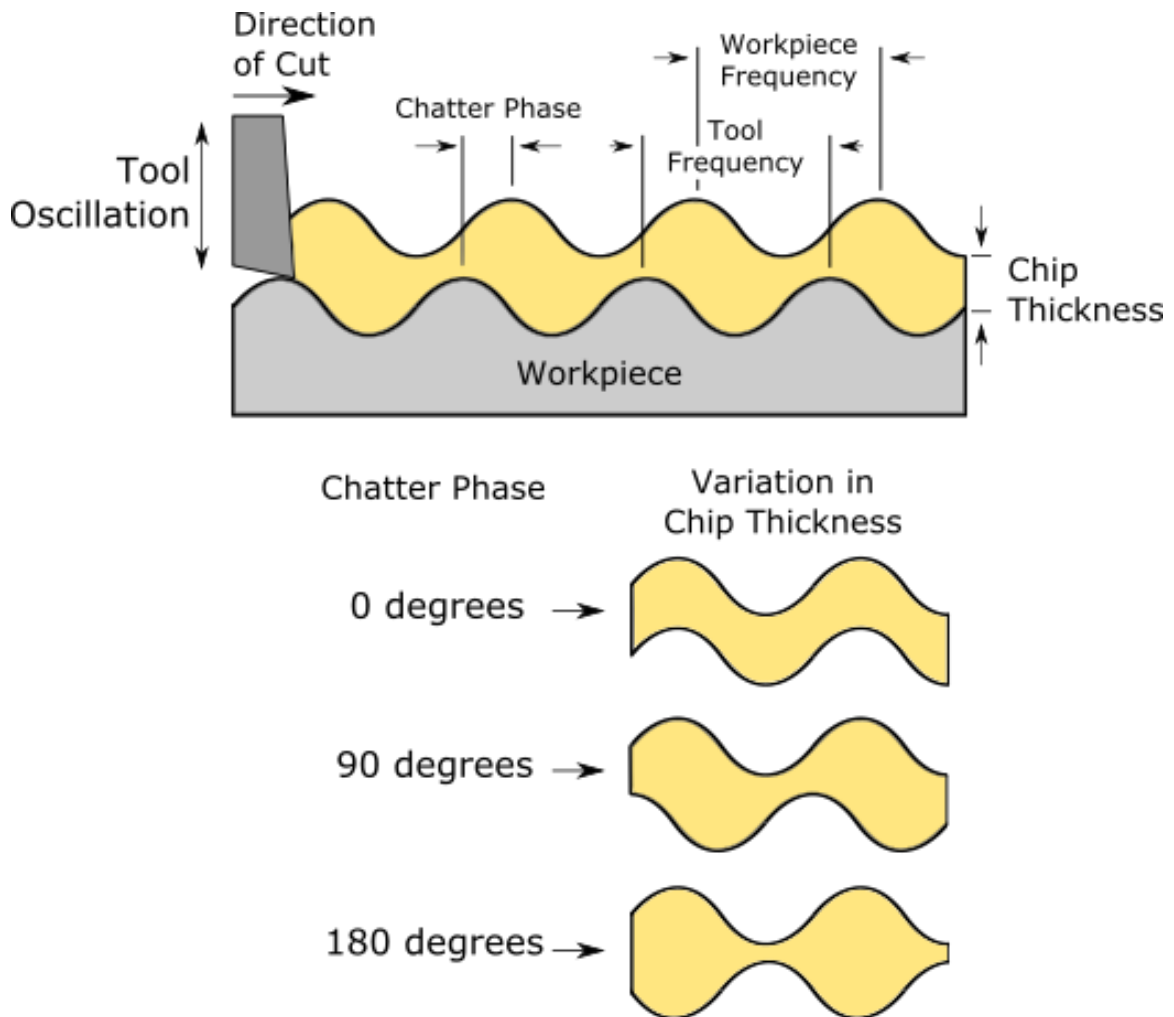
Figure 6.33: Wave regeneration with the variation of chip thickness for different ϵ values. Adapted from [65].

Equation 6.7 is the chatter wave formula that describes wave regeneration, where ϵ is the chatter wave phase, f is the chatter frequency of the tool, n is the workpiece speed, and N is the number of complete chatter waves. This equation, taken from Tlusty [65], was designed for turning operations but can be modified to examine when a grooved wheel is engaged with the workpiece.

$$\epsilon = 2\pi \cdot (\frac{f}{n} - N) \qquad (6.7)$$

To modify Equation 6.7, consider the cross section of the grooved grinding wheel shown in Figure 6.34. The cross section of a $\eta = 50\%$ circumferentially grooved wheel is essentially half grooved and half not grooved. During plunge grinding this cross section of the wheel would then only be engaged for half of every revolution; therefore, the tool frequency f in this case is controlled by the wheel angular velocity ω_s while the workpiece speed n is now the workpiece angular velocity ω_w. The ratio between ω_s and ω_w is the speed ratio r_ω that has been used throughout this study. After applying these modifications, Equation 6.7 becomes Equation 6.8, and the chatter wave phase ϵ will now be referred to as the wheel contact phase ϵ_g.

Wheel Rotation

Grooved Section

Grinding Wheel Cross Section

Non Grooved Section

Workpiece

Workpiece Rotation
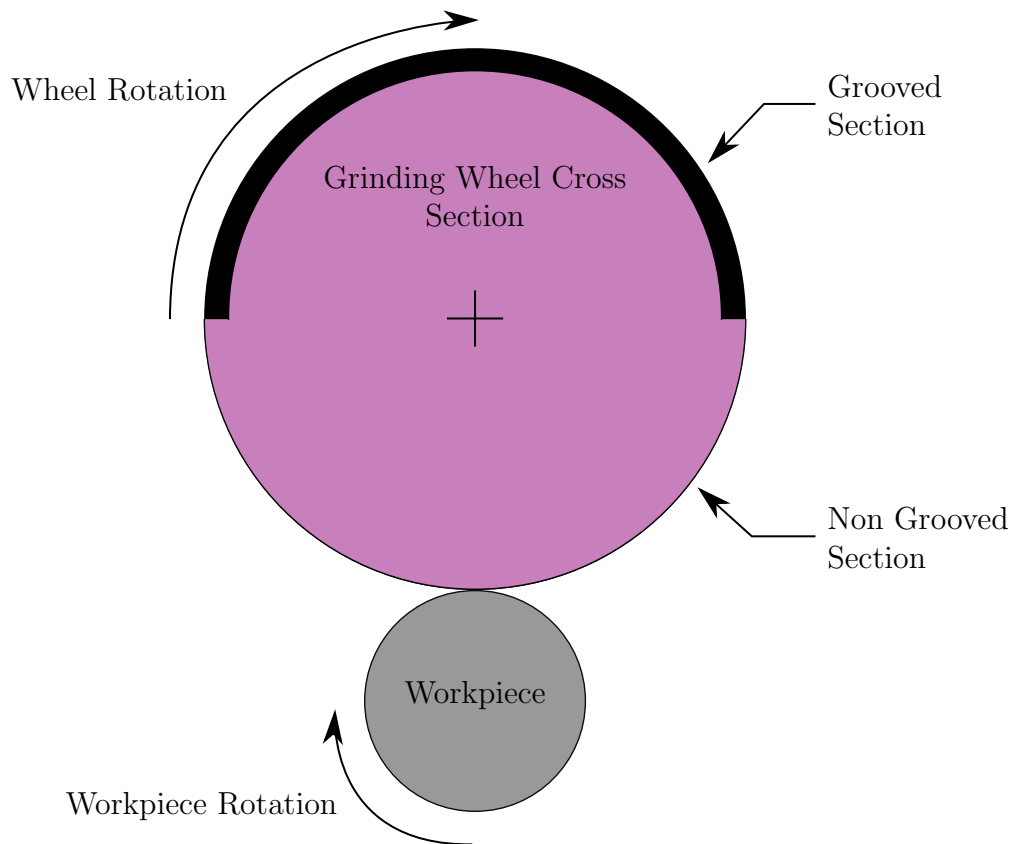
Figure 6.34: The cross section of $\eta = 50\%$ circumferentially grooved wheel in contact with a workpiece

$$\epsilon_g = 2\pi \cdot (\frac{\omega_s}{\omega_w} - N) \tag{6.8}$$

The wheel contact phase ϵ_g represents how well the cutting action on one pass, or revolution, of the workpiece lines up with the next. If $\epsilon_g = 0$, then the revolutions are fully synced and the tool will contact the workpiece in the same way each pass. If $\epsilon_g = \pi$, then the revolutions are completely out of sync and the tool contact will be the exact opposite during each pass. Other values of ϵ_g will behave somewhere between these extremes. The number of chatter waves N is dependent on the form left by the previous pass. In this case N is equal to the nearest integer value to r_ω, rounded down.

Theoretical Example

Equation 6.8 and its application to grinding is best explained through a case study. Figures 6.35, 6.36, and 6.37 give three examples of what will happen to the workpiece at low speed ratios over three grinding wheel revolutions.

The first case is a speed ratio of 1.0, meaning for every revolution of the grinding wheel the workpiece also completes one revolution. This integer speed ratio gives a wheel contact phase value of 0. If the material removal is exaggerated it is apparent from Figure 6.35 that the grooved and non-grooved portions of the wheel always contact the same locations on the workpiece every revolution. Therefore, by the third revolution half of the wheel has been ground to the commanded depth of cut and half of the wheel has not been touched.

For the second case in Figure 6.36 the speed ratio is 1.5 and, therefore, the phase is π. For this phase value, the wheel contacts a different third of the workpiece after each revolution. These alternating wheel paths mean that the entire workpiece will be ground. Another interesting result of this phase angle is that the infeed in the portions ground are twice as large as the commanded infeed, somewhat like what was shown in Figure 6.33 at a chatter phase of 180°. This increase in the specific infeed

should translate to larger chips of material being removed.

The third case in Figure 6.37 shows what is expected from a speed ratio of 2.0. Since this speed ratio is again an integer value, the phase is 0. Therefore, it behaves much like the first case by only grinding half the workpiece surface; however, the pattern (or texture) on the workpiece cross section is different. The number of unground sections of the cross section is directly related to r_ω. If $r_\omega = 1.0$, there is one unground section, if $r_\omega = 2.0$ there are two, and so on.

To summarize this case study, if the speed ratio is an integer, then there will be a texture imparted on the workpiece. The number of unground sections on this texture is equal to the speed ratio r_ω. Other speed ratios grind the entire workpiece given enough time, or revolutions, with $\epsilon_g = \pi$ being an interesting case where the infeed of the sections ground in a given pass are twice as thick as expected.

Wheel Revolutions

Figure 6.35: The theoretical example for speed ratio $= 1.0$. The blue dot is tracked over 1 revolution of the grinding wheel.

Figure 6.36: The theoretical example for speed ratio = 1.5. The blue dot is tracked over 1 revolution of the grinding wheel.

Wheel Revolutions

Initial State $\longrightarrow$ First Revolution $\longrightarrow$ Second Revolution $\longrightarrow$ Third Revolution

$r_w = 1.0$
$\epsilon_g = 0$

ω_s

Wheel

ω_w

Workpiece
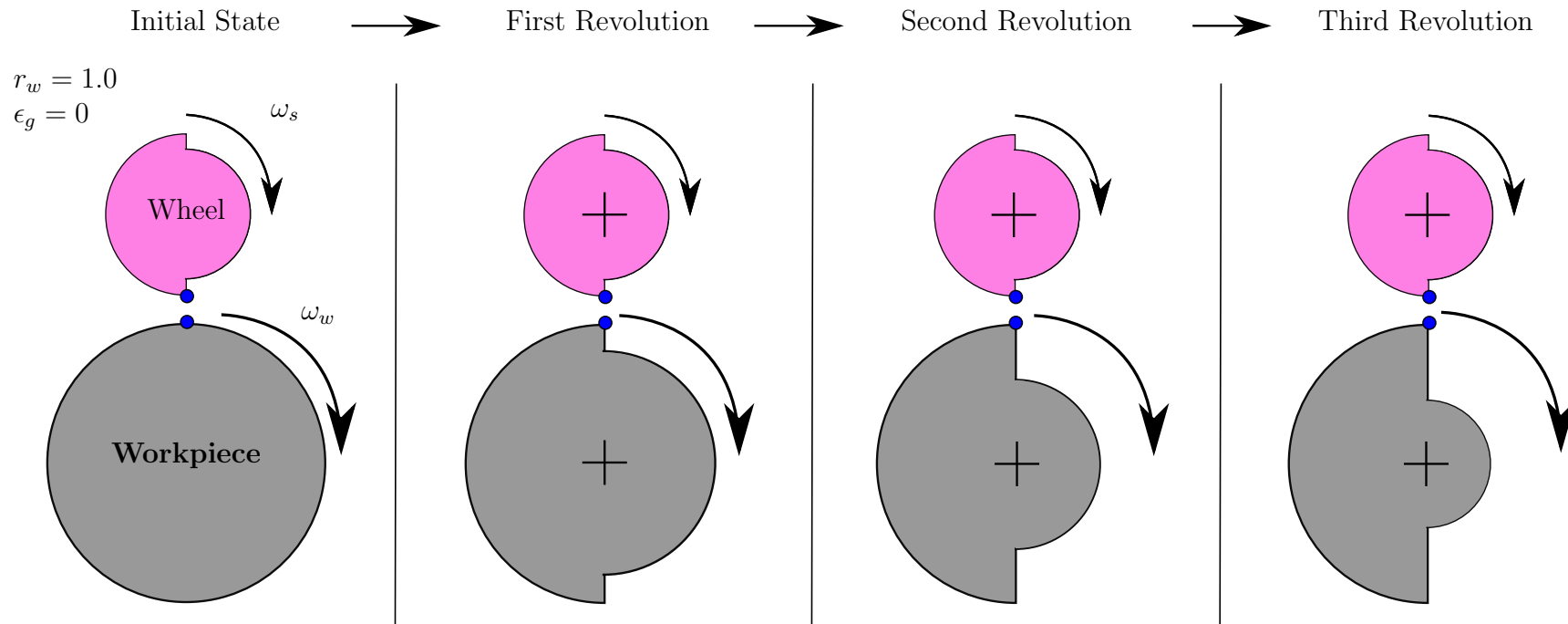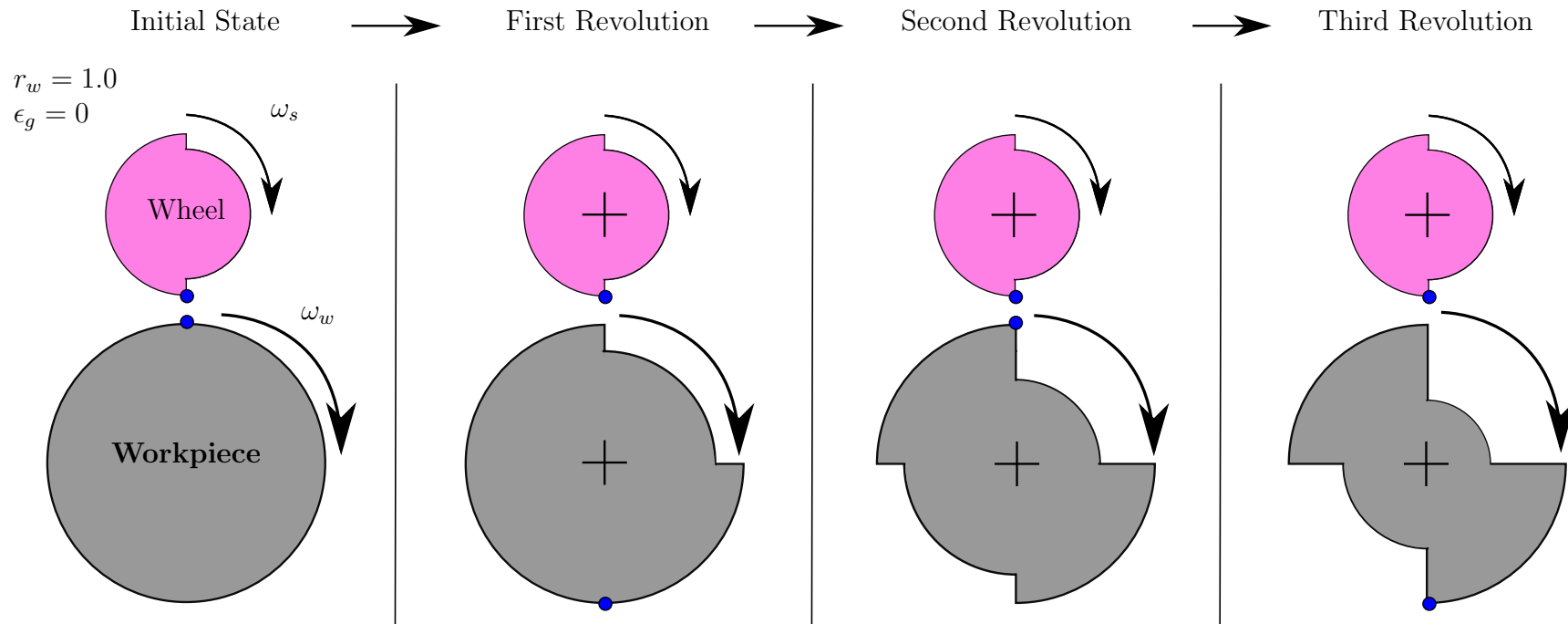
Figure 6.37: The theoretical example for speed ratio = 2.0. The blue dot is tracked over 1 revolution of the grinding wheel.

Comparison to Experimental results

This explanation for the texturing agrees well with the experimental results. As already stated, the $r_\omega = 4.00$ and 5.00 samples show distinct unground portions, the number of which is equal to their respective integer values. The other tests, with their ϵ_g values shown in Table 6.10, showed no signs of texturing.

Table 6.10: The ϵ_g values for the plunge speed ratio study

Test	Speed Ratio	ϵ_g	Texture Observed
1	5.00	0.00	Yes, 5 Threads
2	4.88	1.76π	No
3	4.76	1.52π	No
4	4.50	1.00π	No
5	4.00	0.00	Yes, 4 Threads

The behavior of the tests where $\epsilon_g \neq 0$ are harder to align with this theory because the spark out removes any obvious texture. However, the wheel contact phase and the resulting changes in infeed along the workpiece could potentially explain the variations in force, spindle power, and surface roughness. For example, the larger force and surface roughness observed in test 4 could be explained by the larger infeed when $\epsilon_g = \pi$.

6.4.4 Conclusion to Speed Ratio Study

This study was designed as preliminary work into an original topic. Expanding this research is beyond the scope of this thesis, but is highly recommended. The suggested directions for future study are to expand the range and number of ϵ_g values studied from 0 to 2π to explore interesting effects close to $\epsilon_g = 0$, and to perform more aggressive grinding operations that will better show relative changes in forces, spindle power and surface roughness.

What can be concluded with the current work is that using integer speed ratios with a $\eta = 50\%$ circumferentially grooved wheel can impart a thread-like texture to the workpiece. The shape of this texture is dependent on the value of the speed ratio. Finally, the wheel contact phase equation can be used to help explain the grinding

behavior at different speed ratios, particularly related to the prediction of texture patterns.

Chapter 7

Conclusion

7.1 Thesis Summary

The objectives of this thesis were to design and build a rotary axis to enable cylindrical grinding research, develop the methods needed to analyze cylindrical grinding using the data collected, and then use that data to explore the effects of grooved grinding wheels in cylindrical plunge grinding. This chapter summarizes the discoveries made while meeting these objectives, and provides recommendations on future applications of the rotary axis.

Rotary Axis

The rotary axis successfully met the six design requirements set for it. The rotary axis was able to achieve the full 0-500 rpm speed range and maintain that speed to within 1%, even under aggressive grinding conditions. The motor was selected to provide ample torque to withstand theoretical forces that were twice as large as what was later seen experimentally. The force dynamometer enabled the measurement of in-process forces, and the dynamic characteristics of the system did not interfere with said force measurements. The machine was also made to be safe to operate and was capable of withstanding extensive, direct coolant spray without adverse effect.

Plunge Grinding Studies

The first study on the effect of workpiece stiffness in cylindrical plunge grinding found a 2.5 fold decrease in effective stiffness between the two grinding locations along the workpiece. This lower stiffness drastically increased the time constants and adversely affected the production time, workpiece roundness, and surface roughness. This initial

study also provided a proof of concept for the processing of raw data from the rotary axis.

The second study was the wheel wear comparison between grooved and non-grooved wheels showed accelerated wheel wear with the grooved wheels. This increased wear was suspected of being linked to a weakening of the abrasive grains and the bond that holds them together caused by the grooving process.

The third and largest study, comparing the performance of grooved and non-grooved wheels over multiple infeed rates, showed the benefits of circumferentially grooved wheels in cylindrical grinding. There was an observed 36% reduction in normal force, a 32% reduction in tangential force, a 29% reduction in spindle power, a 28% reduction in specific energy, and a 12% decrease in the time constants. The roundness showed no measurable change and the surface roughness increased by 38%. This result led to the conclusion that this groove pattern would be advantageous in roughing operations.

The fourth study examined the variations in textures, grinding forces, power, and surface finish observed over different speed ratios. Tlusty's chatter wave phase equation was modified and showed the ability to predict the number of threads produced during the texturing of a workpiece. This unique area of research has the potential to inform the debate on whether grooved grinding wheels improve or degrade surface finish.

7.2   Recommendations

There is a broad horizon of potential research using the rotary axis. Most apparent is further exploration of the effects of speed ratios using grooved wheels in cylindrical grinding. The research is straightforward and the results could explain the inconclusive surface roughness findings seen in literature. However, further studies into how different groove patterns behave during cylindrical grinding would also be valuable, as would be a thorough examination of the wear mechanisms of grooved wheels in cylindrical grinding which could take advantage of the Grinding Lab's wheel scanner. The acquisition of an improved roundness measuring system would also add value to

any cylindrical grinding research.

The rotary axis itself could also be upgraded by stiffening the system. This improvement could be accomplished by using a thicker mounting plate, or by adding supports to the existing plate. Also, the addition of a live center to the rotary axis would enable realistic traverse grinding experiments which would further expand the research opportunities the rotary axis provides.

Bibliography

[1] M. P. Groover, "Grinding and Other Abrasive Processes," in *Fundamentals of Modern Manufacturing*, pp. 585–609, John Wiley & Sons, second ed., 2004.

[2] T. Drozda, C. Wick, J. T. Benedict, R. F. Veilleux, and Society of Manufacturing Engineers, *Tool and manufacturing engineers handbook: a reference book for manufacturing engineers, managers, and technicians*. Dearborn, Mich: Society of Manufacturing Engineers, 4th ed., 1983.

[3] American National Standards Institute, *American national standard: markings for identifying grinding wheels and other bonded abrasives*. ANSI ; B74.13-1982, New York, NY: American National Standards Institute, 6th ed., 1982.

[4] S. Malkin, *Grinding Technology: Theory and Applications of Machining with Abrasives*. Ellis Horwood Series in Mechanical Engineering, Halsted Press, 1989.

[5] M. Younis, M. M. Sadek, and T. El-Wardani, "A New Approach to Development of a Grinding Force Model," *J. Eng. Ind*, vol. 109, pp. 306–313, Nov. 1987.

[6] R. S. Hahn, "On the Mechanics of the Grinding Process Under Plunge Cut Conditions," *J. Eng. Ind*, vol. 88, pp. 72–79, Feb. 1966.

[7] S. Malkin and R. B. Anderson, "Thermal Aspects of Grinding: Part 1Energy Partition," *J. Eng. Ind*, vol. 96, pp. 1177–1183, Nov. 1974.

[8] S. Malkin and C. Guo, "Thermal Analysis of Grinding," *CIRP Annals - Manufacturing Technology*, vol. 56, no. 2, pp. 760–782, 2007.

[9] M. Shaw, *Principles of Abrasive Processing*. Oxford: Claredon Press, 1996.

[10] K. Nadolny, "A review on single-pass grinding processes," *J. Cent. South Univ.*, vol. 20, pp. 1502–1509, June 2013.

[11] I. D. Marinescu, W. B. Rowe, B. Dimitrov, and I. Inasaki, *Tribology of Abrasive Machining Processes*. Norwich, NY: William Andrew Publishing, 2004.

[12] R. L. Hecker, S. Y. Liang, X. J. Wu, P. Xia, and D. G. W. Jin, "Grinding force and power modeling based on chip thickness analysis," *Int J Adv Manuf Technol*, vol. 33, pp. 449–459, Apr. 2006.

[13] N. Chiu and S. Malkin, "Computer Simulation for Cylindrical Plunge Grinding," *CIRP Annals - Manufacturing Technology*, vol. 42, pp. 383–387, Jan. 1993.

[14] H. K. Tnshoff, J. Peters, I. Inasaki, and T. Paul, "Modelling and Simulation of Grinding Processes," *CIRP Annals - Manufacturing Technology*, vol. 41, pp. 677–688, Jan. 1992.

[15] G. Warnecke and U. Zitt, "Kinematic Simulation for Analyzing and Predicting High-Performance Grinding Processes," *CIRP Annals - Manufacturing Technology*, vol. 47, no. 1, pp. 265–270, 1998.

[16] T. J. Choi, N. Subrahmanya, H. Li, and Y. C. Shin, "Generalized practical models of cylindrical plunge grinding processes," *International Journal of Machine Tools and Manufacture*, vol. 48, pp. 61–72, Jan. 2008.

[17] S. Malkin and N. Joseph, "Minimum energy in abrasive processes," *Wear*, vol. 32, pp. 15–23, Mar. 1975.

[18] ASM International. Handbook Committee, *ASM handbook*. Materials Park, Ohio: ASM International, 10th ed., 1990.

[19] H. Saglam, F. Unsacar, and S. Yaldiz, "An experimental investigation as to the effect of cutting parameters on roundness error and surface roughness in cylindrical grinding," *International Journal of Production Research*, vol. 43, pp. 2309–2322, June 2005.

[20] S. B. Rao, J. F. Collins, and S. M. Wu, "A quantitative analysis of roundness error in cylindrical chuck grinding," *International Journal of Machine Tool Design and Research*, vol. 21, pp. 41–48, Jan. 1981.

[21] S. B. Rao and S. M. Wu, "Compensatory Control of Roundness Error in Cylindrical Chuck Grinding," *J. Eng. Ind*, vol. 104, pp. 23–28, Feb. 1982.

[22] W. Gao, S. Kiyono, and T. Sugawara, "High-accuracy roundness measurement by a new error separation method," *Precision Engineering*, vol. 21, pp. 123–133, Sept. 1997.

[23] Studer, "Conventional cylindrical grinding machine S30 - Studer https://www.studer.com /en/products /conventional/s30.html."

[24] Destaco, "Rotary Index Drives | DESTACO http://www.destaco.com /rotary-index-drives /1100rdm16h40-330," July 2017.

[25] Hardinge, "http://hardingeus.com/ProductCatalog/Product/150."

[26] Tsudakoma, "Tsudakoma RWA Series http://www.komaprecision.com/Tsudakoma RNA Series.html."

[27] Newbould, "The Newbould Grindit, http://www.imperialnewbould.com /the-newbould-grindit.html."

[28] Harig, "Spin-Indexer http://www.harigmfg.com/spinindexspec.html."

[29] J. Couey, E. Marsh, B. Knapp, and R. R. Vallance, "Monitoring force in precision cylindrical grinding," *Precision Engineering*, vol. 29, pp. 307–314, 2005.

[30] S. J. Drew, M. A. Mannan, K. L. Ong, and B. J. Stone, "The measurement of forces in grinding in the presence of vibration," *International Journal of Machine Tools and Manufacture*, vol. 41, pp. 509–520, Mar. 2001.

[31] J. C. Ramos, J. Vinolas, and F. J. Nieto, "A simplified methodology to determine the cutting stiffness and the contact stiffness in the plunge grinding process," *International Journal of Machine Tools and Manufacture*, vol. 41, pp. 33–49, Jan. 2001.

[32] H. K. Tnshoff, T. Friemuth, and J. C. Becker, "Process Monitoring in Grinding," *CIRP Annals - Manufacturing Technology*, vol. 51, no. 2, pp. 551–571, 2002.

[33] A.-M. O. Mohamed, R. Bauer, and A. Warkentin, "Uncut chip thickness and coolant delivery effects on the performance of circumferentially grooved grinding wheels," *Int J Adv Manuf Technol*, Nov. 2015.

[34] E. Marshall and M. Shaw, "Forces in dry surface grinding," *Trans. Asme*, vol. 74, no. 1, p. 51, 1952.

[35] J. Yoshioka, M. Miyashita, F. Hashimoto, and M. andDaitoh, "High Precision Centerless Grinding of Glass as a Preceding Operation to Polishing," *SME Technical Paper MR84*, vol. 542, 1984.

[36] T. W. Hwang, C. J. Evans, E. P. Whitenton, and S. Malkin, "High Speed Grinding of Silicon Nitride With Electroplated Diamond Wheels, Part 1: Wear and Wheel Life," *J. Manuf. Sci. Eng*, vol. 122, pp. 32–41, June 1999.

[37] E. R. Marsh, A. W. Moerlein, T. R. S. Deakyne, and M. J. Van Doren, "In-process measurement of form error and force in cylindrical-plunge grinding," *Precision Engineering*, vol. 32, pp. 348–352, Oct. 2008.

[38] A. B. Flatau, M. J. Dapino, and F. T. Calkins, "On Magnetostrictive Transducer Applications," *MRS Online Proceedings Library Archive*, vol. 604, Jan. 1999.

[39] H. E. Jenkins and T. R. Kurfess, "Adaptive pole-zero cancellation in grinding force control," *IEEE Transactions on Control Systems Technology*, vol. 7, pp. 363–370, May 1999.

[40] K. Nakayama, J. Takagi, and T. Abe, "Grinding Wheel with Helical Grooves - an Attempt to Improve the Grinding Performance.," *Manuf Technol, Gen Assem of CIRP, 27th*, vol. 26, no. 1 - 2, pp. 133–138, 1977.

[41] J. Verkerk, "Slotted wheels to avoid cracks in precision grinding," *Abrasive Engineering Society Conference*, 1979.

[42] C. Forbrigger, R. Bauer, and A. Warkentin, "A review of state-of-the-art vitrified bond grinding wheel grooving processes," *Int J Adv Manuf Technol*, vol. 90, pp. 2207–2216, May 2017.

[43] T. Suto, T. Waida, H. Noguchi, and H. Inoue, "High performance creep feed grinding of difficult-to-machine materials with new-type wheels," *Bulletin of the Japan Society of Precision Engineering*, vol. 24, no. 1, pp. 39–44, 1990.

[44] T. Waida, H. Noguchi, M. Rezaei, and T. Suto, "Creep feed grinding of ceramics and ceramic-matrix composites with slotted and perforated wheels," *J Jpn Soc Prec Eng*, vol. 57, pp. 324–329, 1991.

[45] Y. C. Fu, H. J. Xu, and J. H. Xu, "Optimization design of grinding wheel topography for high efficiency grinding," *Journal of Materials Processing Technology*, vol. 129, pp. 118–122, Oct. 2002.

[46] T. Nguyen and L. C. Zhang, "Performance of a new segmented grinding wheel system," *International Journal of Machine Tools and Manufacture*, vol. 49, pp. 291–296, Mar. 2009.

[47] J. F. G. Oliveira, A. C. Bottene, and T. V. Frana, "A novel dressing technique for texturing of ground surfaces," *CIRP Annals - Manufacturing Technology*, vol. 59, no. 1, pp. 361–364, 2010.

[48] A.-M. O. Mohamed, R. Bauer, and A. Warkentin, "Application of shallow circumferential grooved wheels to creep-feed grinding," *Journal of Materials Processing Technology*, vol. 213, pp. 700–706, May 2013.

[49] E. Uhlmann and L. Hochschild, "Tool optimization for high speed grinding," *Prod. Eng. Res. Devel.*, vol. 7, pp. 185–193, Apr. 2013.

[50] N. Ramesh Babu, V. Radhakrishnan, and Y. V. G. S. Murti, "Investigations on Laser Dressing of Grinding WheelsPart I: Preliminary Study," *J. Eng. Ind*, vol. 111, pp. 244–252, Aug. 1989.

[51] J.-S. Kwak and M.-K. Ha, "Force modeling and machining characteristics of the intermittent grinding wheels," *KSME International Journal*, vol. 15, pp. 351–356, Mar. 2001.

[52] D. Aslan and E. Budak, "Surface roughness and thermo-mechanical force modeling for grinding operations with regular and circumferentially grooved wheels," *Journal of Materials Processing Technology*, vol. 223, pp. 75–90, Sept. 2015.

[53] J.-D. Kim, Y.-H. Kang, D.-X. Jin, and Y.-S. Lee, "Development of discontinuous grinding wheel with multi-porous grooves," *International Journal of Machine Tools and Manufacture*, vol. 37, pp. 1611–1624, Nov. 1997.

[54] U. Koklu, "Grinding With Helically Grooved Wheels," *Proceedings of the Institution of Mechanical Engineers, Part E: Journal of Process Mechanical Engineering*, p. 0954408912470775, Dec. 2012.

[55] A.-M. O. Mohamed, A. Warkentin, and R. Bauer, "Prediction of Workpiece Surface Texture Using Circumferentially-Grooved Grinding Wheels," 2016.

[56] B. Denkena, J. Khler, and B. Wang, "Manufacturing of functional riblet structures by profile grinding," *CIRP Journal of Manufacturing Science and Technology*, vol. 3, pp. 14–26, Jan. 2010.

[57] N. P. Suh, M. Mosleh, and P. S. Howard, "Control of friction," *Wear*, vol. 175, pp. 151–158, June 1994.

[58] J. W. Byun, H. S. Shin, M. H. Kwon, B. H. Kim, and C. N. Chu, "Surface texturing by micro ECM for friction reduction," *Int. J. Precis. Eng. Manuf.*, vol. 11, pp. 747–753, Oct. 2010.

[59] J. Biera, J. Violas, and F. J. Nieto, "Time-domain dynamic modelling of the external plunge grinding process," *International Journal of Machine Tools and Manufacture*, vol. 37, pp. 1555–1572, Nov. 1997.

[60] M. Weck, N. Hennes, and A. Schulz, "Dynamic Behaviour of Cylindrical Traverse Grinding Processes," *CIRP Annals - Manufacturing Technology*, vol. 50, no. 1, pp. 213–216, 2001.

[61] Z. Sun, "BMNG 5210 Damped Frequency Identification for a Cylindrical Grinding Mechanics."

[62] S. A. Tobias and F. Koenigsberger, *Advances in Machine Tool Design and Research 1969: Proceedings of the 10th International M.T.D.R. Conference, University of Manchester Institute of Science and Technology, September 1969.* Elsevier, Dec. 2015. Google-Books-ID: 17ggBQAAQBAJ.

[63] C. Guo, Z. Shi, H. Attia, and D. McIntosh, "Power and Wheel Wear for Grinding Nickel Alloy with Plated CBN Wheels," *CIRP Annals - Manufacturing Technology*, vol. 56, pp. 343–346, Jan. 2007.

[64] M. C. Shaw, "The size effect in metal cutting," *Sadhana*, vol. 28, pp. 875–896, Oct. 2003.

[65] G. Tlusty, *Manufacturing Processes and Equipment.* Upper Saddle River, NJ: Prentice Hall, 2000.

Appendix A

Component lists

Table A.1: List of workpiece holder components

Workpiece Holder

Component	Manufacturer's ID	Description
Collet mount	Collet Master Index Fixture	Stiff workpiece mount
Face mount split collar	MacMaster Carr, 9677T7	Split collar used to mount large timing pulley to Collet Master
Large timing pulley	Automation Direct, APB72XL037B-375	72 tooth XL 3/8" timing pulley mounted to split collar
Small timing pulley	Automation Direct, APB11XL037BF-250	11 tooth XL 3/8" timing pulley mounted to motor
Timing belt	Automation Direct, 200XL037NG	100 tooth XL 3/8" timing belt connecting the timing pulleys
Brushed DC motor	Kelling, KL23-130-60	350 oz-in Nema 23 60 VDC motor to spin workpiece
Motor mount	Automation Technology, Nema 23 mount	DC motor mount
Encoder	US Digital, E5-500-250-NE-D-E-G-B	500 cpr differential encoder mounted to the motor
Mounting plate	N/A	1/2" stainless steel plate to mount components to force dyno
Force dyno	Kistler, 9257b	3 axis force dynamometer

Table A.2: List of main electrical box components

Main Electrical Box

Component	Manufacturer's ID	Description
Electrical box	Digikey, CS18188-ND	18"x18"x8" steel electrical box
Wall adaptor	Digikey, CCM1914-ND	120 VAC plug with switch to enter box
Cooling Fans	Digikey, 259-1509-ND	24 VDC, 90 mm fans for cooling
Motor power supply	AnTek, PS-10N63	1 kW, 63 VDC power supply for motor
Auxillary power	Digikey, 102-2526-ND	24 and 5 VDC power supply for auxillary components
Motor controller	Gecko, G320x	Digital servo drive
Encoder receiver	US Digital, EA-R-L-10-SH-10-W5	Receiver to convert the differential signal to singal ended

Table A.3: List of speed controller components

Pulse Generator

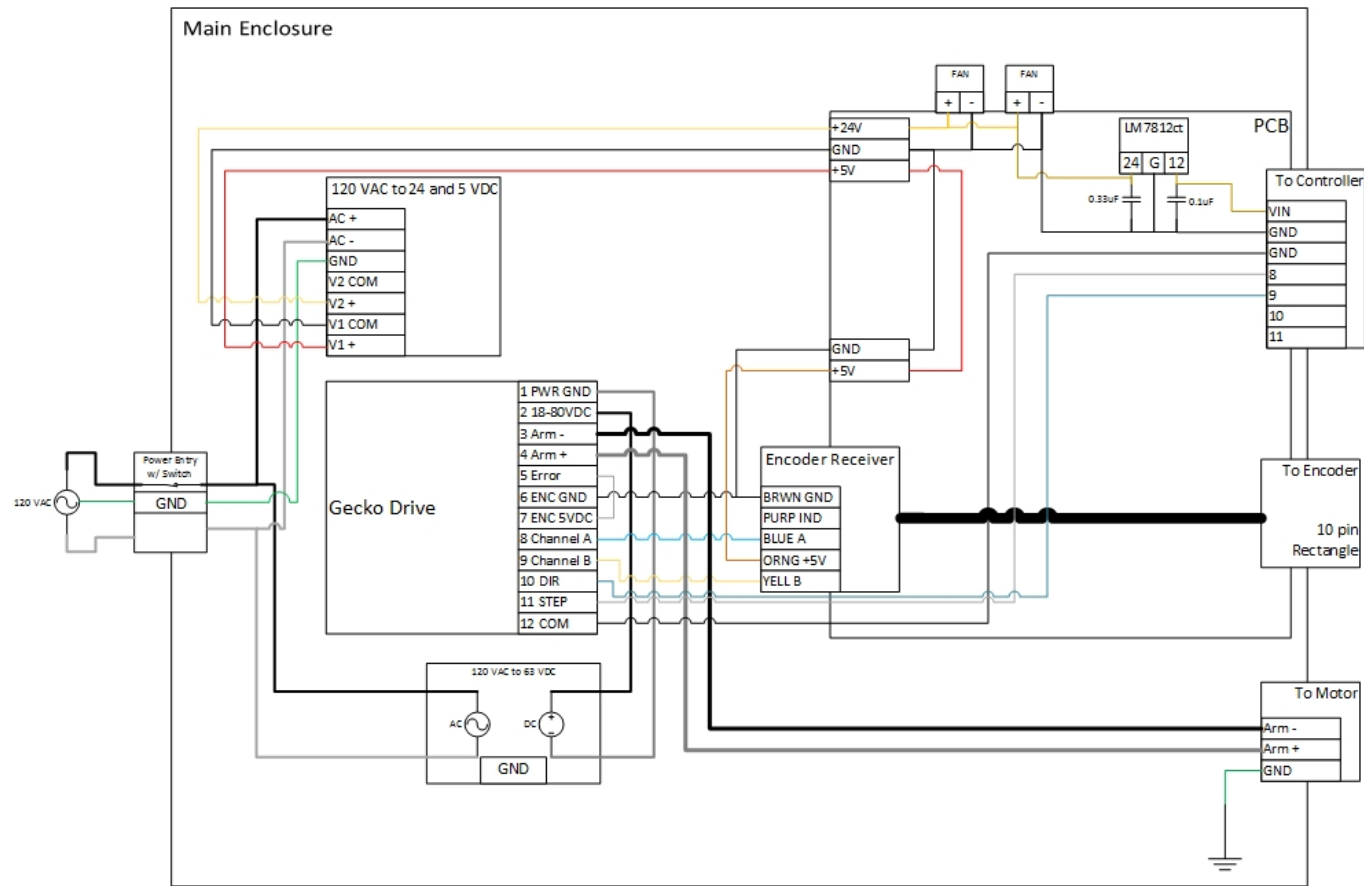| Component	Manufacturer's ID	Description
Microcontroller	Arduino, Uno R3	Sends pulses and direction based on user input
Housing	Home Depot, E989NNJ-CAR	4"x4"x2" PVC junction box to house speed controller
LCD Keypad	Adafruit, LCD Shield Kit	Acts as user interface
Faceplate	N/A	3D printed face to mount to keypad

Appendix B

Line Diagrams

Figure B.1: The line diagram for the main electrical box

Appendix C

Code

The following codes are g-code macros for plunge cylindrical grinding, O3350 and O3351, traverse cylindrical grinding, O3360 and O3361, and multiple pass traverse grinding, O3370 and O3371.

```
O3350 (PLUNGE CYLINDRICAL GRIDING);
G65 P9980 A0 M1 Q1 S100 T100 W55;
G65 P3351 S4000 H3 R1.00 Y0.0001 U1.00 T5.00 Z0.00;
G65 P9990;
M09;
G4 X10;
M05;
M30;
%

O3351 (MACRO FOR O3350);
IF [#19 NE #0] THEN #501 = #19;
S1 M#11;
G90;
G00 X0;
G00 Z#26;
G00 Y#18;
G01 Y-#25 F#21;
G04 X#20;
G00 Y#18;
M99;
```

```
%


O3360 (TRAVERSE CYLINDRICAL GRINDING);
G65 P9980 A0 M1 Q1 S100 T100 W55;
G65 P3361 S4000 H3 R1.00 Y0.0001 U1.00 T5.00 Z0.00 K3.00 W100;
G65 P9990;
M09;
G4 X10;
M05;
M30;
%


O3361 (MACRO FOR O3360);
IF [#19 NE #0] THEN #501 = #19;
S1 M#11;
G90;
G00 X0;
G00 Z#26;
G00 Y#18;
G01 Y-#25 F#21;
G04 X#20;
G01 Z#11 F#23;
G04 X#20;
G00 Y#18;
M99;
%


O3370 (MULTI PASS TRAVERSE CYL GRINDING);
G65 P9980 A0 M1 Q1 S100 T100 W55;
G65 P3371 S4000 H3 R1.00 Y0.0010 J0.0002 D5 U1.00 T5.00 Z0.00 K3.00 W100 M2;
G65 P9990;
```

```
M09;
G4 X10;
M05;
M30;
%


O3371 (MACRO FOR O3370);
IF [#19 NE #0] THEN #501 = #19;
S1 M#11;
G90;
G00 X0;
G00 Z#26;
G00 Y#18;
#28 =-#25+[#7*#5];
G01 Y#28 F#20;
#27 =#6-#26;
WHILE[#7 GT 0] DO1;
G91;
G01 Y-#5 F#21;
G04 X#20;
G01 Z#27 F#23;
G04 X#20;
#27 =-#27;
#7 =#7-1;
END1;
WHILE[#13 GT 0] DO1;
G91;
G01 Z#27 F#23;
G04 X#20;
#27 =-#27;
#13 =#13-1;
```

END1;

G90;

G01 Y#18 F20;

M99;

%